"STUDYING THE EFFECTS OF THERMO-OXIDATIVE AGING ON THE MECHANICAL, TRIBOLOGICAL AND CHEMICAL PROPERTIES OF STYRENE-BUTADIENE RUBBER"

Vihang Mhatre

Thesis submitted to the faculty of the Virginia Polytechnic Institute and State University in partial fulfillment of the requirements for the degree of

Master of Science
In
Mechanical Engineering

Saied Taheri. Chair
Corina Sandu
Maryam Shakiba

December 6, 2021
Blacksburg, VA

Keywords: Rubber aging, Viscoelasticity, Hyperelasticity, Rubber wear, User Material Subroutine, Continuum Damage Mechanics. Rubber Friction

STUDYING THE EFFECTS OF THERMO-OXIDATIVE AGING ON THE MECHANICAL, TRIBOLOGICAL AND CHEMICAL PROPERTIES OF STYRENE-BUTADIENE RUBBER

Vihang Mhatre

ABSTRACT

Styrene-Butadiene Rubber (SBR) is a form of a rubber compound that is widely used in the tire industry. This is due to some of their unique characteristics such as high strength, high elasticity and resilience, high abrasion resistance, ability to absorb and dissipate shocks and vibrations, low plastic deformation, high deformation at low levels of stresses, and high product life. One of the most important and often overlooked causes of SBR degradation and eventual tire failure is 'rubber aging.' It can be defined as an alteration in the mechanical, chemical, physical, or morphological properties of elastomers under the influence of various environmental factors during processing, storing and use. Some of these environmental factors are humidity, ozone, oxygen, temperature, radiation (UV rays), etc. This study focuses on the effects of two of these factors acting in tandem, oxygen and temperature. In the past, studies have been conducted to observe the effects of rubber aging on the mechanical and wear properties of rubber. Studies have also been conducted to study the reactions taking place in rubber during aging and changes in its chemical structure. These studies use different modelling techniques and experiments to quantify the effects of aging.

In this study, a material aging model that can predict the hyperplastic response of styrene-butadiene rubber (SBR) was mathematically developed using an integrated testing and continuum damage model framework. Coupling between the mechanical changes of SBR to the change in the chemical properties, specifically crosslink density (CLD) was also investigated. SBR dogbone shaped samples were accelerated aged in an aging oven at various temperatures and aging periods. Subsequently, hyperelastic tests were conducted to obtain the high strain response taking the 'Mullin's effect' into consideration. These responses were calibrated to different hyperelastic material models and the Arruda-Boyce model was chosen, due to its stable behavior and optimal fit. An aging evolution function was developed based on the variation in the model coefficients. This damage model is able to predict the hyperelastic response of SBR as it ages. A user material subroutine (UMAT) was also implemented in Abaqus based on the obtained aging evolution function to predict the stress response of SBR for varied applications. Additionally, to couple the chemical variations with the hyperelastic response, the rubber structure and composition was probed using Fourier-transform infrared spectroscopy (FTIR). The degradation of additives and SBR polymer chains were analyzed microscopically to explain the impact on the macroscopic properties. This study helps to correlate the change in crosslink density to ameliorate mechanical properties, such as strain at break, modulus, and stiffness.

The effects of aging on the viscoelastic properties of SBR were also studied. Dynamic Mechanical Analysis (DMA) was used to characterize the viscoelastic response. Master curves of storage and loss modulus were generated using the time-temperature superposition principle (TTSP). The friction coefficient was estimated from the storage and loss modulus using a simplified form of the Persson equation [1]. CLD was also estimated from DMA data. Wear experiments were conducted on the Dynamic Friction Tester (DFT) for various aging conditions. The estimated friction coefficient was compared to the one from the experiments. Archard's law was used to correlate the frictional energy to the volume loss during wear experiments. Correlation between the wear and the viscoelastic properties of SBR is also studied. Finally, the lifetime of SBR for various aging temperatures is predicted using various models.

STUDYING THE EFFECTS OF THERMO-OXIDATIVE AGING ON THE MECHANICAL, TRIBOLOGICAL AND CHEMICAL PROPERTIES OF STYRENE BUTADIENE RUBBER

Vihang Mhatre

GENERAL AUDIENCE ABSTRACT

Elastomers or rubbers are they are generally referred to are an indispensable part of human life. They are made up of long-chain polymer units linked to one other through crosslinks. This peculiar morphology of rubbers is what gives them their unique characteristics. There are as many as 40,000 known products that use some form of rubber as the primary raw material. Apart, from this, they are also widely used in aviation and aerospace, automobiles, dampers and absorbers, civil engineering, electronics, medical, toys, clothing, sports, footwear, and so on. This is due to some of their unique characteristics such as high strength, high elasticity and resilience, high abrasion resistance, ability to absorb and dissipate shocks and vibrations, low plastic deformation, high deformation at low levels of stresses, and high product life. Over the last couple of years, it has also played a pivotal role in personal protective equipment (PPE) and masks worn by billions of people and frontline workers all over the globe. The fact that rubber is included in the EU's list of critical raw materials [2] highlights its global importance.

However, over the past several years, the rubber supply has dwindled. COVID-19 also caused disruptions in the supply chain of rubber. As the effects of COVID-19 are fading, there has been a spike in the demand for rubber; the primary reason being automotive

tires! Even though substantial research is being conducted to try and replace rubber as a raw material with synthetic alternatives such as polyurethane, the excellent blend of damping, friction and wear characteristics, heat dissipation provided by natural rubber cannot be replicated by any of these laboratory compounds. Hence, at this time, there is an increased need to conserve and improve the longevity of rubber compounds.

Styrene-Butadiene Rubber (SBR) is a form of a rubber compound that is widely used in the tire industry. One of the most important and often overlooked causes of SBR degradation and eventual tire failure is 'rubber aging.' It can be defined as an alteration in the mechanical, chemical, physical, or morphological properties of elastomers under the influence of various environmental factors during processing, storing and use. Some of these environmental factors are humidity, ozone, oxygen, temperature, radiation (UV rays), etc. This study focuses on the effects of two of these factors acting in tandem, oxygen and temperature. In the past, studies have been conducted to observe the effects of rubber aging on the mechanical and wear properties of rubber. Studies have also been conducted to study the reactions taking place in rubber during aging and changes in its chemical structure. These studies use different modelling techniques and experiments to quantify the effects of aging.

The present study aims to model changes in the hyperelastic (large stretching) behavior of SBR using a Continuum Damage Mechanics (CDM) approach. This mathematical model is translated into ABAQUS, a finite element analysis software to study the mechanical response of components with various geometries and loading conditions. Secondly, the effects of aging on the viscoelastic behavior of SBR is studied. This helps us to estimate the cross-link density (CLD) as well as the friction coefficient of SBR as it is aged. The impact of aging on the wear and friction properties of SBR is studied experimentally. Finally, using various mechanical and chemical models the lifetime of SBR is estimated for various aging temperatures. Thus, the end goal of the study is to drive the development of new rubber compounds that will help improve the service life of rubbers and also have a positive impact on the environment.

ACKNOWLEDGMENT

Firstly, I would like to thank my family for giving me the opportunity to study at Virginia Tech and for constantly supporting me and believing in my abilities. I would like to express my heartfelt gratitude to Dr. Saied Taheri who gave me an excellent platform in the form of the Center for Tire Research (CenTiRe) lab to discover the vast and wonderful world of Tire research and sharing his expertise and knowledge and for providing constant guidance, throughout my graduate studies. I owe my knowledge and career in the tire industry to him.

I would also like to express my deepest appreciation to my committee members Dr. Maryam Shakiba and Dr. Corina Sandu for their valuable comments, suggestions, and contributions to my research. Many thanks to my lab colleagues, Waleed Alkandari, for helping me learn the core concepts of tire mechanics and for valuable contributions to my research as well as Zhen Xu, Rajvardhan Nalawade and Urvin Salvi for helping with experimentation and practical suggestions. It was indeed a fun and rewarding experience working with everyone at CenTiRe.

I very much appreciate Sumitomo Rubber Industries (SRI), especially Dr. Toshio Tada for constantly supporting the project in any way possible, by giving rubber samples as well as guidance for the study. I would like to thank CenTiRe and National Science Foundation (NSF) for providing the necessary funds for the project and the Industry Advisory Board (IAB) for the thought-provoking discussions and comments during technical meetings.

I cannot leave Virginia Tech without mentioning my roommates and all my friends for all the memorable time spent together at the lab, library and in social settings. Thank you for making me feel at home. Finally, I am deeply indebted to all my course professors who provided me with the invaluable knowledge to succeed in my research and life.

TABLE OF CONTENTS

LIST OF FIGURES

LIST OF TABLES

1 INTRODUCTION

AGING can be defined as an alteration in the mechanical, chemical, physical, or morphological properties of elastomers under the influence of various environmental factors during processing, storing and use. Some of these environmental factors are humidity, ozone, oxygen, temperature, radiation (UV rays), etc. Elastomers are made up of long-chain polymer units linked to one other through crosslinks.

Fig 1.1: Factors Causing Elastomer Aging

Today, different types of elastomers are widely used in aviation and aerospace, automobiles, dampers and absorbers, civil engineering, electronics, medical, toys, footwear, and so on. This is due to its many unique properties such as high strength, high elasticity and resilience, high abrasion resistance, ability to absorb and dissipate shocks and vibrations, low plastic deformation, high deformation at low levels of stresses, and high product life [3]. However, if the rubber is subjected to harsh environmental or working conditions, exposure to chemicals, it will lead to change in its properties which may, in turn, cause damage and eventually failure [4]. The severity of such failures will depend on applications, and in some cases, this can also prove to be fatal (passenger car tires.) Thus, modelling the effects of aging on rubber properties has many benefits. Some of them are:

- Improve service life of polymers in use
- Predict useful life of components in critical applications and prevent failures
- Help provide timelines for product or part replacements and maintenance
- Positive impact on the environment due to higher product life and fewer failures
- Serve as a factor that drives research and development of new durable rubber compounds

As seen, these environmental factors may work together to affect the rubber lifetime. However, it is very difficult to study the effects of all these factors combined and then individually separate their contributions. Hence, this study focuses on the degradation occurring due to the combined effects of two such factors that commonly cause rubber aging- oxygen and temperature. It is a well-known fact that in most scenarios, temperature speeds up the kinetics of reactions. Similarly, elevated temperatures, lead to faster oxidation and crosslinking reactions that typically take place in rubbers and alter their properties. The mechanical, as well as molecular changes, differ based on the material composition of the rubber as well as the additives and fillers used in it.

Styrene-Butadiene Rubber (SBR) is a synthetic rubber, which is produced on a very large scale due to its wide application portfolio in car tires, shoes, dampers, automotive parts, etc. In most of these applications of SBR, the polymer undergoes large mechanical loads, fatigue loads and environmental conditions. If they are subjected to very harsh conditions, they may degrade and fail, and its severity will depend on individual application Some of the properties that are affected by aging as seen in the literature are: tensile strength, strain at break, hardness, peel strength, wear performance, oxygen content, volume, color, stickiness etc. [5]. The SBR compound used in this study is a tire tread compound obtained from Sumitomo Rubber Industries (SRI), Japan. Being a tire tread compound, the material also consists of additives such as carbon black, antioxidants, oils, coupling agents, ZnO and other chemicals, wax, etc. All these additives are present in the compound to reduce wear as well as hinder oxidation and thus rubber aging.

Needless to say, a large amount of research has and is being conducted on various aspects of tires. They can be categorized into four types: 1) Rubber Lifetime, Wear and Friction 2) Noise, Vibration and Harshness and 3) Tire Dynamics 4) Tire Design and Analysis. Even after nearly 150 years since its invention, constant developments are being made in each of these departments in order to achieve longer tire life, reduce tire noise, fuel efficiency, sustainability, and so on. Safety is another very important factor. According to National Highway Transportation Safety Administration (NHTSA), there are about 11,000 tire-related motor vehicle crashes each year and nearly 200 people die in these crashes. Highly worn tires, reduced tread depth, aged tires, underinflated tires are some of the major reasons for these crashes. This

study aims to look deeper into some of the research that has been conducted over the years in the field of tire wear and friction.

1.1 RESEARCH OBJECTIVES

- Study the thermo-oxidative aging effects on the mechanical, tribological and chemical properties of SBR
- Model the mechanical changes using the Continuum Damage Mechanics (CDM) approach
- Develop an ABAQUS User Material Subroutine (UMAT) to predict the aged material hyperelastic response
- Study the effects of aging on the viscoelastic properties of SBR
- Study the effects of aging on the COF and wear of SBR
- Study the changes in chemical structure using FT-IR and determine the crosslink density
- Predict the lifetime of SBR at any given temperature

Chapter 2 focuses on the review of literature related to rubber friction and wear studies and also a review of its test setups. Furthermore, it also includes a summary of studies related to rubber aging and the various models and techniques used to characterize it.

Chapter 3 of this study deals with modelling the changes in the hyperelastic response due to aging. It also talks about developing a UMAT subroutine in ABAQUS.

Chapter 4 studies the changes in the viscoelastic properties of rubber as it is aged. It also strengthens the fact that mechanical and chemical changes observed in this research are indeed due to oxidative aging. This is done by calculating the CLD and plotting its change as the material ages.

Chapter 5 focuses on the tribology aspects of rubber aging. The friction coefficient is estimated using a simplified Persson model and experimentally determined from tests as well. Wear tests

are conducted, and mass and volume losses are measured. Frictional energy changes and viscoelastic changes are correlated to the volume loss during wear tests

Chapter 6 includes different types of novel mathematical models that can be used to predict SBR lifetime at various aging temperatures.

2 LITERATURE REVIEW

2.1 RUBBER FRICTION

We use the terms friction and wear quite often in our day to day lives. In simple terms, friction can be defined as the resistance to motion. It is responsible for the successful application of the contact by providing traction and grip. Wear can be defined as the degradation, erosion or destruction by friction or use. Thus, we easily find out that wear is a consequence of friction. Some of the earliest studies to evaluate and understand friction were done by Leonardo Da Vinci. He quantified friction by using a pulley block system shown in Fig. 2.1. Based on the experiments, he defined two laws of friction, friction is independent of the contact area, and it is directly proportional to the force acting perpendicular to its motion, i.e., normal force.

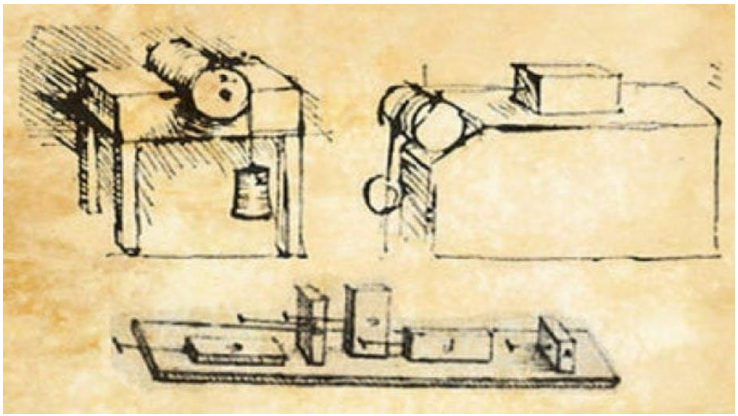

Fig. 2.1: Early Friction Setup

Later, Columb came up with the first empirical equation of friction given by Eq. (2.1)

$$F_f = F_N \mu \quad \textbf{(2.1)}$$

Where, F_f is the frictional force, F_N is the normal force and μ is the proportionality constant defined as the coefficient of friction. Further research showed that each surface consists of asperities. They can be classified as either micro or macro depending on their size. Due to these asperities, the actual area in contact is much smaller than the apparent area of contact.

Rubber friction is quite different from the friction properties observed in metals. The reason for this is that the modulus of rubber is very low compared to other solids that lead to high deformation. Another reason is due to the internal friction that occurs in the rubber structure over a wide range of frequencies [6]. Rubber is also a viscoelastic material. The word viscoelastic can be broken down into two words: viscous, which means it can flow to some extent and elastic, which means it can return back to its original shape. The structure of rubber can be simply imagined as a plate of noodles with all its strands entangled with each other. This entanglement keeps them together as a solid. Each strand represents a single polymer chain. The rubber used in tires is 'vulcanized', meaning crosslinks are formed between these strands by the addition of sulfur. This further strengthens the network and helps it to return to its shape (to some extent) even after it is deformed.

Another aspect of rubber in terms of friction that sets it apart from other materials is the rubber 'stickiness'. This in terms leads to the phenomenon of the 'stick-slip' motion (which also causes stick-slip vibrations) as a rubber block slides over the surface. It can be imagined as trying to slide your finger over tape, with periodic sticking and slipping when the slip forces overcome the stick force. Moreover, because of its low elastic modulus, during sliding, a compressive force area is developed in the front end which cause waves to propagate from the front end to the back end which are called 'Schallamach Waves' [6]. Additionally, rubber friction is dependent on surface texture and roughness. The coefficient of friction (COF) of rubber can be divided into two categories: static and dynamic. Static COF occurs at very low sliding speeds or when the body is just about to start sliding. It is the value that occurs just before the body is set into motion Dynamic COF on the other hand occurs while the body is in motion and is generally lower than the static COF. Thus, it can be concluded that the rubber friction phenomenon is very complex and fails to follow the general classical laws of friction.

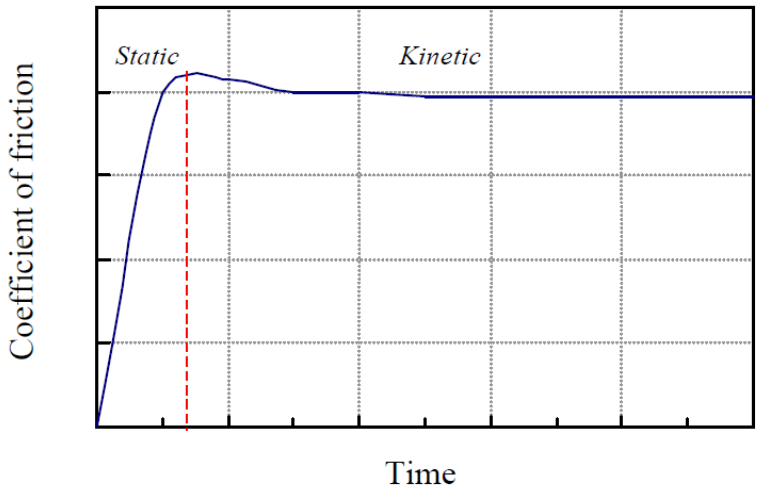

Fig. 2.2: Coefficient of Friction Components: Static and Dynamic

2.1.1 Mechanisms of Rubber Friction

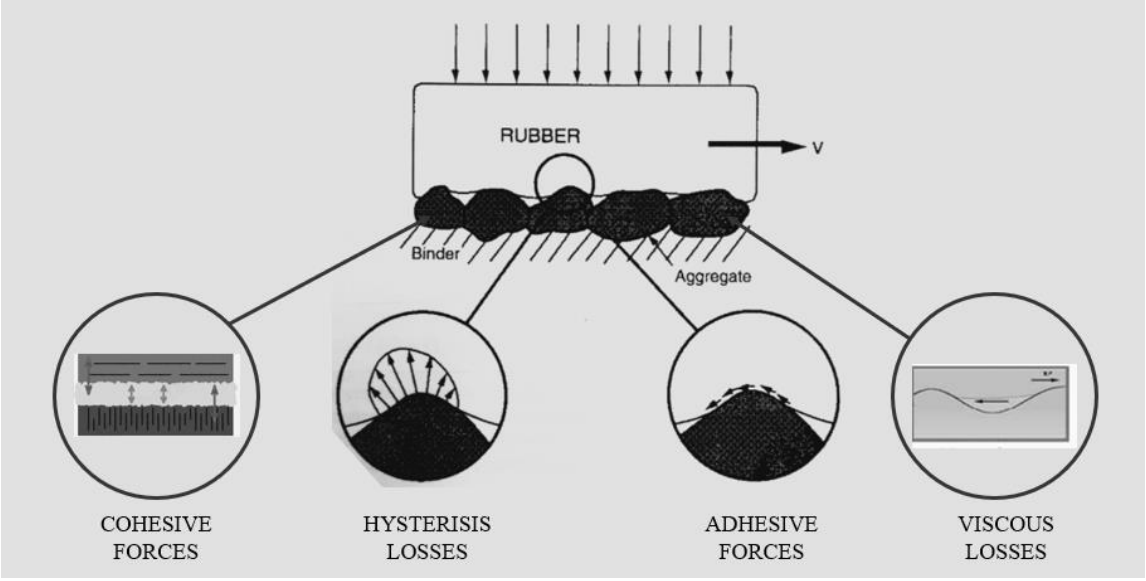

Fig 2.3: Mechanisms of Rubber Friction [7]

Based on the surface, operating and environmental conditions, the material composition of the rubber itself, frictional losses can occur at the rubber-surface interface by one or more of the following means as shown in Fig 2.3.

1. **Hysteresis (μ_h)**

   Hysteresis losses are observed in rubber and can be proved by simply observing the loading and unloading cycles as it is deformed. In real-world scenarios, the tread block in the tire comes in contact with the road and is deformed as it goes through the contact patch. The energy lost in hysteresis is converted to heat which increases the temperature of the surface. This type of frictional loss is very evident at rough surfaces and at high sliding velocities [8]. It is mainly related to the viscoelastic properties of rubber.

2. **Adhesive (μ_a)**

   As the name suggests, adhesive losses occur because of the inherent sticky nature of rubber. These types of losses are aggravated at smooth contact where there is an interaction of rubber microtexture with the micro asperities of the surface [8]. It generally occurs due to Van Der Walls forces and surface energies of bodies in contact. Needless to say, it is dominant at high loads and low sliding velocities. However, it can be neglected if lubricants and contaminants are present on the surface.

3. **Cohesive (μ_c)**

   Another important factor that plays a major role is the cohesive or abrasive loss. As the name suggests these losses are related more to the texture of the surface, the asperity distribution and the wear that occurs as a consequence. Numerous studies have been conducted that try to correlate abrasive friction to the microtexture and macrotexture of the abrading surfaces.

4. **Viscous (μ_v)**

   This is a special case of frictional loss which occurs in the presence of a fluid or lubricant. The fluid generates hydrodynamic resistance to the motion of the body in the interface. [9]

$$\mu_{total} = \mu_h + \mu_v + \mu_a + \mu_c \tag{2.2}$$

Thus, the total contribution to friction coefficient in rubber is due to the above-mentioned factors. There is no evidence of correlation or interdependence of one factor over the other.

2.2 RUBBER WEAR

Now that we have a better understanding of friction, we can investigate the phenomenon of rubber wear. Rubber abrasion or wear is a complex phenomenon that has mechanical, thermal, and chemical contributions [10]. Sometimes it can be a combination of different types such as mechanochemical wear or thermomechanical wear. Rubber wear is paramount in the tire industry as it determines the service life of a tire. When the tire tread is worn out to a certain level, the tires need to be changed. This leads to significant costs to the consumer but also has environmental implications. Hence, significant efforts are being made to come up with material compositions that will reduce treadwear. Like rubber friction, rubber wear is also a complex phenomenon, and the exact understating of the rubber wear process does not exist. To add to the complexity, tread compounds are made up of various fillers such as silica and carbon black as well as other additives. These fillers greatly alter the mechanical and chemical properties of the rubber compound. Each tire has its unique tread formulation based on its application and service conditions. All this make it exceedingly difficult to estimate or predict the wear rates of tires.

Yet another factor that largely affects the treadwear is the surface on which the tire is run or tested. In the past years, there have been debates over using lab surfaces or actual road surfaces to model tire wear. Both choices have their pros and cons. While on one hand, the lab tests are low cost, give quick results, and are highly repeatable due to known surface properties and controlled environmental factors such as temperature and humidity, they do not give an accurate representation of the wear that actually occurs in real life. This is because lab surfaces usually use an adhesive back sandpaper which is glued to a rotating disk or rolling drum which causes severe wear. Studies have been performed to correlate the laboratory test wear to road wear, but it needs a significant amount of time and experiments to come up with a robust model [11]. Thus, lab surfaces are usually preferred where a comparative study needs to be done between different tire or rubber types. Outdoor road surface wear tests are often plagued with uneven surface conditions, uncontrollable environmental factors, and a large amount of time for testing.

2.2.1 Mechanisms of Rubber Wear

Like friction, rubber wear also occurs in different forms and types as seen in Fig 2.4. Some of them are discussed below.

1. **Adhesive/Smearing Wear**

   This type of wear is less severe as compared to the other wear mechanisms. Under mild abrasion conditions, a very thin film is deposited on the surface. This is referred to as 'sticky-layer.' This is basically a sticky gooey transfer of rubber on the abrasive surface. This mainly occurs due to the high interface temperature that is generated due to friction [12]. One may also see this smeared layer as black tracks left on roadways when cars perform sudden braking. Another reason for smearing may be the thermo-oxidative degradation of polymer chains. An interesting fact about smearing is that it may actually reduce the subsequent wear that occurs after the deposition of the sticky layer [13]. This, however, is bad for laboratory testing which is mostly conducted on rolling or revolving tracks and the rubber comes into contact with the same surface multiple times. A lot of efforts are also put to reduce these errors in lab wear tests due to smearing. One possible mitigation is to continuously clean the abrader surface or feed in magnesium oxide powder or french chalk during wear tests. However, these powders act as lubricants which may again lead to erroneous results.

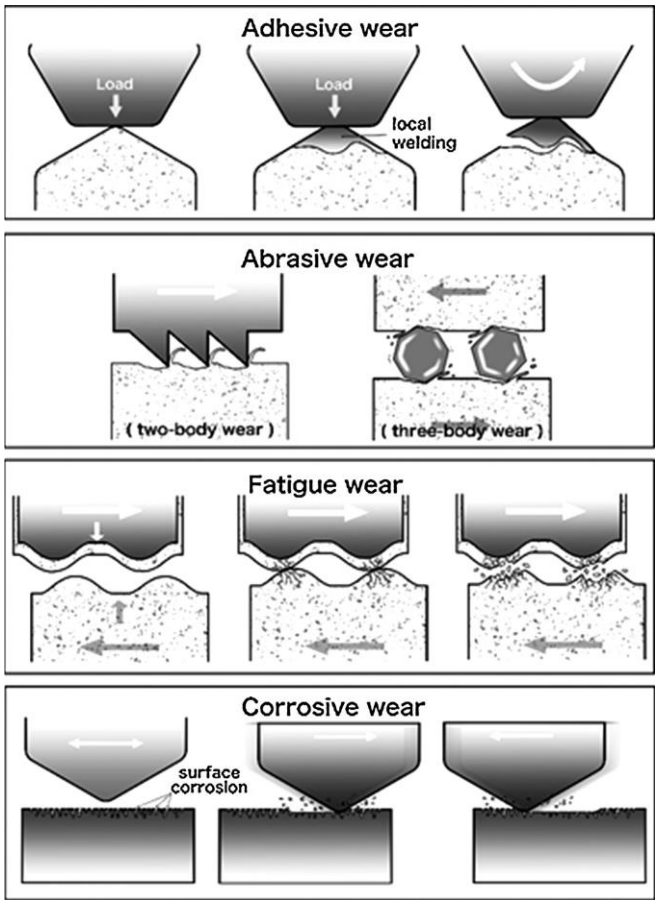

Fig 2.4: Mechanisms of Rubber wear [14]

2. Abrasive Wear

Abrasive wear is dominant when the surface consists of sharp asperities of a macro level. These asperities cut through the rubber that flows in them when its limiting strength is reached [15]. This type of wear is more severe than other types and leads to more mass loss. To study abrasive wear, studies have been conducted that quantify the wear that occurs at variable velocities and a range of temperatures. The time-temperature superposition principle (TTSP) can be used on this family of curves obtained. A reference curve is chosen and other curves at different temperatures (but same velocity range) are shifted to form a continuous 'master curve.' This is done using the William-Landel-Ferry (WLF) equation [16]. This is similar to the study conducted by Grosch that correlated friction to various sliding velocities by testing them at various temperatures and then shifting them using TTSP to get a 'friction master curve.'

3. **Fatigue wear**

This particular type of wear generally occurs when the asperities are not as sharp to generate severe abrasive wear. Thus, the mechanism of wear that takes place is called fatigue wear. Schallamach observed the formation of ridges perpendicular to the direction of motion of the abrader. These ridges formed a pattern across the surface of the rubber as seen in Fig 2.5 called as 'Schallamach Pattern.' A lot of studies have been conducted that try to correlate the rubber wear with these patterns, based on ridge spacing and ridge depth [17], [18]. However, these patterns tend to disappear when the direction or sliding velocity is changed. This is studied in detail by Nguyen et al [17] will be discussed in subsequent sections. Schallamach termed this abrasion as intrinsic abrasion. Fatigue wear increases due to reduction in glass transition temperature and reduction in filler concentration.

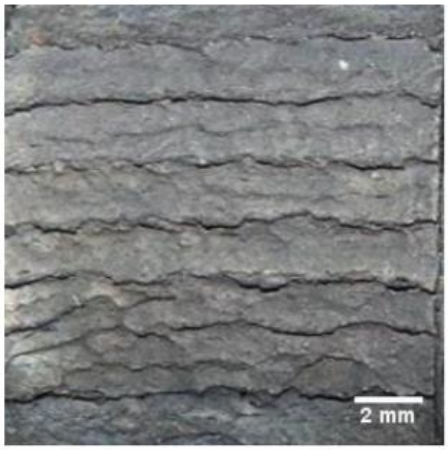

Fig 2.5: Schallamach Waves on Abraded Rubber Surface [15]

4. **Corrosive Wear**

As the name suggests, this wear occurs due to chemical degradation. It is related to oxidation and free radical formation at elevated temperatures at the interface. This process is highly dependent on the type of rubber compound under study as each one reacts to oxygen and temperature differently. A study by Schallamach shows that the rate of wear was low in air as compared to nitrogen [13]. A possible explanation behind this is the formation of the 'sticky layer' which hinder further wear. This sticky layer does not occur in a nitrogen rich (inert gas) environment. In some rubber compounds, the free

radicals form crosslinks rather than reacting with oxygen and hence corrosive wear is reduced.

2.3 FACTORS AFFECTING RUBBER FRICTION AND WEAR

1. **Normal Load/Contact Pressure**

   Generally, as the pressure increases, there is an increase in the apparent area of contact between rubber and the surface and hence, the wear volume increases with an increase in pressure or load. The amount of increase depends on the material as well as the test surface. It has been observed that COF decreases with an increase in pressure.

2. **Slip/Sliding Velocity**

   The COF increases gradually as speed is increased and then reaches a maximum value. It then levels off and falls slight at very high speeds. An alternate observation is made by Grosch when he used the TTSP and WLF equations to measure COF at various sliding speeds over a temperature range [19]. He observed that the shape of COF vs speed was a bell-shaped curve. Abrasion increases with an increase in slip velocity.

3. **Temperature**

   Temperature plays an exceedingly important role in rubber friction and wear. Temperature effects can be divided into three categories, ambient temperature, interfacial temperature, and flash temperature, of which the ambient and contact temperatures are easiest to control and analyze. The wear of the rubber decreases as the temperature is reduced below its glass transition temperature (T_g). However, when we go further below, the wear rate sharply increases, as it behaves like a solid well below T_g. Abrasive wear is dominant in this temperature region. It can be observed from the rods and curls of rubber formed. At very high temperatures, there is a slight increase in wear due to thermomechanical fatigue as well as ageing. Smearing wear is dominant and can be

observed by sticky layer formation as well as small particles of abraded rubber during the wear test.

4. **Surface**

The surface plays a very critical role in determining the rubber friction and wear. Other materials such as metals do not have a very strong friction dependence on surface characteristics. However, due to various properties of rubber that set it apart from other materials, friction, and wear change with surface texture. Micro and macrotexture of the surface affect various components of rubber friction which have been discussed in previous sections. Similarly, rubber wear and its mechanisms will be highly different on smooth surfaces like glass as compared to pavements.

5. **Humidity**

Studies related to the effect of humidity on rubber wear and friction are limited. However, humidity does not greatly affect wear and friction on rough surfaces. However, it can prove to be significant if the rubber is slid over a smooth surface or surface that have a majority of micro-texture. This is because humidity can affect adhesion and alter values of friction and wear.

6. **Oxygen Level**

Research studies show that abrasion studies conducted in inert atmospheres generate less wear as compared to that in air. One of the possible explanations is smearing wear. Black-filled compounds have been shown to smear more than their unfilled counterparts. Elevated temperatures are excellent conditions for oxidation which occur at extreme conditions (emergency braking, etc.) but may occur frequently in lab wear tests due to severe surface conditions. Thus, the absence of oxygen prevents the formation of free radicals and their combination with oxygen.

7. **Aging**

Aging of tires is another aspect that can largely affect the friction and wear characteristics of rubbers. Recently, NHTSA conducted thorough research on the effects of

underinflation and tire aging, especially at elevated temperature regions such as Phoenix [20]. This was done after a recall of around 14.4 million Firestone tires over safety concerns [21]. Studies are being conducted to understand the mechanical and chemical implications of tire aging. Accelerated oven tests are conducted to speed up the ageing process. Some research studies have proved that treadwear increases due to aging. Friction effects are currently unknown. Aging of the sidewall can lead to delamination and eventually tire failure and can be fatal.

8. **Material properties and composition**

   The compound formulation greatly affects wear and friction performance in treads. Additives and fillers such as carbon black help in reducing wear as seen in subsequent sections. Wax and antioxidants are added to reduce the attack of ozone as well as hinder oxidation which is the main contributor to tire aging. Continuous efforts are being made to develop newer compounds to attain better friction wear characteristics.

9. **Lubrication/Wet traction**

   Lubricants dramatically reduce wear as well as wear particle morphology. The nature of wear is abrasive in wet conditions or in presence of lubricants. The adhesive component of friction and wear can be considered practically negligible.

Comprehensive research has been conducted to study and model the changes in mechanical, chemical and tribological properties of elastomers due to most of the above-mentioned properties. However, the degradation of rubber and changes in the material and morphological properties has not been studied extensively by many researchers. This research gap was identified, and the causes and effects of rubber aging are studied in this thesis.

2.4 TEST SETUPS USED TO STUDY AND MODEL RUBBER FRICTION AND WEAR

Because there is no complete understanding of the rubber friction and wear phenomenon, or a model that can accurately predict them for any rubber compound, surfaces and test conditions,

laboratory experiments are still considered very useful to gather data quickly and accurately. Thus, a study of various friction and wear test rigs becomes imperative. Andrea Genovese et al [22] compiled these various test rigs in a review paper. The study is not exhaustive in the sense that it does not include all the test rigs used around the world, but it covers most of them and does an excellent job categorizing them. The study groups the testers into three main categories,

1) Rolling Friction Testers (RFT)
2) Linear Friction Testers (LFT)
3) Other miscellaneous friction testers

The RFT, as the name suggests uses a roller or a drum with abrading surface adhered to it. They can be both internal and external, depending on the applications. One of the downsides of these machines is the curvature of the drum which needs to be high to simulate flat road conditions. Also, it is very difficult to use asphalt due to curvature. The huge size is also a limitation, and the vibrations of drum and structural members may interfere with some of the sensitive experiments related to tire NVH.

The LFT is further classified as ‘sample in motion’, ‘surface in motion’ and ‘on-field’ testers. The first type of tester is currently used in the University of Hannover and University of Surry laboratories. Some of the advantages of using these testers are the high range of velocities, ability to run dry and wet friction tests and use different surfaces. The HiLiTe Test Rig and the test rigs at the Vienna University of Technology and Aalto University of Technology fall into the second category. They have similar advantages as those of the first type. The third type of tester is the on-field tester. One of them has been developed at the Center for Tire Research (CenTiRe) laboratory at Virginia Tech in collaboration with the University of Akron. A major advantage of this test rig is that it can be used on both indoor as well as outdoor surfaces. Another such tester has been developed by the University of Aachen with the difference that it is not a mobile device but rather attached to the floor. Environmental conditions cannot be controlled in these test rigs.

Next, we come to ‘other types of testers.’ The first among them is the pin-on-disk tester, which is one of the earliest used test setups. It is used in the ASTM G133 and G99 standards. The major disadvantage of the setup is that it cannot simulate real road conditions. The Dynamic Friction tester (DFT) is widely used for many studies due to its compactness and ability to simulate a

wide spectrum of test conditions as well as environmental conditions. It is used in the ASTM G115; ASTM E-1911 standards. A type of the DFT is also present at the CenTiRe lab at Virginia Tech which will be discussed in the latter sections. The last one is the British Pendulum Test (BPT). It is used in the ASTM E303 standard.

Many studies have focused on developing novel, durable and consistent test surfaces for lab treadwear studies. One such notable study was conducted by Bridgestone Americas and Bridgestone Tokyo [23]. The patent for the invention was filed in the year 2012. The invention relates to tire testing and fabrication of surfaces. In the past, patents have been filed for using silica sand with epoxy resins, casting polyurethane with the texture of asphalt or concrete, using road casted surfaces, and other molding methods with adhesives. The authors point the cons of using these surfaces and justify the superiority of their invention.

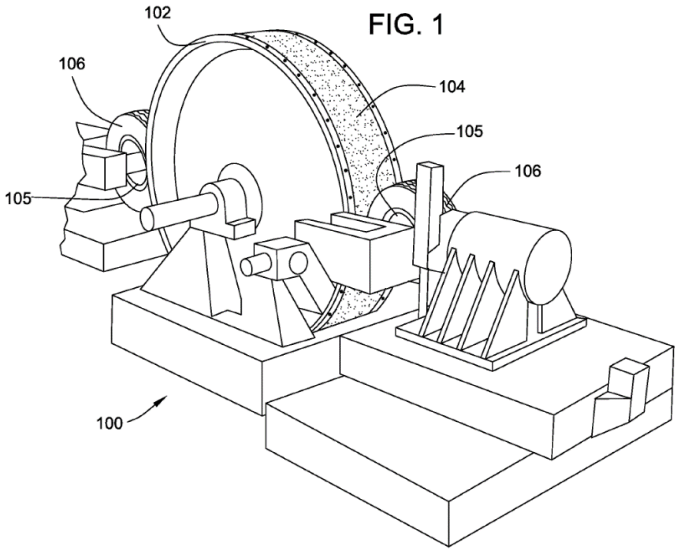

Fig 2.6: Bridgestone Americas Patented Test Setup [23]

As marked in Fig 2.6, 100 is the treadwear machine, 102 is the road wheel, 104 is the hardened wear surface, 106 is the tire being tested, 105 are rims. The hardened wear surface is disposed on a steel plate which is in turn fastened to the road wheel. The study emphasizes the macro

characteristics of the road (0.1-1mm) and large-macro characteristics (1-10 mm). The large-macro characteristics affect the road tire contact and hence need to be given more importance.

A negative cast of an actual road surface is used to stamp it on a layer of unhardened epoxy to get a positive cast. This is used to capture the large-macro roughness of the road at least. Next, the road surface is covered with liquid epoxy and hard aggregates are mixed to capture macro roughness. Embodiments of hard aggregates are added to increase durability. The road surface negative cast is used to imprint positive cast on the roadwheel. This surface creation results in accurate road roughness emulation increased service life of up to 500,000 miles compared to 50,000 sandpapers. Another way of creating the negative cast of the road surface is by scanning the road surface using a laser 3D scanner or a profilometer and then inputting that data into a 3D printer to generate an accurate representation of the road surface for capturing large-macro roughness.

2.5 RUBBER FRICTION AND WEAR MODELS

The above sections provided an understanding of the rubber friction and wear phenomenon and discussed some of the earlier studies that were conducted. In recent years, some studies have come up that look into rubber friction and wear with different perspectives. Some of them challenge the older studies while some tend to add and complement the earlier results with large data collected over the years and the use of image processing and machine learning models to predict tire performance and characteristics [24]. Some of these recent studies have been compiled in this section to gain insights on various perspectives regarding rubber wear and friction and to guide further research in the area.

Y. Fukahori et al challenged the classical friction and wear studies and proposed a new model which is significantly different from them. The study proposes that the adhesive friction component, which has been assumed to be very small in previous literature, to be quite significant. The study proposed the total friction coefficient to be comprised of adhesive factor and the factor occurring due to stick-slip motion. This paper focuses on the interfacial properties of rubber rather than viscoelastic properties. The second focus of the paper is on wear in relation

to the formation of abrasion patterns. The abrasion pattern is due to the high-frequency vibration and is promoted by the stick-slip motion.

Schallamach, Grosch and Moore developed models that focused on the viscoelastic effects on rubber friction and wear. Schallamach reported temperature and velocity dependence on rubber friction. Grosch used WLF transform [16] to estimate friction at low sliding velocities (10^{-5} to 1 cm/s) as a function of temperature [19]. It gave rise to the well-known conclusion "peak of friction occurs at peak of tan delta" [19]. Moore developed a friction model based on adhesion and deformation backed by Grosch's data which split the friction term into adhesion and deformation factors [10]. They were a function of velocity, pressure, modulus, tangent delta, and the peak of COF occurs as glass transition temperature as seen in Fig. 2.7.

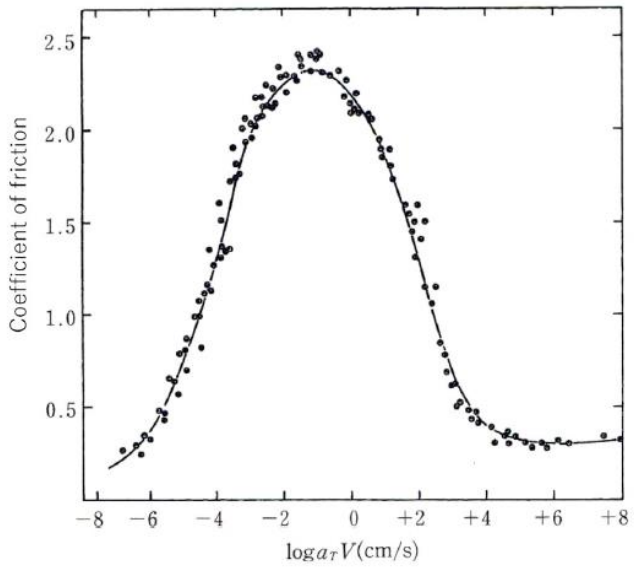

Fig 2.7: Friction Coefficient as a Function of Velocity (after shifting curves, (Grosch) [19]

Barquins and Roberts replicated Grosch's experiments and found out that there is a gradual increase in COF with the speed up to 10^2 mm/s, but it levels off at around 10^4 mm/s speed range as shown in Fig 2.8 [25]. Thus, they concluded that the change in COF w.r.t velocity does not fully form a bell shape. They also observed violent stick-slip at higher velocities thus making the system unstable.

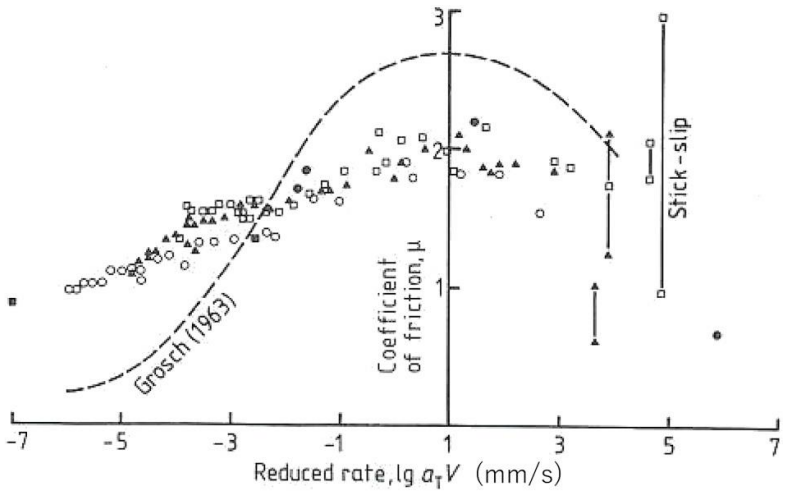

Fig 2.8: Friction Coefficient as a Function of Velocity (after shifting curves, Barquins and Roberts) [25]

Fukahori also proposed a new model for vulcanized rubber. Earlier, it was thought about as homogenous, consisting of crosslinked rubber molecules. His new theory assumes it to be a combination of a seamless uncrosslinked phase (30% volume) and a seamless crosslinked phase (70% volume) with a meniscus at the interface [26]. Other studies by Nakajima [27] and Fukahori, Gabriel and Busfield [28] supported this observation of meniscus formation and thus explained the stick-slip behavior as well.

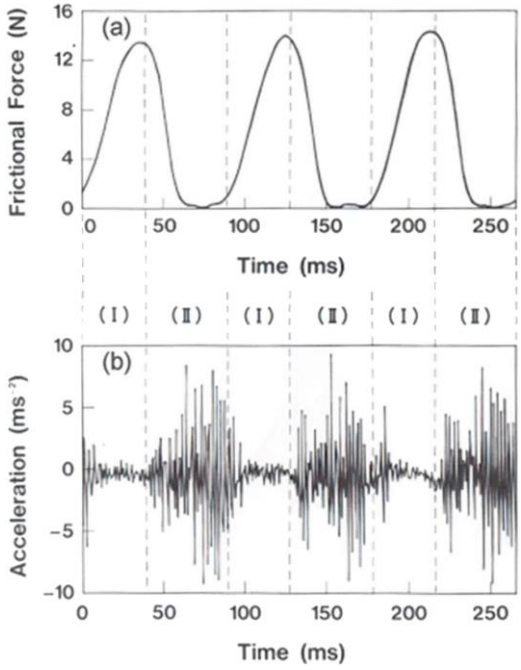

Fig 2.9: Frictional Force and Acceleration Data [18]

Experimentation using a steel slider was carried out to gain a deeper understanding of the stick-slip phenomenon and the high-frequency vibrations generated as rubber slides over a surface and how it relates to COF as well as abrasion patterns.

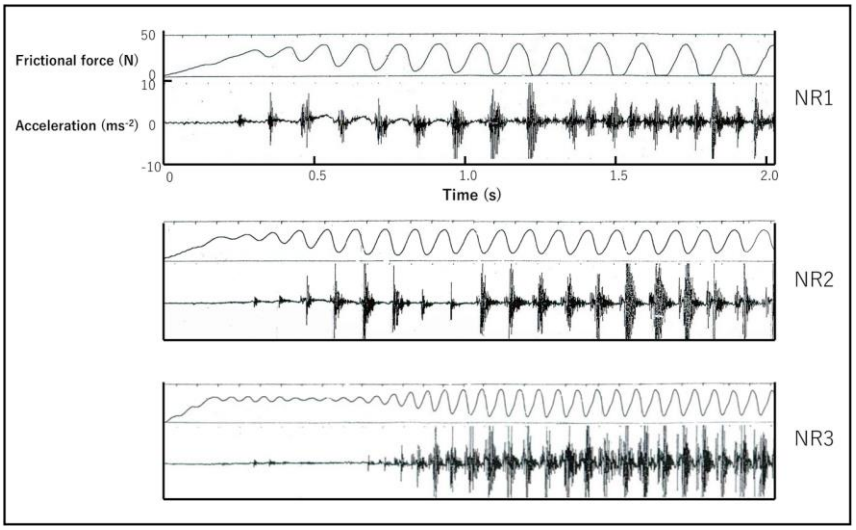

Fig 2.10: Frictional Force and Acceleration Data for various Rubber Samples [18]

Fig 2.11 shows the interaction of the surface with rubber characterized as a combination of heterogenous crosslinked and uncrosslinked phases with a meniscus being formed at the interface. The high viscous characteristics of the uncrosslinked phase generate a very high adhesive force, which is greater than the Van der Waals force which was validated by other studies as well. The study also concludes that the presence of water greatly hinders the meniscus formation and hence can explain the reduce COF in wet conditions.

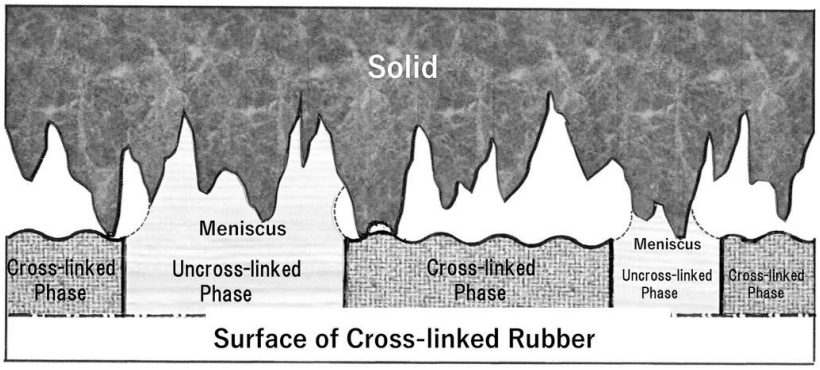

Fig 2.11: Surface and Rubber Interaction [18]

As per the study, the total friction force is caused due to the contribution of the adhesion factor and the stick-slip motion.

$$F_{all} = F_{ss} + F_{adh} \tag{2.3}$$

Additionally, the stick-slip term can be further divided into hysteresis losses and force due needed for crack formation components.

$$F_{ss} = F_{def} + F_{crack} \tag{2.4}$$

Furthermore, the adhesive component is divided into the Van der Waals force and the meniscus force.

$$F_{adh} = F_{vanderwalls} + F_{meniscus} \tag{2.5}$$

Next, the study focuses on correlating the abrasion to the abrasion pattern (pattern spacing and depth). The distance between the cracks increases till it reaches a steady-state which follows a trend similar to that of the rate of wear. Thus, it can be concluded that the wear rate also is a consequence of the stick-slip motion. Schallamach [29] had proposed an empirical relation for wear rate (*V)* with respect to abrasion pattern spacing D_{ab}, given by Eq. (2.6).

$$V = a\, D_{ab}^{n} \tag{2.6}$$

Where n varies with material and surface but in general can be assumed to be 3.

The above study helps us understand the friction and wear phenomenon through a different perspective and validates the wear rate model proposed by Schallamach. However, this wear model is dependent on the formation and observation of so-called abrasion patterns which appear only at certain test conditions and when there is no arbitrary change in sliding speed both in terms of magnitude and direction. Thus, the model may fail when such conditions arise which is similar to what happens in real-world scenarios as well. Schallamch defined such abrasion as ‘intrinsic abrasion.’ Nguyen et. al [17] developed an advanced model for tire wear that considers the history dependency and directional effects of abrasion and in turn predict tire wear.

Experiments were conducted on the Grosch wheel setup with the wheel and track temperature being 45℃/45 ℃ respectively and the 30℃/10 ℃. The slip angles were also varied. It was

observed that more wear is observed in the change of slip angle from 4 degrees to -4 degrees compared to change from 5 degrees to 3 degrees which are in turn greater than the abrasion at a constant 4-degree slip angle. The study proposes that the rate of wear ($\dot{w}$) is a function of the contact pressure (P), the flash temperature (Θ), sliding speed (v_s), damage vector (D) and rate of frictional dissipation (D_s). Similarly rate of Damage ($\dot{D}$) is dependent on the same mentioned factors.

Damage is generated in a body depending on these above factors and damage is released due to the material loss occurring over time. Thus, the study proposes the directional damage rate given by Eq. (2.7)

$$\dot{D} = (1 - || D ||)\, \alpha \left(\frac{P}{P_o}\right)^{\beta} \left(\frac{|| v_s ||}{v_o}\right)^{\gamma} \frac{v_s}{||v_s||} - \tau\, \dot{w}\, D \tag{2.7}$$

As seen earlier as well, the simple abrasion model is given by Eq. (2.8)

$$\dot{w} = \lambda\, \dot{D}_s \tag{2.8}$$

Where, λ is the abrasion factor. This factor is adjusted to incorporate the directional effects on the model. A dependency of the abrasion factor on the direction of slip velocity is illustrated in Fig 2.12. It shows the abrasion factor for various magnitudes of damage. Some of the points of interest are also marked. θ is the angle between the slip velocity and the damage direction which is 0 for the case of unidirectional sliding and is 180 when the direction is completely reversed.

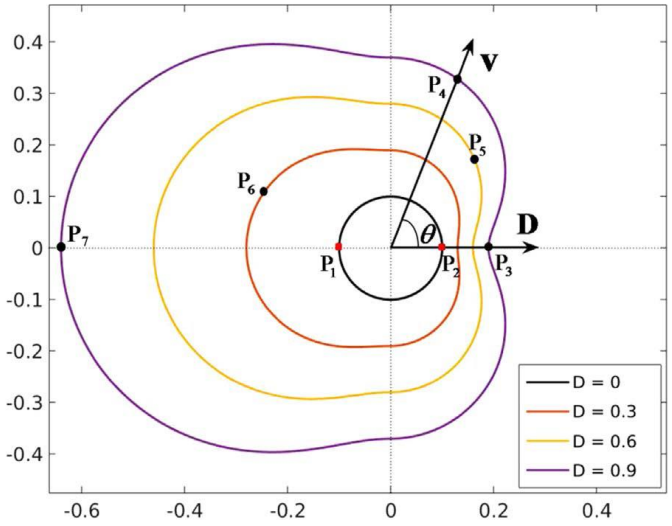

Fig 2.12: Damage Factor as a Function of Direction and Slip Velocity [17]

Eq. (2.9) is introduced to find which factors affect the abrasion factor.

$$\lambda = \frac{h}{E_T}\,(1 + ||\, D \,||\, \phi) \tag{2.9}$$

Where, h denotes the wear particle dimension, E_T is the tearing energy needed to generate a unit surface, ϕ is a function of θ and is chosen as a parametric curve defined by Eq. (2.10).

$$\phi = \sqrt{(a_1\, cos\ \theta)^2 + (b\, sin\ \theta)^2}, \qquad if\ \frac{\pi}{2} \le \theta \le \frac{3\pi}{2} \tag{2.10}$$

$$\phi = \sqrt{(a_2\, cos\ \theta)^2 + (b\, sin\ \theta)^2}, \qquad otherwise$$

The model is also analyzed for sliding speeds at different directions and particular angles. This is validated by experiments and the model does predict the wear quite accurately. The Grosch wheel experiments were also simulated using an uncoupled thermomechanical model using Arbitrary Lagrangian-Eulerian (ALE) FEM to predict the abrasion.

The next study [30] focuses on the wear rate under coupled rolling and sliding conditions. The authors state that even though there exist multiple models for wear under sliding conditions, the combined rolling and sliding conditions remain unexplored.

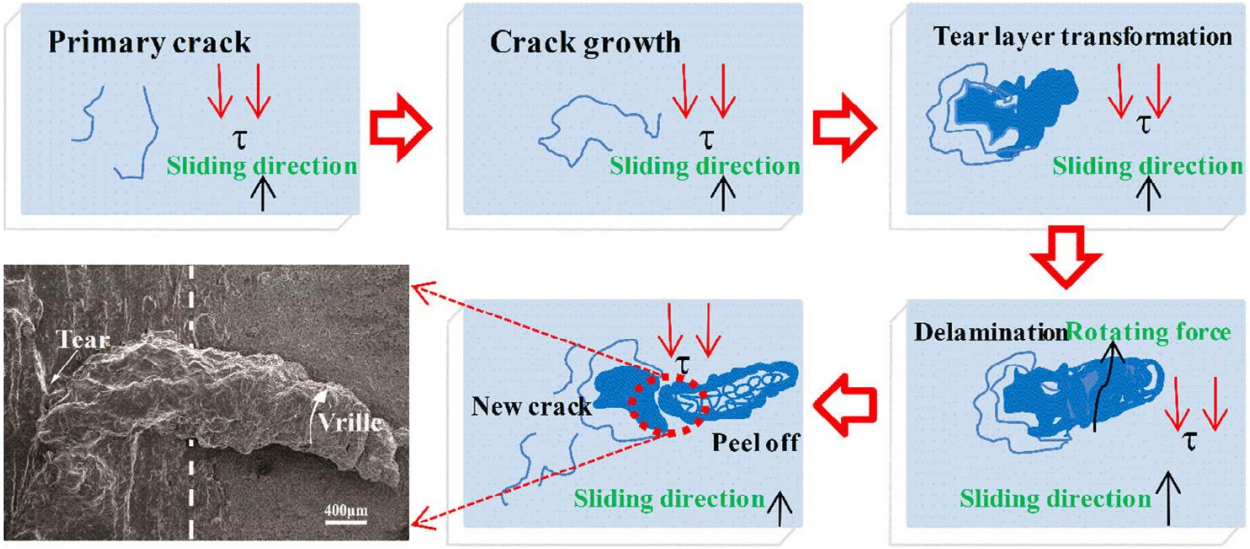

Fig 2.13: Debris or Wear Particle Formation and Cut-off [30]

A thermal numerical analysis was performed in the contact region to understand the role of temperature in the wear mechanism. The authors defined the longitudinal slide-roll ratio (LSSR) as the ratio of relative linear velocity to mean linear velocity. Tests were conducted on an

improved Akron tester machine. As expected, the wear observed for low LSSR values was low with small debris particles (adhesive, fatigue, and abrasive wear) which changed to large rod-like particles at high LSSR values (thermofatigue, tear wear, adhesive tear, curl wear, thermal decomposition). Debris formation at high LSSR values is shown schematically in Fig 2.13.

The major contribution of this study is that it establishes a relationship between friction heat and wear mechanisms. The authors divide the total heat generated into two components, hysteresis heat and friction heat. They are given Eq. (2.11).

$$Q_{hysteris} = \pi\, n\, \epsilon_0^2 E^{"} \qquad Q_{friction} = \frac{\mu\, N\, v_s}{2b\sqrt{2R\epsilon_o - \epsilon_o^2}} \tag{2.11}$$

Where, n is the speed of the rubber wheel, ϵ_o is maximum variable, $E^{"}$ is loss modulus, μ is COF, N is positive pressure, v_s is sliding speed. Thus, the total heat generated per unit area is

$$Q_{total} = Q_{hysteris}$$

Fig 2.14 shows the heat distribution across the rubber surface for various LSSR values. Using Fourier heat conduction law and Newton's Law of Cooling, using appropriate boundary conditions, and assuming that the experimental time is long enough (wave equation is neglected), the function of temperature rise of rubber across the surface was established.

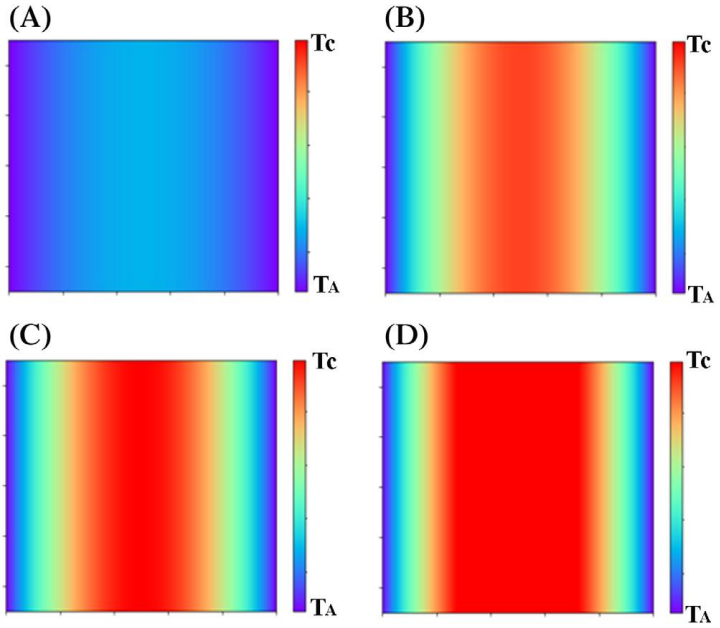

Fig 2.14: Heat distribution for LSSR values (from (A) to (D) increasing LSSR values) [30]

Rubber wears due to crack formation, propagation and peel and tear. When the interface temperature reaches a critical value, the rubber breaks down (thermomechanical fatigue/degradation) and this, in turn, increases peel and tear, increasing overall wear. These results can be used to make high-performance tread compounds that can combat the issue of heat dissipation at higher LSSR values more efficiently thus reducing wear.

So far in this section, papers related to the friction and wear theories that are a function of contact pressure, velocity, temperature, environmental effects, etc. are reviewed. However, the abrading surface is a very important factor that changes the wear and friction properties of rubber to a great extent. This factor is not considered in the papers discussed above. Hence, a change in the surface type (glass, concrete, pavement) or roughness can greatly affect the results. The following study tries to bridge this gap. We have seen many types of abraders reviewed by Genovese et al [22] and each one uses unique surfaces. The contact type may be point (needle), line (razor blade slider) or area (sandpaper/asphalt surface). Blunt surfaces cause mild wear, mostly adhesive and fatigue and sharp asperities cause severe abrasive and tear wear.

R. Ramakrishnan et. al [31] conducted wear tests on a modified Lambourn abrader shown in Fig 2.15 with grindstone used as an abrading surface. A desired amount of slip was set for the runs. Grit size was approximated by grit number.

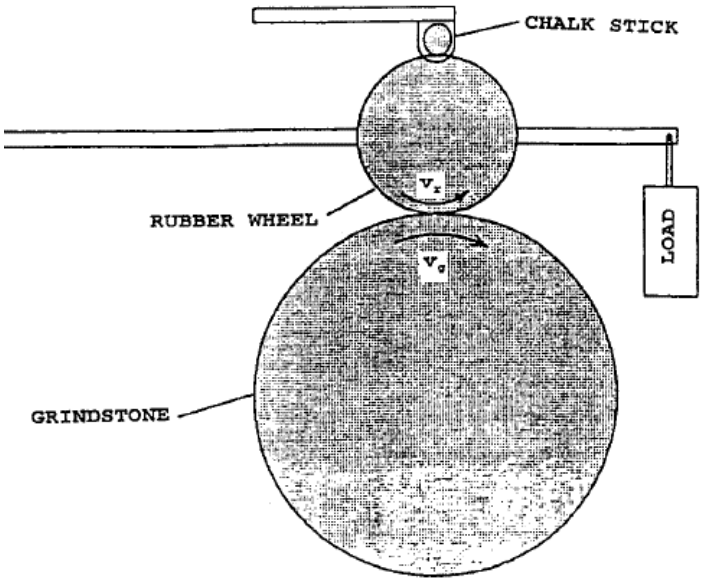

Fig 2.15: Test Setup Lambourn Abrader [31]

Contact pressure was also changed which ranged from 14 N to 48 N. Chalk stick was used in the wear process to reduce the effect of smearing. Wear rate was calculated from the weight loss and number of revolutions of the sample. Another set of experiments were conducted for fatigue crack growth and the fatigue exponent β was found out. Hertzian cylindrical contact model is used to calculate the length of contact. COF was found to be directly proportional to the pressure/load and inversely proportional to the modulus as seen in previous studies as well. The new model developed in this study considers the wear to be a product of the wear volume per grit, grits passed by rubber per revolution, and the density of rubber, given by Eq. (2.12).

$$W = w \times \delta\left[a_0 (f/w)^{\beta}\right] \times N_0 tc \times \rho \tag{2.12}$$

Where, w is contact width, δ is penetration depth, f is fraction force, N_0 is the number of grits per unit area, t, c are the thickness and circumference of rubber wheel respectively and finally ρ is the rubber density as seen in Fig 2.16. Furthermore, it was found that the wear rate is proportional to the diameter of the grit size and fatigue factor given by Eq. (2.13).

$$W^* \propto \dot{d}^{-(2+\beta/3)} \tag{2.13}$$

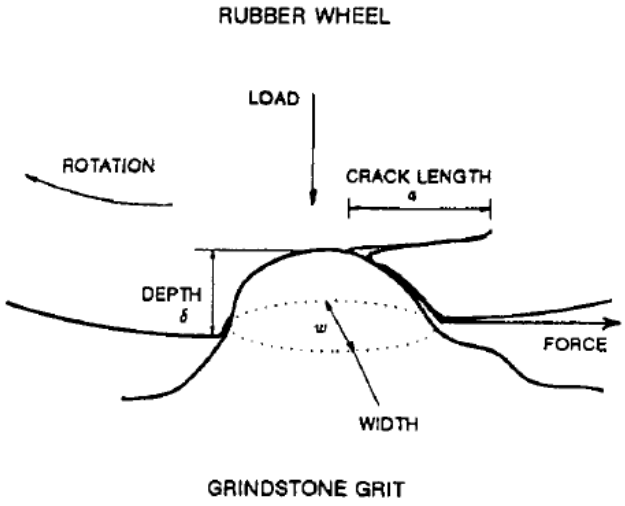

Fig 2.16: Rubber Surface Interaction and Crack Properties and Dimensions [31]

The wear rate was plotted as a function of grit diameter and the exponents found were in the range of -5.3 and -4.4, but the ones predicted from the model is around 1.8 which is three times

lesser than the data. This can be explained by the assumption that the grits are completely spherical and evenly distributed. Also, the real contact area is considered instead of the apparent contact area and pressure dependence is not considered in the model.

As seen in the above study, the rubber wear is correlated to the grit diameter of the grindstone surface. But the major issue in doing so is that the diameter is considered even across the entire surface. This is not true especially in real road conditions where the surface is made of uneven distribution of microtexture (wavelength and amplitude < 0.5 mm) and macrotexture (wavelength and amplitude > 0.5 mm). Gunaratne et. al [32] aimed to develop a correlation between tire wear and friction and the pavement texture properties. Many test setups like BPT, profilometer, sand patch and grease patch method, can be used to measure the pavement texture. Past studies have tried to correlate tread wear with the COF and macrotexture depth parameter (T).

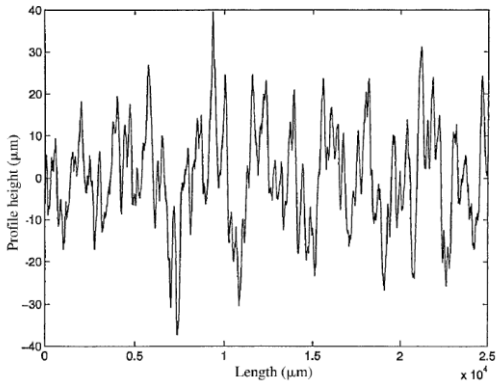

(A)

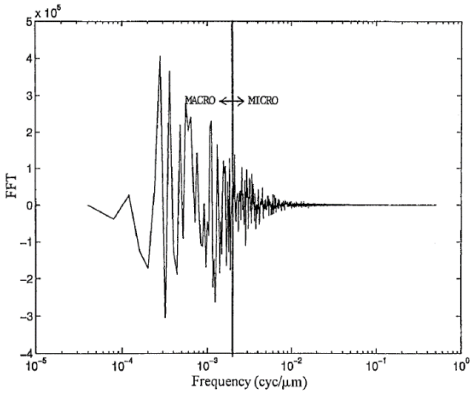

(B)

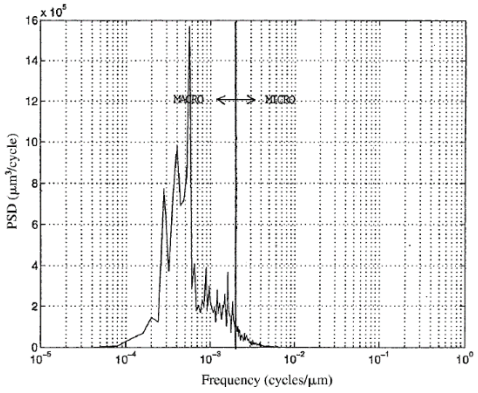

(C)

Fig 2.17: (A) Surface Profile (B) Separating Micro and Macro Texture (C) Separation of Power Spectral Densities (PSD) as Micro and Macro [32]

Tests were conducted on the friction/wear testing machine and the dry and wet friction force was measured. Spectral analysis techniques like Fast Fourier Transform (FFT) were used to analyze surfaces and the Power Spectral Density (PSD) was found out. Furthermore, the area under the PSD curve was calculated and was used to quantify the frequency and roughness characteristics in terms of spatial frequencies. Finally, these plots were used to distinguish between pavement micro and macrotexture as seen in Fig 2.17.

As discussed in previous studies, COF can be divided into hysteresis and adhesion component. The adhesion component is naturally dependent on the microtexture while the hysteresis is dependent on the macrotexture [33]. Regression models were developed correlating COF to the area under the PSD curve corresponding to microtexture (Micro) and the macrotexture (Macro). It was given by Eq. (2.14).

$$\mu_{dry} = 2.618 + 0.481\, Log\ (micro) - 0.701\, Log(Macro)$$

$$\mu_{wet} = 1.015 + 0.251\, Log\ (micro)\ - 0.302\, Log\ (macro) \quad \textbf{(2.14)}$$

An interesting observation is that the coefficient for microtexture PSD is more for dry compared to wet as adhesion is negligible in wet conditions. Similar to the COF, the wear rate relationship with these factors were also investigated and the following regression Eq. (2.15) was developed.

$$Log(K_w) = -0.959 + 0.365\, Log(micro) - 0.486\, Log(macro) \quad \textbf{(2.15)}$$

As seen from the equation, the more the microtexture area, the higher is the wear and the more the macrotexture area, the less is the wear. This can be explained due to less contact between rubber and the surface. The proposed model was validated using laboratory tests using similar particle size, thus resulting in similar roughness to the earlier surface. On-field tests were also conducted on a concrete aircraft runway and the COF and wear rates were predicted accordingly. Thus, this study emphasizes the importance of studying pavement texture profiles for estimating

friction and wear and will also be useful in designing pavements with the right amount of skid resistance and acceptable tire wear rates.

Many studies conducted in the area of rubber friction and wear make use of many complex test setups as seen earlier. As the complexity of the setups increases, so does the cost. The following study conducted by T. Vieira et. al [34] aims to evaluate friction and wear rates using low-cost tests. The study uses the BPT as well as Rotary Drum Abrader to evaluate wear and friction. Abrasion patterns were analyzed under a microscope to measure the mean wavelength of abrasion patterns for each test specimen.

The friction values and the energy lost in the BPT can be given from Eq. (2.16)

$$D\ F_N\ \mu = W\ (H - h) \tag{2.16}$$

Where, D is the contact length of the British pendulum, F_N is the normal force, μ is the COF, W is pendulum weight, $H - h$ is the height difference between initial and final position. COF for all rubber samples is calculated on both pavement and sandpaper surfaces.

$$W_{wear} = \frac{\mu N d}{\Delta m} \tag{2.17}$$

Work of wear (W_{wear}) is an index used to calculate the efficiency of rubber materials given by Eq. (2.17). Care should be taken while using work of wear as it is only applicable to compare tires of similar performance characteristics and having the same master curve peaks.

Linear regression was performed over wear and wavelength observed and it showed a good correlation, thus proving that large wavelength is an indication of severe wear. Surface energy vs friction plot also showed linear correlation,

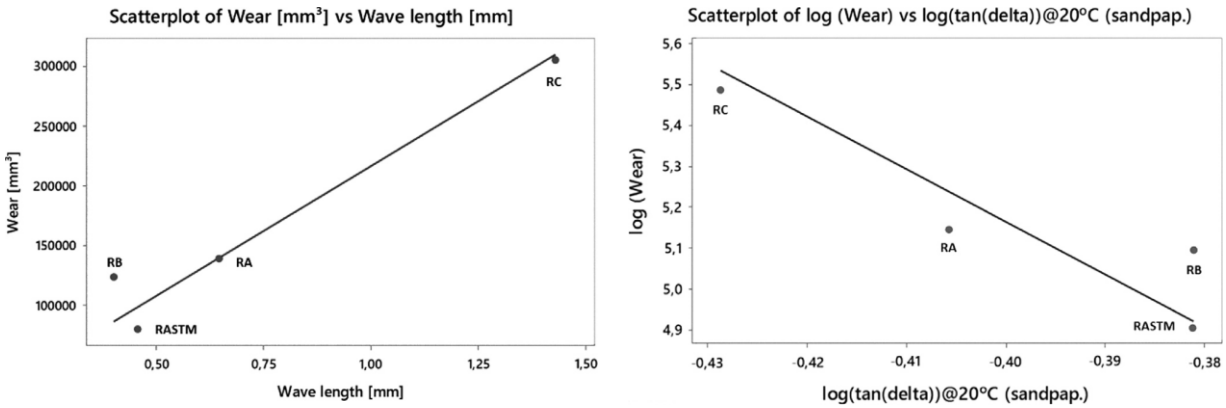

(A) **(B)**

Fig 2.18: (A) Correlation between Wear Volume Loss and Surface Wavelength (B) Correlation between Wear Loss and Tangent Delta [34]

It is also concluded that rubber with high friction performance also has high adhesive friction. A great degree of correlation was also found between the product of friction and wear and tangent delta. Correlation between log tangent delta and log of wear is also evident as shown in Fig 2.18. This also helped prove the fact that wear rate is dependent on the viscoelastic properties.

Many physics-based friction and wear models can quickly become very mathematically intensive and highly convoluted and sometimes may be dependent on parameters that need a lot of data and complicated testing methods. These theories can be simplified by making certain assumptions but still maintaining reasonable accuracy. One such study by Abraham et.al [30] is reviewed. The study aims to propose a new fatigue wear simulation model using lab test results and a simplified abrasion equation. The author cites a research study by M.M. Resnikowskij on tire wear [35]. Resnikowskij, like many other researchers, also assumed that the volume abraded (ΔV) is proportional to work done by friction (ΔW). He defined a new term called frictional resistance (β) which is the ratio of these two terms given by Eq. (2.18).

$$\beta = \frac{\Delta W}{\Delta V} = \mu.\ N.\frac{\Delta l}{\Delta V} \tag{2.18}$$

Where, μ is COF, N is normal load and Δl is friction length. Furthermore, he assumed that there must be a wear thickness δ which will be abraded and separated due to wear after a characteristic length of l_o.

Also, $l_o = z\,.n$, where z is the average distance between two projections and n cycles to failure. Also,

$$V_o = \delta A_o \tag{2.19}$$

Where A_o is wear area and V_o is characteristic volume loss. Combining Eq. (2.18) and Eq. (2.19), we get Eq. (2.20).

$$\beta = \frac{\mu \cdot N \cdot z}{A_0} \cdot \frac{n}{\delta} \tag{2.20}$$

The author further assumed two theories to hold and be incorporated in the equation: 1) relationship between fatigue and indenter tests as given by Kragelskij [36] and the Hertz theory of contact for incompressible materials [37]. This results in Eq. (2.21) given below.

$$\beta = \frac{\mu}{k'\pi\ 0.68}\left(\frac{\sigma_o}{k"}\right)^b \left(\frac{N}{A_o}\right)^{\frac{1-b}{3}} E^{\frac{2}{3}(1-b)} \left(\frac{Z}{r}\right)^{\frac{5-2b}{3}} \tag{2.21}$$

Where, σ_o is single loading strength, E is the modulus, r is asperity radius, k' is penetration constant,k" is penetration stress constant, b is fatigue resistance coefficient. Eq. (2.21) was further simplified by assuming some terms as constants, which gives us the simplified Eq. (2.22.

$$\beta = \mu\,(f_z)^b\ G^{2(1-b)/3}\ \ (k_\alpha)^b \tag{2.22}$$

Where, G is dynamic shear modulus, f_z is tensile strength, k_α is fatigue wear coefficient, b is fatigue wear steadiness. Lab tests were conducted on a DIN abrasion tester at various loads and specimens. Road tire tests were also conducted for 22400 km. It was observed that there was no correlation between DIN abrader results and road tire wear results. The correlation of Eq. (2.21) with road tire wear was excellent. The correlation between modified Eq. (2.22 and road tire wear is also good.

2.6 RUBBER AGING MODELS

Polymer aging prediction is challenging especially because of the complex rubber microstructure and the entangled crosslinks. Different types of factors that cause aging have been discussed in

Section 1. It is observed in research studies that thermal aging leads to chain scission, generation of extra crosslinks in the rubber network, oxidation of macromolecular chains, and consumption or migration of additives such as antioxidants, stabilizers and degradation or cracking of surface [38]. The increase in crosslink density (CLD) due to aging has been a subject of many studies. CLD is affected by the availability of oxygen, oxygen diffusion and permeability, double bonds in the main chain, pressure, the temperature of exposure as well as time.

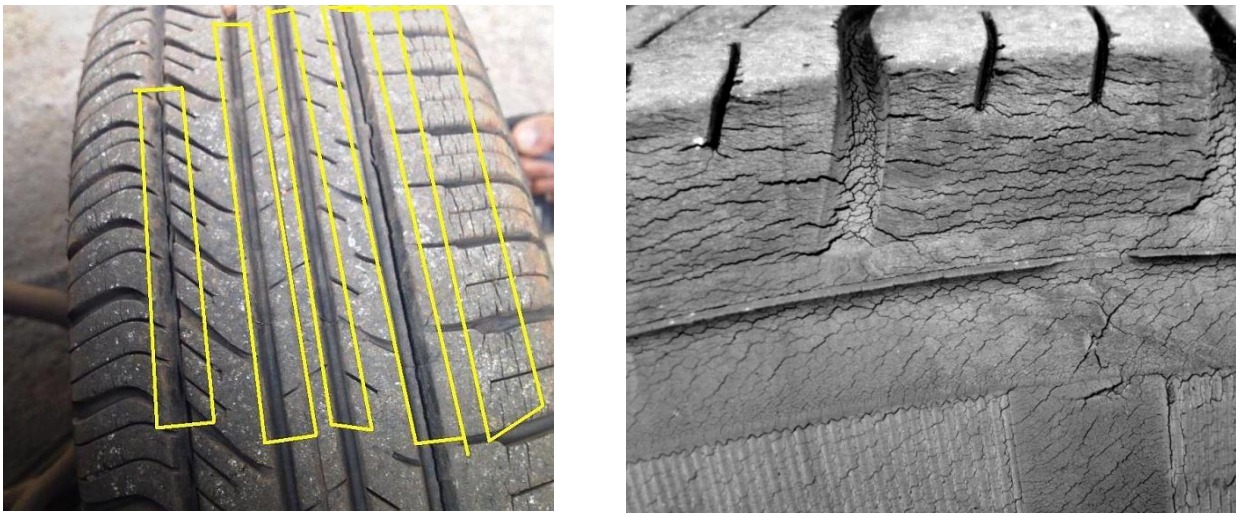

(A) **(B)**

Fig 2.19: (A) Circumferential Cracks on Tires due to Aging (Age: 4.3 years, Mileage: 11,000 miles) (B) Cracks on Tire Sidewall due to Rubber Aging

Jieying Zhi et.al [39] studied the effects of accelerated aging on the macromolecular and mechanical properties of SBR and proposed a constitutive model. They observed a rise in storage modulus in the rubbery region with an increase in the glass transition temperature as well. The change in tensile strength and elongation at break with aging time is shown in Fig 2.20.

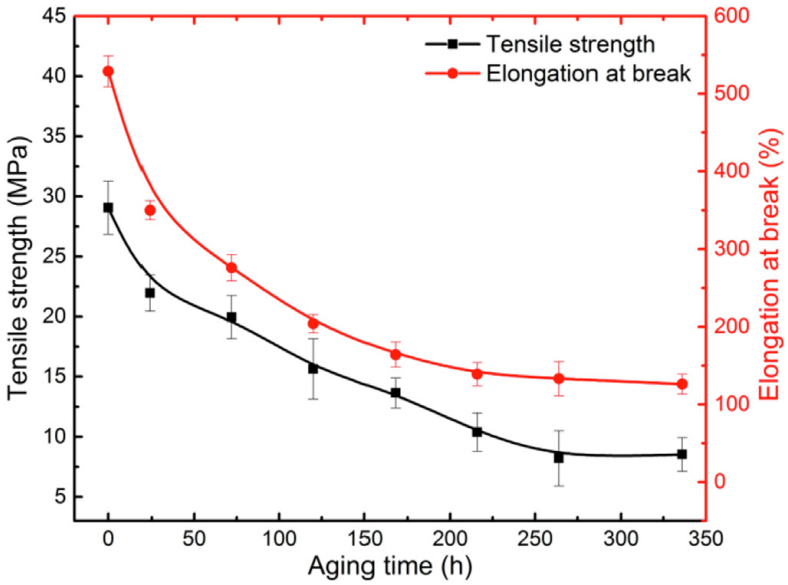

Fig 2.20: Change in Tensile Strength and Elongation at Break with Aging Time [39]

The change in CLD with aging time is shown in Fig 2.21. We observe that initially, the rate of CLD increase is slow, then it increases with aging time and again decreases with further aging, thus following an S-shape behavior.

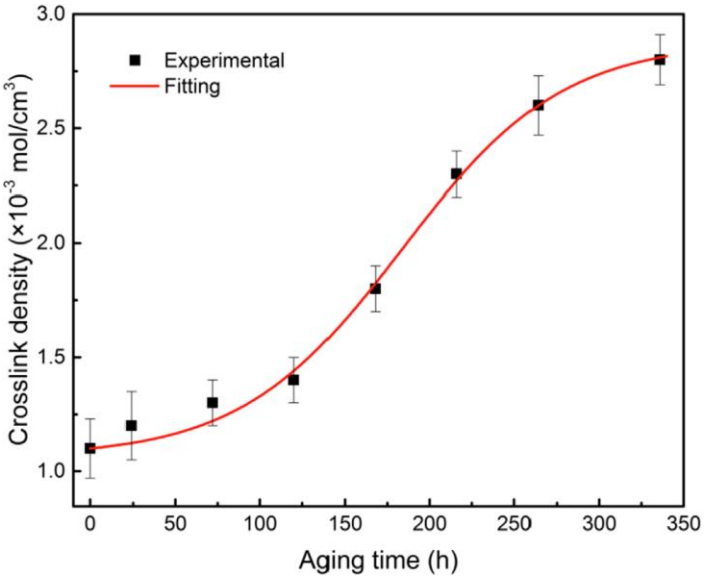

Fig 2.21: Change in CLD with Aging Time [39]

However, this research only studies the effect of aging at only one aging temperature, 120 °C and, different aging temperatures may affect this process. Moon et al [40] gave a unique perspective of using a parallel spring model to characterize aging in Natural Rubber/ Butadiene

rubber (NR/BR) blends. Accelerated aging was carried out at 70 ℃ to 100 ℃ and for 17 to 35 days. They tried to establish a robust relationship between the change in mechanical and chemical properties, especially CLD. Results showed a linear relationship between the strain-energy density (SED) and the CLD. The increase in CLD is modelled as adding a spring in parallel to the existing network of springs which increases stiffness. Studies have also been conducted to evaluate the evolution of network structures as NBR is aged. Aging was carried out at 60 ℃, 80 ℃, 100 ℃ and 125 ℃. Low dimensional NMR, solvent extraction and swelling, infrared spectroscopy and other mechanical measurands were conducted. [41] A major focus was on the CLD and how its increase influenced the density and hardness of the network. FTIR was used to correlate trends in CLD with chemical structural changes.

Aging is quite a slow phenomenon that may take months or years to study and model at room temperature. Thus, to speed up the rate of reactions as well as the degradation, artificial aging methods are employed. These methods subject the polymer under study to elevated conditions (temperature, pressure, radiation, etc.) and thus accelerate the aging process. The primary goals of accelerated aging are, lifetime prediction for a set time and conditions, selecting appropriate materials for a particular environment, understanding the degradation mechanisms and also for the creation of novel durable materials.

An example of an application where aging has been studied extensively in the past years is the automotive tire. The history of tire aging awareness can be traced back to 1985, when Uniroyal, a tire manufacturer voiced its concerns about tire safety of new radial tires which claimed to last much longer than old-styled bias tires [42]. Later, in the early 1990s, the uproar over Ford Explorer rollovers failed to emphasize the tread separation occurring in tires older than six years. After over a decade, in 2005, NHTSA proposed testing tires for aging and developing a standardized test to measure the effects of tire aging. In 2007, NHTSA presented its research findings in the form of a report to Congress. An interesting observation made was, that 77% of tire-related insurance claims came from five ‘hot-climate’ states and almost 84% due to tires older than six years [20]. However, there are still no hard regulations regarding tire age, and it is recommended to check with the concerned tire manufacturers about their tire life.

It has been observed that in regions of very high temperatures such as Phoenix, AZ a common failure mode for tires is the belt and tread separation, which can lead to catastrophic accidents. These failure modes have led to one of the largest tires recalls in the history of automobiles [43]. Aging also has adverse effects on abrasion resistance and hence mileage and fuel efficiency. Dynamic loading and tire-road interaction can lead to heat build-up due to friction and rolling resistance. NHTSA has studied, the implications of aging on the physical and chemical properties of tire components, in both lab as well as field conditions.

There have been several studies in the past decade which focus on the aspects of aging and degradation of various elastomers. Some focus on one specific factor such as thermal or ozone aging while others try to couple different factors to study their interactions. Svetlana et al [3] performed aging tests on polyurethane rubber to monitor changes in compression elastic modulus, shore A hardness, rebound coefficient and change in volume. They observed decreased volume, increased hardness, increased elastic rebound and increased compression static modulus. Accelerated aging was also conducted by Qiaobin et al [44] at 50 ℃, 60 ℃, 70 ℃ and 80 ℃. A Weibull distribution was used to describe the failure life of rubber under alternating stresses. Chauoki and Salima [45] conducted experiments to observe the influence of thermal and ultraviolet (UV) aging on polypropylene and natural rubber blend polymer. They also studied the influence of percentage rubber in the compound on the structure and properties of the blend. They observed a pronounced decrease in strain and strength properties of blend after thermal and UV aging as compared to only thermal aging, which also suggests stiffening of the blend. Further investigation also showed cracks on the sample surface and debonded rubber from the matrix. Sima et al [46] also observed that stress and elongation at break are affected to a great extent by aging process on silicone rubber. Also, the tests were carried out anaerobically (nitrogen was used) and hence, there was no extra crosslinking and hence no stiffening. This explains the decrease in Young's modulus due to aging. They also observed an increase in tear-resistance and hardness initially which fell off as aging progressed. FTIR and Scanning Electron Microscopy (SEM) were used to understand the surface morphology and brittle behavior. Svetlana et al [4] also studied the implications of aging (3 years) on the damping capabilities of absorbers, which is yet another widely used application. They tried to mathematically model these changes using the viscoelastic Maxwell and Burgers model. They concluded from their

study that aging tends to increase the natural frequency, decrease damping capacity, and decrease the restitution coefficient of elastomers.

Another interesting method to predict rubber aging was explored by Hong et al [47]. They used three neural network methods to predict aging life of nitrile butadiene rubber (NBR) gaskets. Hong et al [48] tried to consolidate all the theories related to rubber fatigue aging as well as experimental methods to create a software that can predict rubber aging life. They divided the theories into four prediction categories, curve model, computer simulation model, material model and experimental simulation model. Similar to Moon et al, a study was conducted by Jie et al that also showed a linear trend in the CLD with aging time, but for NBR [49]. The samples were aged at 65 ℃ for up to 90 days. Aging led to a decrease in elongation at break, increased surface roughness, increased void size and occurrence of white spots. An interesting observation was the increase in tensile strength up to a critical value and then a steady decrease upon further aging. As the CLD increased, the network became stable and relative movement of network chains decreased. But after reaching a critical value, due to less mobility, the stress distribution was affected and hence decreased the tensile strength.

Li et al [50] studied the effects of the addition of different carbon black contents to the natural rubber (NR) and the effect of thermal and UV aging on the hardness, elongation, and tensile strength. They also confirmed that with aging, the network density increases, and pores and voids are formed on the surface compromising the elasticity. Rami and his research group [51] have performed an extensive analysis of aging effects on neoprene rubber in tension and compression. Aging was performed at 70 ℃, 80 ℃ and 90 ℃. They observed an increase in young's modulus, no change in bulk modulus, slight decrease in poison's ratio. They further observed that these properties follow an Arrhenius or pseudo-Arrhenius behavior. They also linked the young's modulus to the elongation at break and hardness and thus were able to use it for lifetime prediction. C.L. Dong et.al [52] studied the aging effects on the tribological properties of Nitrile Butadiene Rubber (NBR). They observed that the Shore A hardness increased, tensile strength and tear strength decreased, friction coefficient increased, average wear loss increased with an increase in aging time and temperature. Surface profilometry as well as Scanning Electron Microscopy (SEM) was performed on the samples to better understand the tribological properties of NBR.

Jieying et al [39] addressed the mechanical and microstructure changes in SBR due to thermo-oxidative aging from experimental and modeling aspects. The samples were aged at 120 ℃ for up to 336 hours. They observed that chain scission and crosslinking occurred simultaneously, and the dominant reaction decides the mechanical properties of the polymer. Thus, aged rubbers have both increased crosslinks as well as increased dangling chain ends. Viscoelastic and hyperelastic properties are modelled based on macromolecular changes. However, the study does not explore the change of aging kinetics as aging temperature changes. Other thermo-oxidative aging studies also explore the effects on mechanical and chemical properties for NBR and SBR. [53][54]. Kewei et al [55] studied aging effects on Butyl rubber (60 -100 ℃) and predicted lifetimes using Arrhenius based approach. They observed that, unlike other studies, the degradation of properties of butyl rubber with aging time, do not follow a linear relation. They further investigated the activation energies at low and high temperatures and concluded that degradation processes with lower activation energies dominate the low-temperature region and the higher activation energy processes dominate at higher temperatures. Ahmed Korba [56] has conducted thorough research on aging effects on hyperelastic response and documented it in his PhD dissertation. He defined a simple With Function Bases (WFB) model (based on the Yeoh model and Continuum mechanics) to predict the hyperelastic response as a function of aging time, temperature. However, it takes a long time to define the model parameters. Also, the error is quite high at aging temperatures above 115 ℃.

As rubber compounds are widely used in the tire industry, a lot of efforts have been put to understand the effects of aging on the tire lifetime and its effects on the performance characteristics as well. One such study investigates the aging effect on tire force and moment (F&M) characteristics. [57] [58]. The researchers concluded that cornering stiffness increased with aging and the overturning moment decreased with aging. However, they did not find any strong correlation between tire age and peak lateral force. Baldwin, Bauer, Elwood have conducted many studies [59]–[64] in the past that investigate different aspects of tire aging such as conducting field tests, lab accelerated aging studies, correlating these two results, etc. Peel strength, tensile strength, elongation and swelling ratio were studied. Effects of changing partial pressure of oxygen, diffusion-limited oxidation (DLO), Arrhenius based lifetime prediction were some of the areas that were studied.

3. PREDICTIVE MODELLING OF HYPER-ELASTIC RESPONSE DUE TO AGING

The word ‘Hyperelasticity’ can be broken down into two words- ‘hyper’ meaning excessive and ‘elasticity’ meaning ability to be stretched. Thus, simply understood, it related to materials being stretched excessively. Hyperelasticity can be defined as a theory or material model which is used to capture the large strain, non-linear elastic behavior of certain types of materials such as elastomers, thin films, soft tissues, etc. As opposed to linear elastic material wherein the stress varies linearly with strain (at least for small deformations), for hyperelastic materials, the stress varies non-linearly with strain. This can be seen in Fig. 3.1. For linear elastic material, ‘Hooke’s law’ is used which states that strain is directly proportional to the stress applied. For such homogenous, isotropic materials, which do not show a non-linear stress-strain behavior, it is possible to model them using just two material constants: young’s modulus and the Poisson’s ratio. However, rubber on the other hand can undergo large deformations and still return to its original shape (with low plastic deformation) due to its strong and compliant cross-linked structure. For such hyperelastic materials like SBR, modeling the strain energy is more complex and there is always a need to have one or more constants to accurately fit the data. They are modelled using a Strain Energy Density (SED) function which provides this relationship between stress and strain. Many SED potential functions exist, however not all of them can predict the stress-strain response fully and accurately at all strains. They can be analyzed based on the following main qualities:

1) The model should be able to match the ‘S-shape’ curves which are typically observed in hyperelastic materials as seen in Fig. 3.1. The upturn nature of the curve is especially difficult to model [65].
2) The model should work for all deformation modes. E.g., if the model accurately represents uniaxial tension data, then it should also do that for shear or biaxial and triaxial extension data as well.

3) The stability of the model should be ensured by using different criteria. The most popular one is Drucker's stability criterion.
4) The material parameters of the model should be less which will further ensure better stability as well as reduce the number of experiments and deformation modes.
5) Finally, the model should not be overly complex and mathematically intensive and have some physical meaning to its fitting constants.

Classification and in-depth discussion of different hyperelastic models will be done in the subsequent sections.

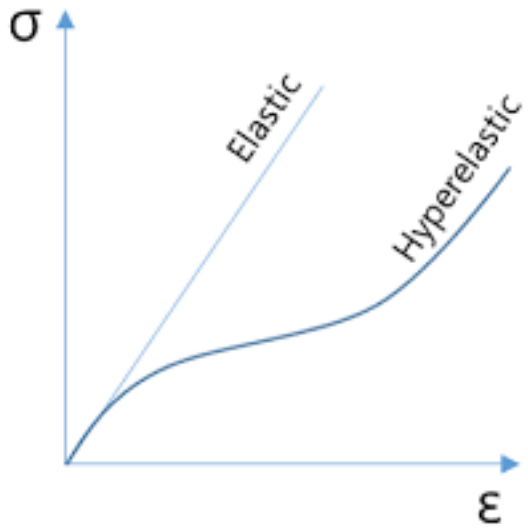

Fig. 3.1: Stress-Strain Response of Linear Elastic and Hyperelastic Materials

Studies have been conducted that try to model rubber aging by defining a new hyperelastic model [5]. Other studies try to predict the stiffness and strain at break for different aging conditions. However, there has been no study to model rubber aging based on the CDM approach. This chapter aims to develop a novel yet simple model that can capture the thermo-oxidative aging effects on the large-strain response of SBR under accelerated aging. This is done by modifying the existing hyperelastic models to incorporate the aging effect. The study will focus on observing changes in the tensile strength and elongation at break for SBR at different aging time periods and temperatures. The study also focuses on eliminating Mullin's effect in aged rubbers, which many studies have not considered in the past. Finally, a user material subroutine (UMAT) is developed in ABAQUS to simulate the SBR response as a function of

aging time and temperature. Fourier Transform Infrared Spectroscopy (FTIR) is used to study the changes in the chemical composition based on the FTIR spectra.

3.1 THEORETICAL BACKGROUND

The various models used to represent the nonlinear behavior of the stress-strain curve of rubber subjected to large deformations can be divided into two main categories:

1) **Physical/ Mechanistic models** - These models are based on the molecular structure of the material
2) **Phenomenological models -** These models are mathematically tailored to fit the experimental data using certain constants

However, one cannot draw a clear line and distinguish the phenomenological models from the physical ones as some phenomenological models have shown to have captured the physical behavior of these materials as well. For most of the hyperelastic models out there, the stress-strain response is derived from a SED function. Based on the SED function, the hyperelastic models can again be categorized as:

1) Statistical Mechanics based
2) Invariant based (continuum mechanics)
3) Stretch ratio-based (continuum mechanics)

The major issue with developing a new hyperelastic model is to capture the accurate non-linear stress-stretch behavior, ensuring stability and applicability for all deformation modes. All these complexities will be discussed later in this section. However, to do this, some background knowledge of Continuum and Solid mechanics is needed. We start by defining what is a SED function and work our way in.

1) **SED function (W)** [66]

When an elastic material is deformed or loaded, work is done on the material. This work done is stored as recoverable 'strain energy' in the solid. When the same material is allowed to relax, and return to its original unloaded condition, work is done by the material. If the material comes backs to its original configuration without any damage or external stress, then it is completely

elastic. However, if there is a permanent set of deformation in the material, then it is not completely elastic (plastic strain). Thus, strain energy density can be defined as the work done per unit volume of a material to deform it from an unloaded (zero stress) state to a loaded state. This SED function is represented by *W* and is a function of the deformation gradient tensor **(F).** Thus, *W= W(**F**)*

2) Deformation Gradient (F)

As the name suggests, the deformation gradient is the measure of deformation occurring in a system from its reference configuration (X) to its current new configuration (x) as seen in Fig. 3.2.

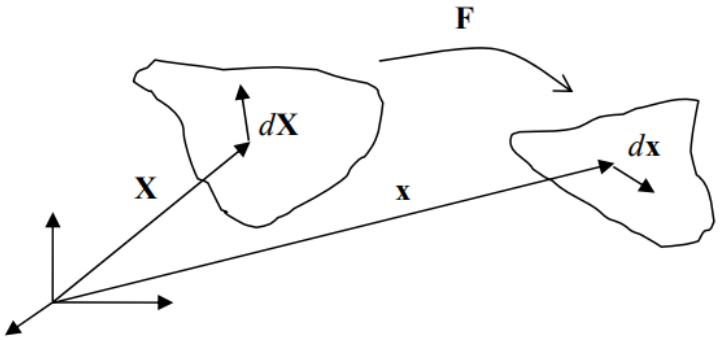

Fig. 3.2: Mapping of Deformation from Reference to New Configuration

3) Cauchy-Green Strain Tensors

The deformation tensor can provide information about the mapping of the element from a reference configuration to the current configuration. However, it is unable to give information about rigid body translations. Thus, the 'Left Cauchy-Green Strain (B)' and 'Right Cauchy-Green Strain (C)' tensors given by Eq. (3.1)and Eq. (3.2) respectively, are used to measure the changes between element lengths and angles as they are deformed.

$$\mathbf{C} = \mathbf{F}^{\mathbf{T}}\mathbf{F} \tag{3.1}$$

$$\mathbf{B} = \mathbf{F}\,\mathbf{F}^{\mathbf{T}} \tag{3.2}$$

1) Stretch/ Stretch Ratio ($\boldsymbol{\lambda}$)

The stretch ratio is simply defined as the ratio of the length of the deformed element to that of the same undeformed element as seen in Eq. (3.3).

$$\lambda = \frac{|d\mathbf{x}|}{|d\mathbf{X}|} \tag{3.3}$$

When $\lambda = 1$ the material is unstretched, $\lambda < 1$ material is under compression and for $\lambda > 1$ material is under tension. For a simple example of stretch (simple triaxial extension) only in the principal axes (X, Y, Z) which are mutually orthogonal to each other, and represented by $\lambda_1, \lambda_2, \lambda_3$ respectively, the deformation gradient can be represented by,

$$\mathbf{F} = \begin{bmatrix} \lambda_1 & 0 & 0 \\ 0 & \lambda_2 & 0 \\ 0 & 0 & \lambda_3 \end{bmatrix}$$

For the case of uniaxial extension, say in X direction, $\lambda_1 = \lambda \; and \; \lambda_2 = \lambda_3 = 0$

$$\mathbf{F} = \begin{bmatrix} \lambda & 0 & 0 \\ 0 & 0 & 0 \\ 0 & 0 & 0 \end{bmatrix}$$

Thus, from the above parameter definitions, we see that the SED function is actually a function of the stretch ratios and the 'invariants' of the strain tensors, Eq. (3.4). Thus,

$$W(\mathbf{F}) = U(I_1, I_2, I_3) = \widetilde{U}(\lambda_1, \lambda_2, \lambda_3) \tag{3.4}$$

where,

$$\begin{gathered} \boldsymbol{I_1} = tr(B) = B_{kk} = \lambda_1^2 + \lambda_2^2 + \lambda_3^2 \\ \boldsymbol{I_2} = \frac{1}{2}(I_1^2 - \mathrm{B} \cdot \mathrm{B}) = \frac{1}{2}\left[(I_1^2 - B_{ik}B_{kj}\right) = \lambda_1^2\lambda_2^2 + \lambda_2^2\lambda_3^2 + \lambda_3^2\lambda_1^2 \\ \boldsymbol{I_3} = \det \mathrm{B} = J^2 = \lambda_1^2 \, \lambda_2^2 \, \lambda_3^2 \end{gathered} \tag{3.5}$$

3.2 EXPERIMENTAL SETUP

3.2.1 Material and Sample Geometry

The material under study is a tire tread compound supplied by Sumitomo Rubber Industries (SRI), Kobe, Japan. The formulation for the compound in parts per hundred rubber (phr) is shown in Table 3.1.

Table 3.1: Formulation of SBR Tread Compound

Component	phr
SBR	100
Filler- Carbon Black	20
Silicon	40
Antioxidant-A	2.22
Antioxidant-B	0.88
Stearic Acid	1.5
Zinc Oxide	2.2
Coupling Agent	2.4
Wax	1.78

The material is sourced as sheets of dimensions 150 mm by 10 mm and ~ 0.6-0.65 mm thickness. The SBR sheets are stored in cold storage before artificial aging to prevent any pre-aging of the material. Hourglass/dog-bone shaped samples for hyperelastic study are cut out from the sheet as seen in Fig. 3.3. using an ASTM mold, with an overall length of around 70 mm, grip width 10 mm and gauge width 6mm. They are stored at ambient temperature for 3 hours before testing.

(A) **(B)**

Fig. 3.3: (A) Dogbone Shaped Samples used in Hyperelastic Testing (B) SBR Sheet from which the Samples are cut

3.2.2 Hyperelastic Tests

Hyperelastic uniaxial testing is performed on the aged samples on the INSTRON 2710-002 machine as shown in Fig. 3.4. The rating of the load cell used is 1 kN. Tests are conducted at a strain rate of 0.5 mm/sec. Two types of tests are conducted, 1) elongation until failure 2) cyclic loading and then elongation until failure. In the first type of test, the samples are loaded at the above-mentioned strain rate and stress-strain data is collected till failure. In the second type of test, the sample is first subjected to a certain number of loading and unloading cycles up to 400% strain and then finally elongated until failure. This is done to eliminate the 'Mullin's Effect.'

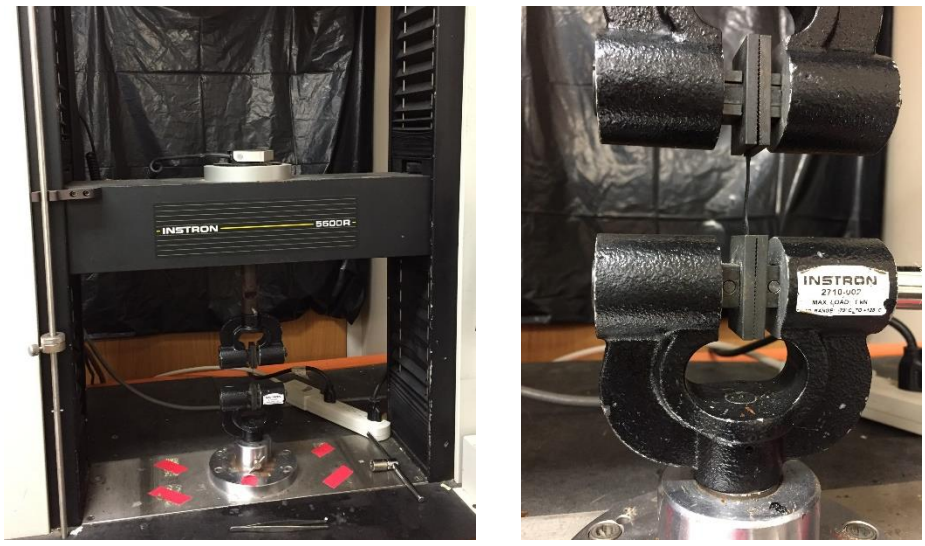

Fig. 3.4: Instron Machine with Sample Mounted

Mullins [67] observed that the stress-strain curve for elastomers changes when the sample is loaded repeatedly for the first time. He observed that the subsequent curves are generally below the first loading curve. This softening behavior of elastomers after the first cycle is called Mullins' effect. During the experimentation, such behavior was also observed for the aged samples as well as seen in Fig. 3.5 (A). The stress and strain profiles of the loading and unloading cycle can be seen in Fig. 3.5 (B) and (C). A stable response was needed to gather accurate data for the model.

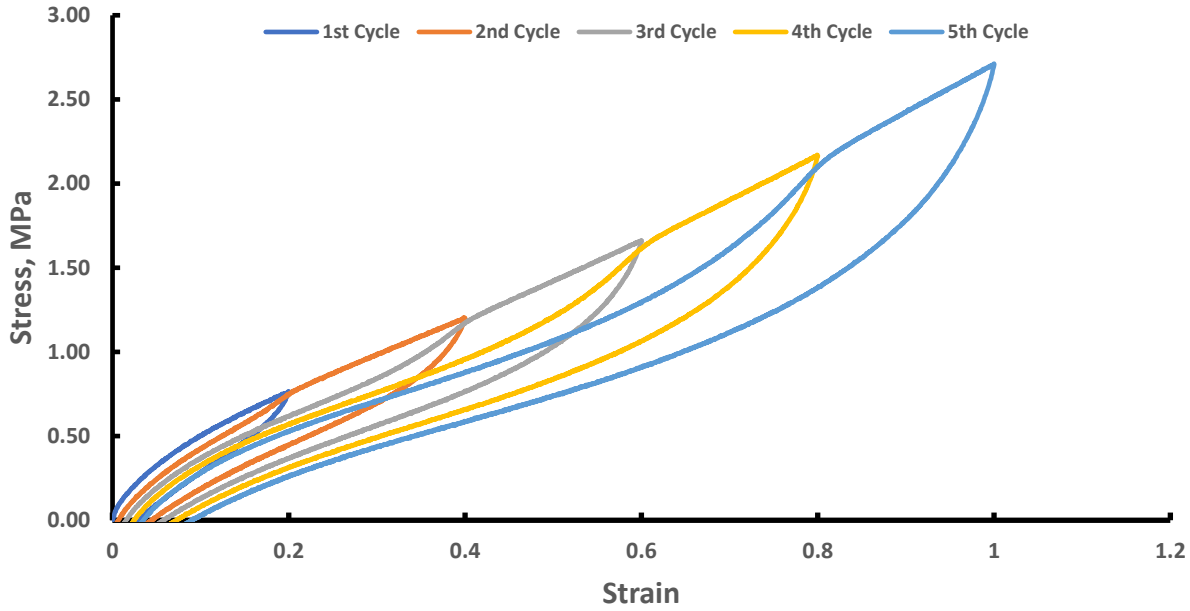

(A)

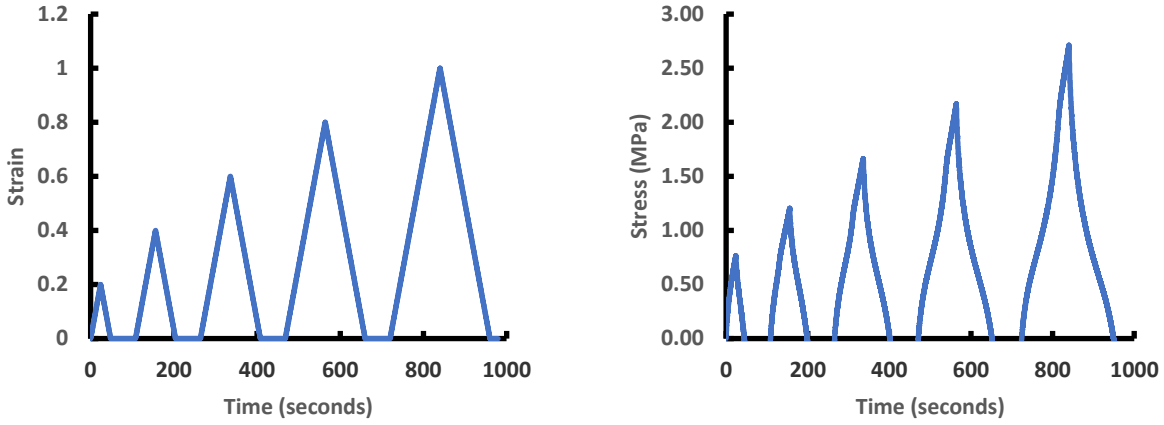

(B) (C)

Fig. 3.5: (A) Repeated Cyclic Loading of Sample (B) Strain Profile and (C) Stress Profile of Loading and Unloading

Hence, the samples were loaded and unloaded for 7-8 cycles, till the curve came to equilibrium as shown in Fig. 3. 6 (A). Then, the sample was allowed to relax for 10 minutes and then loaded till failure. The final loading curve for all samples was used for the study as seen in Fig. 3. 6 (B). For each aging condition, three samples were tested, and the average of the data was used for final analysis.

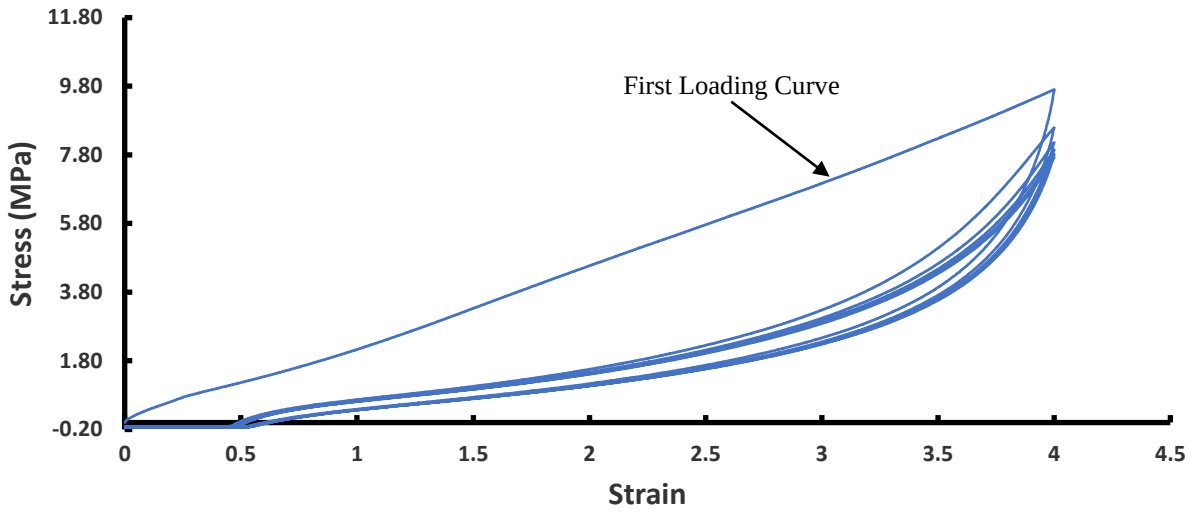

(A)

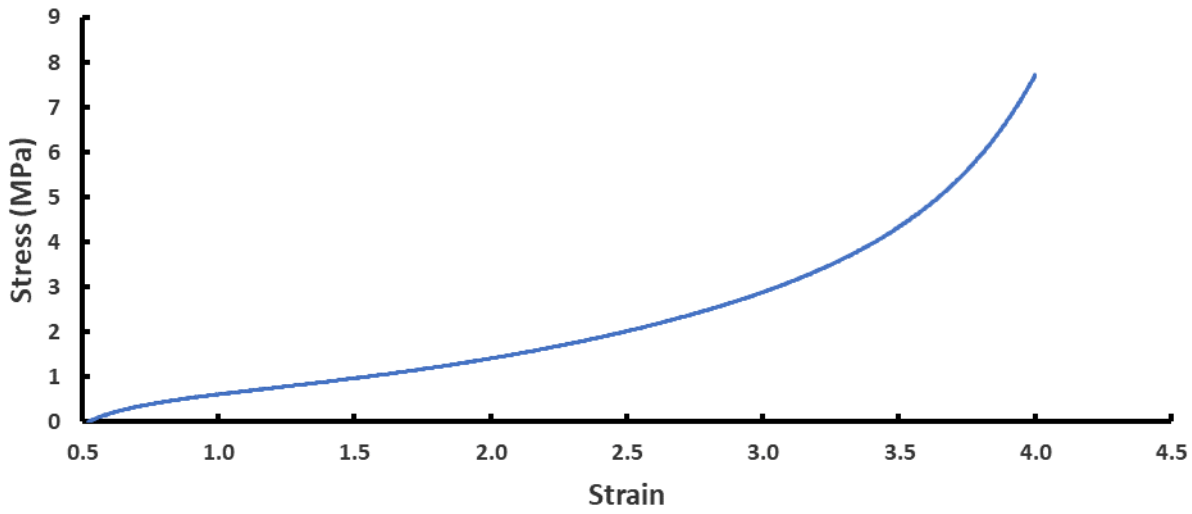

(B)

Fig. 3. 6: (A) Cyclic Loading and Unloading up to 400% Strain (B) Final Stable Loading Curve

3.2.3 Aging Chamber

As discussed in the earlier sections, the aging process is accelerated by subjecting the samples to elevated temperatures. Studies have shown that there is a direct correlation between temperature

and oxygen diffusivity in the rubber [68]. A vacuum aging oven as shown in Fig. 3.7 is used for this purpose with a continuous supply of air. This ensures that aging is aerobic in nature, instead of anaerobic. Oven aging is carried out in accordance with the ASTM D573-04- 'Standard Test Method for Rubber Deterioration in Air Oven.'[69] Samples were placed such that their entire surface is exposed evenly.

Fig. 3.7: Vacuum Aging Oven for Accelerated Aging

3.2.4 FT-IR ATR

FTIR analysis was performed to study the aging chemistry and kinetics. Fig. 3.8 shows the working of the FTIR-ATR. In the ATR crystal, an incident infrared beam is reflected multiple times by the sample. The intensity changes of the infrared beam after interacting with the sample is measured by the detector.

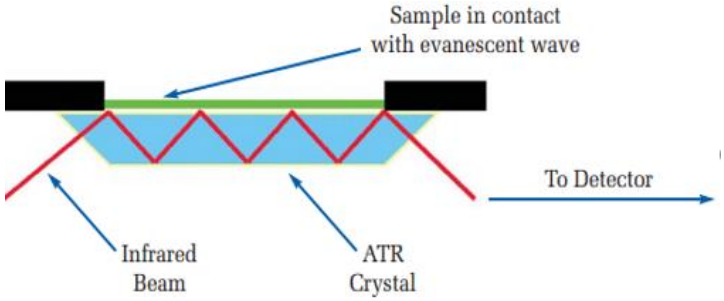

Fig. 3.8: Working of FT-IR

Compared to the conventional FTIR device, FTIR-ATR measurement is non-destructive and quick. The FTIR characterization was performed using a PerkinElmer ATR-FTIR (model Spectrum 100), Fig. 3.9 in the range of 4000–1000 cm^{-1} with 256 scans at room temperature.

Fig. 3.9: PerkinElmer ATR-FTIR (model Spectrum 100)

3.2.5 Test Matrix

Table 3.2 shows the test matrix used for this study. Samples were aged at 70 ℃, 90 ℃ and 110 ℃ for a period of 1, 2, 4 and 8 weeks. The different temperatures help us study the aging kinetics at low and high temperatures. For each given aging time and temperature, at least two samples were tested and their response was averaged out to get a final response which is shown in the following section.

Table 3.2: Aging Test Matrix

T (℃)	Aging Time (*weeks*)			
70	1	2	4	8
90	1	2	4	8
110	1	2	4	8

3.3 RESULTS

3.3.1 Hyperelastic Uniaxial Response

As per the test matrix, the hyperelastic uniaxial tensile tests were conducted for the given aging times and temperatures. Fig. 3.10 (A) shows the load-elongation curves for one such temperature of 90 °C and different aging times without the removal of Mullins effect. One of the most striking observations is that the stiffness or slope of these curves increases with aging time. As seen in Section 2.6, crosslinking and chain scission takes place simultaneously in the compound during aging. Depending on which reaction dominates the other, the material may either soften or harden overtime. In the case of SBR, the crosslinking increases and hence there is an increase in stiffness with aging time and temperature. However, the opposite is true for natural rubber (NR) compounds. Another observation is that the strain at break decreases drastically as the material is aged. This is because of the embrittlement and the damage occurring in the material due to aging and the formation of surface cracks and defects.

Mullin's effect is then eliminated, and these curves are also plotted as shown in Fig. 3.10 (B) up to a stretch ratio of 4.5. Again, we observe a similar trend where the slope of the curves increases with aging. This data is then filtered, and stress-stretch ratio curves are plotted which will be used for further analysis.

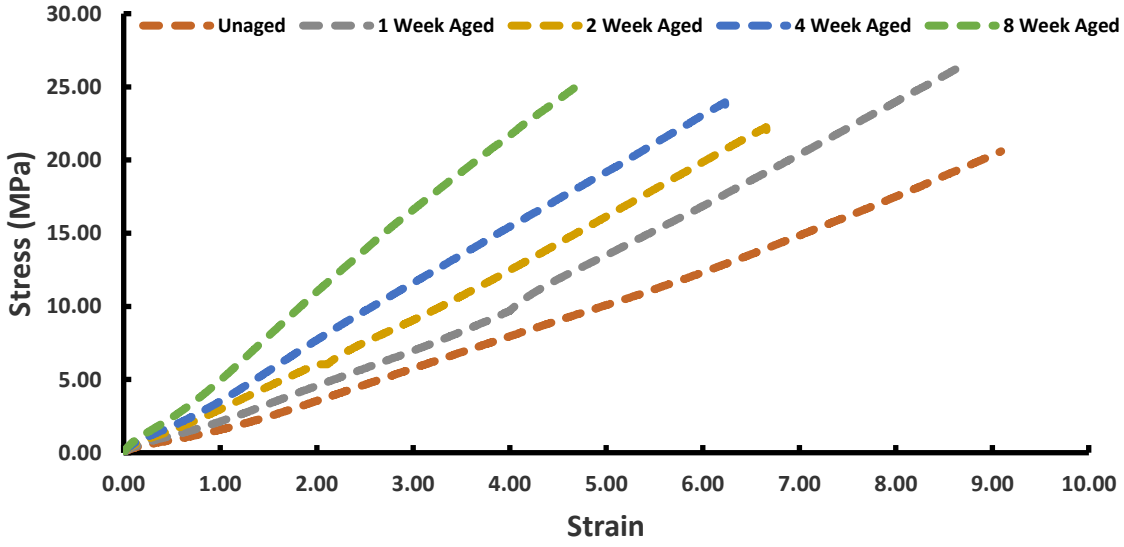

(A)

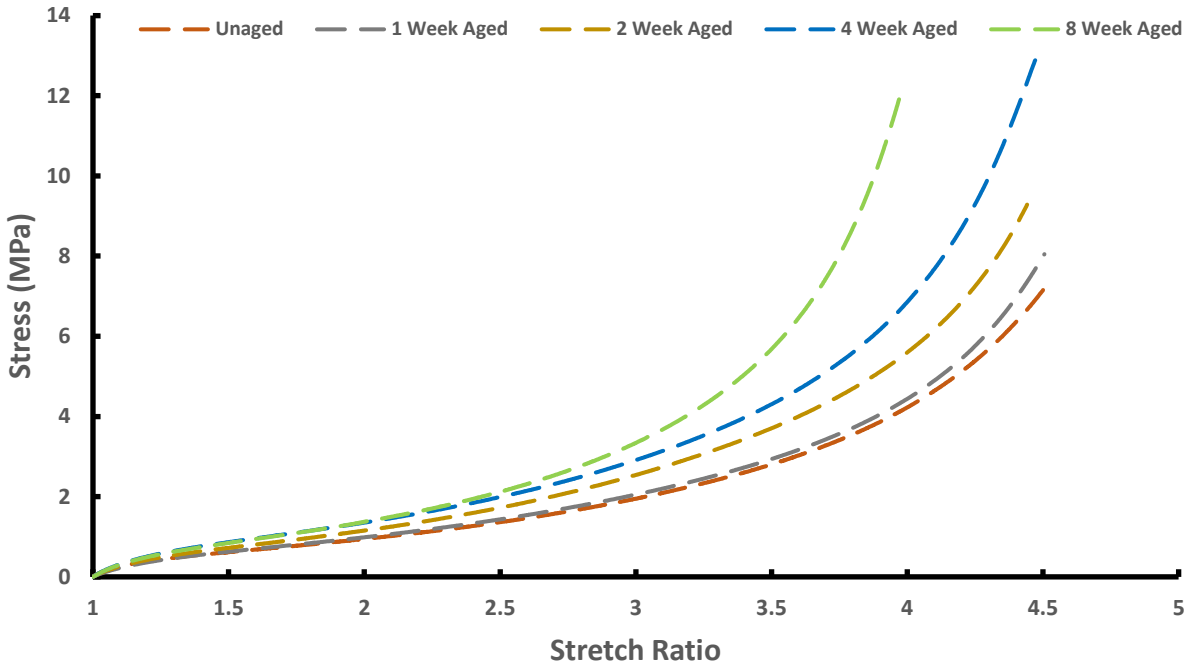

(B)

Fig. 3.10: Stress-Strain aged response curves (A) at 90 ℃ without elimination of Mullins effect (B) at 90 ℃ after removing Mullins Effect

3.3.2 FT-IR SPECTRA

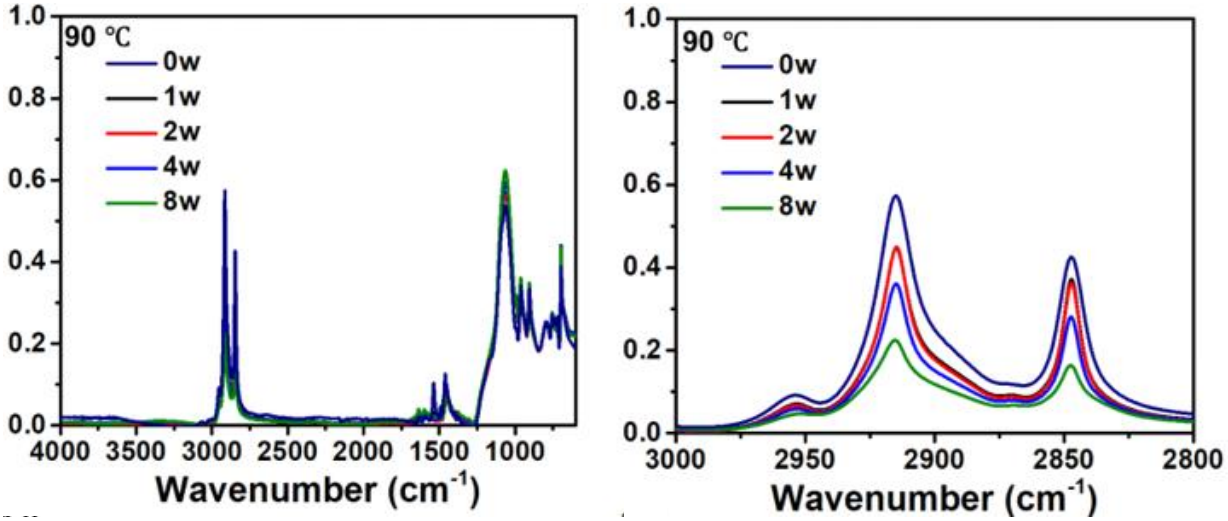

Fig. 3.11: FTIR-ATR Spectra (90 °C)

Fig. 3.11 shows the FTIR spectrum of samples for all aging times at 90 °C from 4000 cm^{-1} to 1000 cm^{-1} wavenumber. The region between 3000 cm^{-1} and 2800 cm^{-1} is of special interest, because it represents the C-H group. As observed in the above figure, the C-H groups are consumed as aging takes place. This is due to the different reactions taking place during aging. This led to a decrease in C-H stretching intensity over time. No carbonyl group and only weak hydroxyl groups were observed on the FTIR spectra. This is different from pure (no fillers or additive) rubber compounds which showcase a strong carbonyl signal between 1700 to 1800 cm^{-1}. The presence of fillers and antioxidants significantly retarded the oxidation reaction. The peaks at 1638 and 1580 cm^{-1} may be ascribed to the oxidation of the primary antioxidant, N-(1,3-dimethylbutyl)-N'-phenyl-1,4-benzenediamine (6PPD), generated quinone product (6PPDQ) after the thermal aging. The strongest peaks at 1080 cm^{-1} overlap with that of C-O-C bending, C-N bending, and SiO2. The peak intensity increased with aging time, indicating an oxidative crosslinking reaction during the thermal aging. The occurrence of crosslinking was also supported by the crosslinking density of the rubber, determined by Flory-rubber theory based on the elastic modulus. Which will be discussed in Section 4 of this thesis. The aging kinetics at other aging temperatures will be discussed in Section 6.

3.4 MODELLING AND ANALYSIS

3.4.1 Hyperelastic Material Modelling

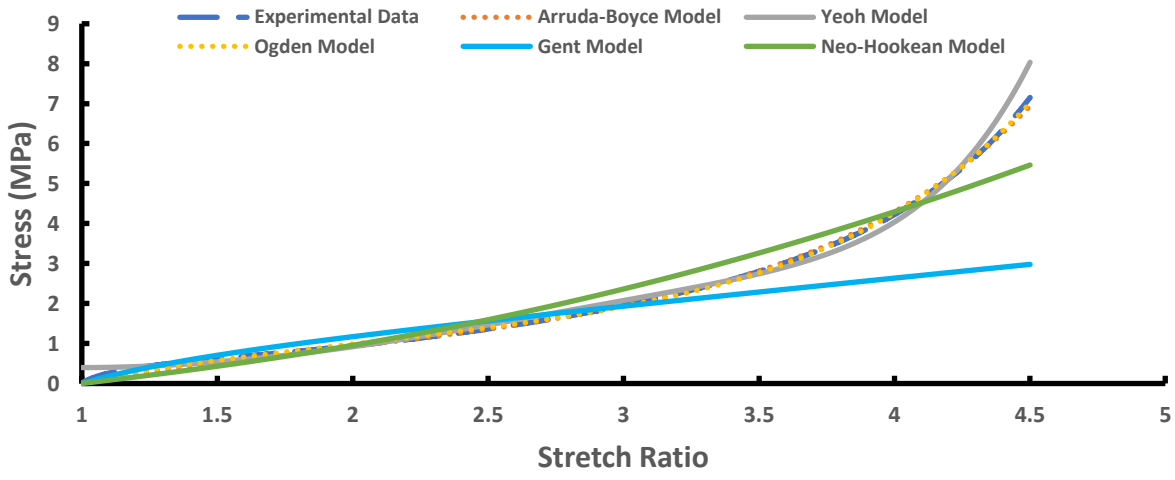

Fig. 3.12: Fitting various Hyperelastic models to Experimental data (unaged)

Many hyperelastic models have been formulated that can be used to characterize rubber stress-strain response over the past six decades. Some of the most widely used ones are shown in Table 3.3. However, these models are unable to capture the aging behavior of polymers. As seen in the previous sections, efforts have been made to predict the lifetime of rubber based on Arrhenius equations but few models can accurately predict entire aging curves. Hyperelastic models from Table 3.3. were compared to determine the best model for the present study. Of these, the Ogden, Yeoh, and Arruda-Boyce models were selected and compared for the accuracy of fit and stability using the actual data as seen in Fig. 3.12.

Table 3.3: Comparison of Hyperelastic Models [70]

Model	Strain Energy Desnity	Data Needed	Drucker Stability Criteria	Fit Accuracy	Notes
Neo-Hookean	$U = C_{10}(\bar{I}_1 - 3) + \frac{1}{D_1}(J^{el} - 1)^2$	At lest **one** deformation mode	C_{10} must be positive for stability	Low	One of the simplest model with only one fitting coeffcient
Yeoh	$U = C_{10}(\bar{I}_1 - 3) + C_{20}(\bar{I}_1 - 3)^2 + C_{30}(\bar{I}_1 - 3)^3 + \frac{1}{D_1}(J^{el} - 1)^2 + \frac{1}{D_2}(J^{el} - 1)^4 + \frac{1}{D_3}(J^{el} - 1)^6$	At lest **one** deformation mode	C_{10} *and* C_{30} must be positive and C_{20} can be negative if $\|C_{20}\| \ll \|C_{10}\|$ *or* $\|C_{30}\|$	Moderate	C_{20} helps model the upturn stiffness in the curve
Mooney-Rivlin	$U = C_{10}(\bar{I}_1 - 3) + C_{01}(\bar{I}_2 - 3) + \frac{1}{D_1}(J^{el} - 1)^2$	At lest **two** deformation modes	$D_{11} = 4(\lambda_1^2 + \lambda_2^2)\left(\frac{\partial U}{\partial \bar{I}_1} + \lambda_2^2 \frac{\partial U}{\partial \bar{I}_2}\right) + 4(\lambda_1^2 - \lambda_2^2)^2\left(\frac{\partial^2 U}{\partial \bar{I}_1^2} + 2\lambda_2^2 \frac{\partial^2 U}{\partial \bar{I}_1 \partial \bar{I}_2} + \lambda_2^4 \frac{\partial^2 U}{\partial \bar{I}_2^2}\right)$ $D_{22} = 4(\lambda_1^2 + \lambda_2^2)\left(\frac{\partial U}{\partial \bar{I}_1} + \lambda_1^2 \frac{\partial U}{\partial \bar{I}_2}\right) + 4(\lambda_1^2 - \lambda_2^2)^2\left(\frac{\partial^2 U}{\partial \bar{I}_1^2} + 2\lambda_1^2 \frac{\partial^2 U}{\partial \bar{I}_1 \partial \bar{I}_2} + \lambda_1^4 \frac{\partial^2 U}{\partial \bar{I}_2^2}\right)$ $D_{12} = D_{21} = 4\lambda_1^2 \frac{\partial U}{\partial \bar{I}_1} + 4\lambda_2^2 \frac{\partial U}{\partial \bar{I}_2} + 4(\lambda_1^2 - \lambda_2^2)(\lambda_1^2 - \lambda_2^2)\left(\frac{\partial^2 U}{\partial \bar{I}_1^2} + (\lambda_1^2 + \lambda_2^2)\frac{\partial^2 U}{\partial \bar{I}_1 \partial \bar{I}_2} + \lambda_1^2 \lambda_2^2 \frac{\partial^2 U}{\partial \bar{I}_2^2}\right)$ Material matrix D must be positive definite	High	Based on strain invariants.
Ogden	$U = \sum_{i=1}^{N} \frac{2\mu_i}{\alpha_i^2}\left(\bar{\lambda}_1^{\alpha_i} + \bar{\lambda}_2^{\alpha_i} + \bar{\lambda}_3^{\alpha_i} - 3\right) + \sum_{i=1}^{N} \frac{1}{D_i}(J^{el} - 1)^{2i}$	At lest **three** deformation modes	$\begin{bmatrix} D_{11} & D_{12} \\ D_{21} & D_{22} \end{bmatrix} = \sum_{i=1}^{N} 2\mu_i \lambda_1^{-\alpha_i} \lambda_2^{-\alpha_i} \begin{bmatrix} \lambda_1^{2\alpha_i}\lambda_2^{\alpha_i} + 1 & 1 \\ 1 & \lambda_1^{\alpha_i}\lambda_2^{2\alpha_i} + 1 \end{bmatrix}$ Material matrix D must be positive definite	High	Based on principal stretches. Can predict upturn stiffening. Stability reduces as coefficients increase
Arruda-Boyce	$U = \mu \sum_{i=1}^{5} \frac{C_i}{\lambda_m^{2i-2}}\left(\bar{I}_1^i - 3^i\right) + \frac{1}{D}\left(\frac{J_{el}^2 - 1}{2} - \ln J_{el}\right)$	At lest **one** deformation mode	Both the coefficients need to be positive to ensure stability	High	Based on expressing the molecular network of polymers by 8 chains oriented from the center diagonal of the microstructure
Gent	$U = -\frac{GJ_{lim}}{2}\ln\left(1 - \frac{\bar{I}_1 - 3}{J_{lim}}\right) + \frac{1}{D_1}(J - 1)^2$	At lest **two** deformation modes	-	Moderate	Baed on a logarithmic strain energy function

The stability of these models needs to be verified in order to choose a model which is stable at all strain ranges and deformation conditions. The 'Drucker' stability criterion is used to ensure that the quality of fit to the experimental data. The condition states that, for an incompressible material, the change in stress ($d\sigma$) due to infinitesimal change in logarithmic strain ($d\epsilon$) satisfies the following inequality

$$d\sigma : d\epsilon > 0$$

If this inequality is violated, then the model obtained is unstable. This can cause non-physical behavior and non-convergence. ABAQUS documentation has a comprehensive section on the Drucker stability and the conditions that must be met. For this study, these conditions were imposed while curve fitting to various hyperelastic models. The Drucker stability criterion for all models under study is compared in Table 3.3. The stability criterion for the Arruda-Boyce model is the simplest. It says that the initial shear modulus (μ) and locking shear (λ_m) should be positive.

Another important aspect of curve fitting is the cost function/error function that is used to minimize the error between the experimental data and the material model. The cost function is given by Eq.
(3.6).

$$RSS = \sum_{i=1}^{n} \left(y_i - f(x_i)\right)^2 \tag{3.6}$$

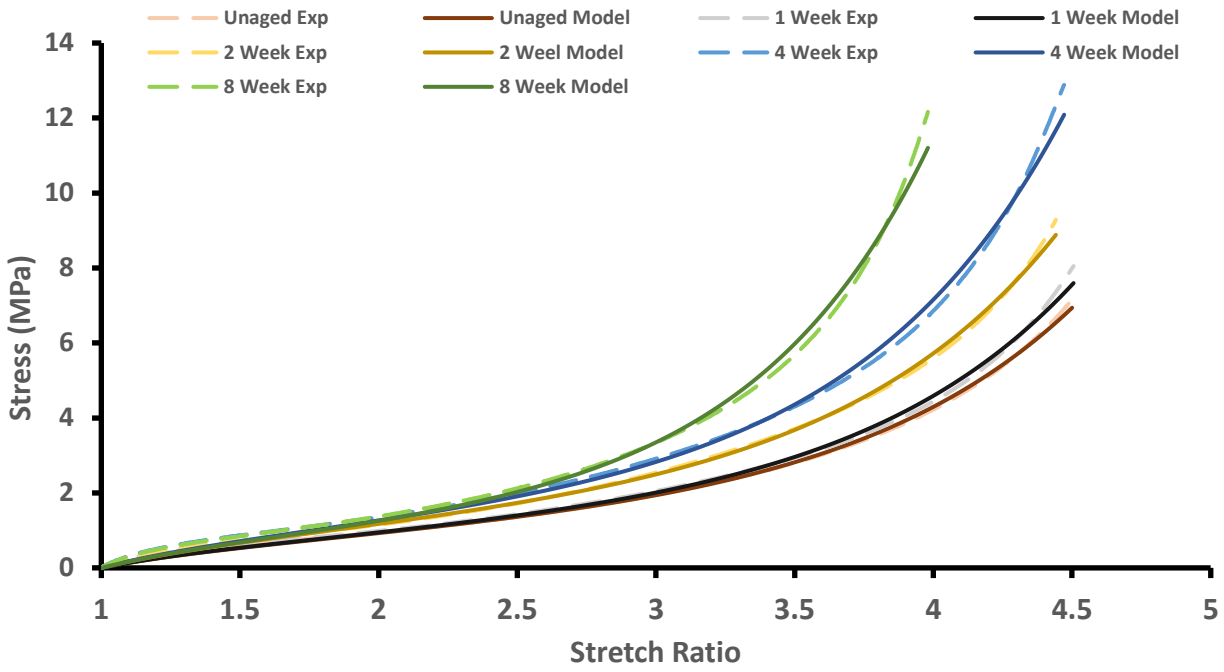

Fig. 3. 13: Arruda Boyce Material Model for 90 °C aged samples

It was observed that though the Ogden model had the best fit quality, as the number of fitting coefficients increased, it became difficult to maintain stability. This may be because only one (uniaxial) deformation mode was used, but the model needs at least three deformation modes. The Yeoh model was stable for most conditions, but the quality of fit was poor in some

situations. The Arruda-Boyce model, however, resulted in a stable model with high fitting accuracy, with only two fitting coefficients. Fig. 3. 13 shows the Arruda-Boyce material model along with the experimental data for 90 ℃ for all aging times. Hence, in this study, the Arruda-Boyce model is selected to be modified using the CDM approach to model the aging behavior as a function of aging time. The Arruda Boyce strain energy density (SED) equation is given by Eq. (3.7).

$$U = \mu \sum_{i=1}^{5} \frac{C_i}{\lambda_m^{2i-2}} \left(\bar{I}_1^i - 3^i\right) + \frac{1}{D}\left(\frac{J_{e\ell}^2 - 1}{2} - \ln J_{e\ell}\right) \tag{3.7}$$

where,

$$C_1 = \frac{1}{2}, C_2 = \frac{1}{20}, C_3 = \frac{11}{1050}, C_4 = \frac{19}{7000} \text{ and } C_5 = \frac{519}{673750}$$

μ is shear modulus, C_i (i= 1 to 5) is a constant, $\bar{I}_1$ is the first invariant, $D = 2/K$, K is the bulk modulus and $J_{e\ell}$ is the elastic volume strain.

3.4.2 Continuum Damage Mechanics (CDM) Model

The main objective of the CDM is to model the effects of distributed flaws such as cracks, voids, and their growth on a macroscopic scale. [71] Damage modeling of composites is very difficult given the complex filler interactions and diverse damage states. Hence, to simplify the model, a continuous damage variable ('*D*' in this study) is used which is based on the concept of effective stress and strain equivalence [72]. This theory assumes that the rather complex damage mechanics can be simplified by assuming that this damage is uniformly distributed and occurs in a distributed way [72]. For this study, the damage parameter *D* is defined to be 0 for unaged condition, which means that there is no damage. However, as aging occurs, *D* increases due to the degradation of material taking place due to the formation of cracks and voids and may go up to a maximum of *D* =1 which marks the total damage of the material.

The traditional CDM model is modified to make it a power-law relation by adding a constant 'k' in the exponent. The parameters that are modified with the CDM equation are the hyperelastic fitting constants: the initial shear modulus (μ) and locking shear (λ_m). The behavior of these constants needs to be understood for accurate modelling. As seen in the experimental data, μ

increases with aging time. λ_m represents the value at which the upturn nature of the curve starts. This value decreases as the stiffness increases at a more rapid pace.

Thus, the equations for the change in these coefficients can be Eq. (3.8)

$$\mu_j = \frac{\mu_0}{\left(1 - D_j\right)^{k_j}}$$
$$\lambda_{m,j} = \left(1 - D_j\right)^{k_j} \lambda_{m,0} \tag{3.8}$$

Where, μ_j and $\lambda_{m,j}$ is the shear modulus and locking shear for aged samples, respectively. Index j is the aging time in weeks (j= 1, 2, 4,8, etc.). Thus, using Eq. (3.7) and (3.8) the Arruda-Boyce model is modified as shown in Eq. (3.9).

$$U_j = \frac{\mu_0}{\left(1 - D_j\right)^{k_j}} \sum_{j=1}^{n} \sum_{i=1}^{5} \frac{C_i}{\left[\left(1 - D_j\right)^{k_j} \lambda_{m,0}\right]^{2i-2}} \left(\bar{I}_1^i - 3^i\right) + \frac{1}{D}\left(\frac{J_{el}^2 - 1}{2} - \ln J_{el}\right) \tag{3.9}$$

Thus, the data gathered for all aging time periods is curve fitted using Eq. (3.9) and the damage variable '*D*' and exponent '*k*' is found out.

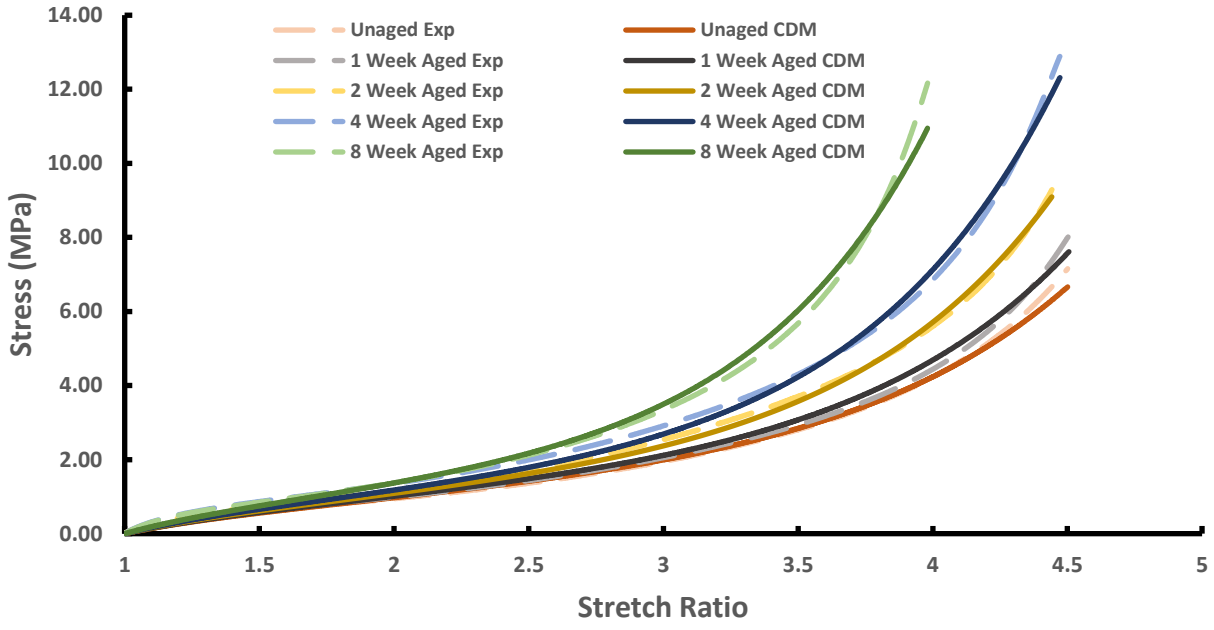

(A)

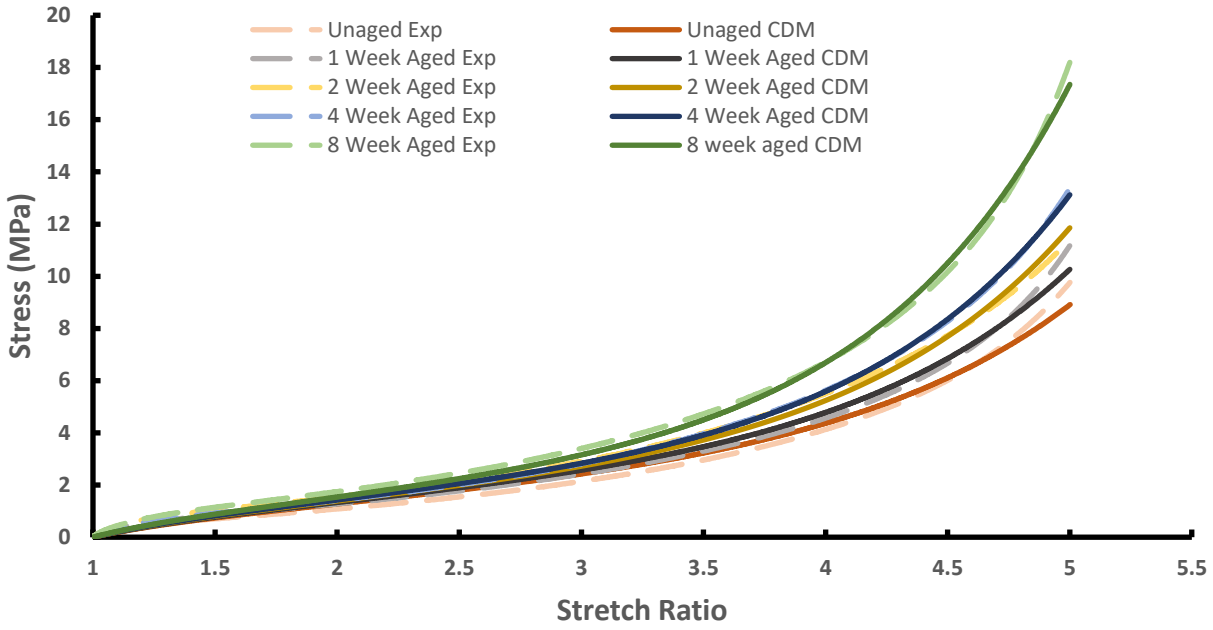

(B)

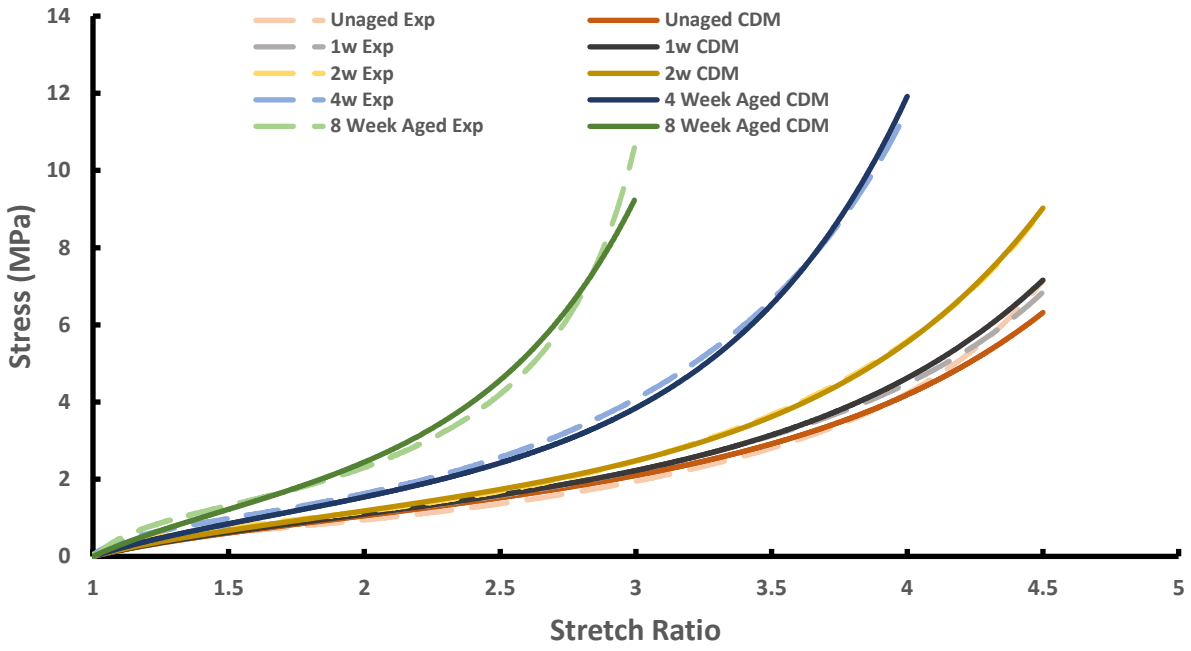

(C)

Fig. 3.14: Comparison of CDM and Experimental Stress-Strain Curves at (A) 90 ℃ (B) 70 ℃ (C) 110 ℃

From these, the Arruda-Boyce model coefficients for all aging conditions are found. Table 3.4 shows the summary of model coefficients found from the modified Arruda-Boyce equation. As expected, the initial shear modulus increases with aging time and the value of locking shear decreases. As seen in the above figures, the aging temperature plays a huge role in dictating the response of SBR. At lower temperatures as seen in Fig. 3.14 (B), we see that the curves are close together. However, with an increase in aging temperature, as seen in Fig. 3.14 (A) and (C), with increasing aging temperature, the curves grow farther apart. This suggests that damage in SBR is not linear w.r.t aging temperature.

Table 3.4: Material and Damage parameters for 90 °C aged samples

Aging Time *(weeks)*	μ	λ	D	k
0 (unaged)	0.472	2.656	-	-
1	0.480	2.607	0.019	1
2	0.508	2.467	0.071	1
4	0.534	2.344	0.118	1
8	0.586	2.138	0.195	1

Thus, in order to get the hyperelastic response of SBR at any given time and temperature, we need the unaged material parameters and the respective damage variable. Thus, a relationship between these damage variables and the aging time and temperature needs to be understood and modelled. Fig. 3.15 shows the damage parameters for all the tested aging times and temperatures.

As seen in the literature for various aging parameters (e.g., CLD) as well as from Fig. 3.15, the damage parameter follows an S-shape behavior. The rate of reactions/damage is slow at the start but increases steadily and then plateaus off. The Avrami or Sigmoid equation was chosen as the base equation to model the damage parameter. The typical form of the sigmoidal equation and the nature given by Eq. (3.10) and seen in Fig. 3.16.

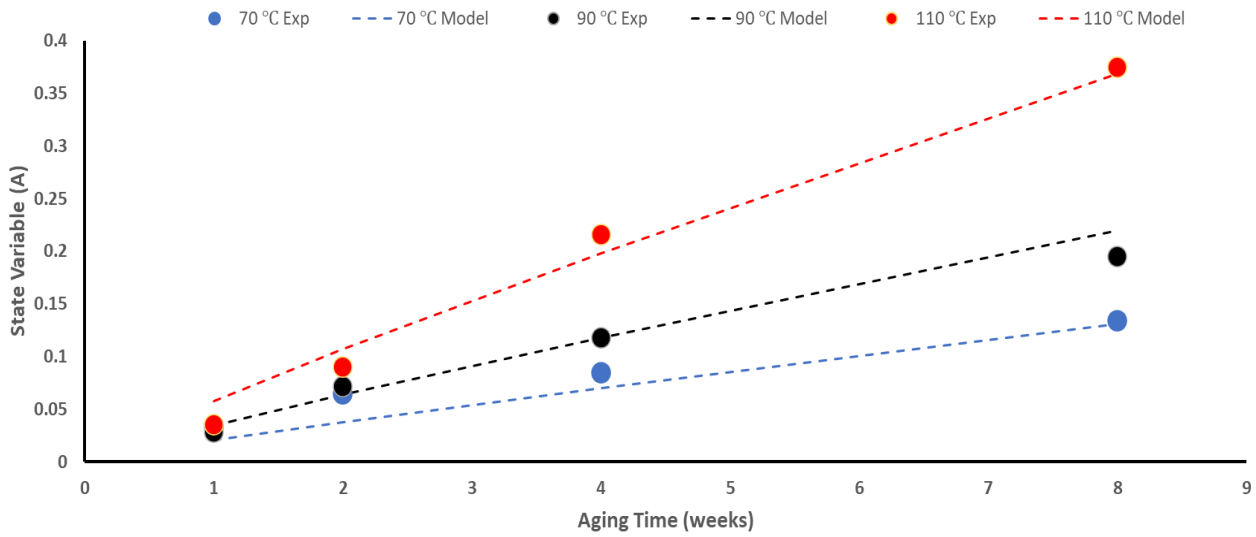

Fig. 3.15: Damage Parameter Plot for all Aging Time and Temperature

$$y_{fit} = X\,(1 - e^{-kt^n}) \tag{3.10}$$

However, it does not consider the non-linearity induced due to temperature effects. Thus, it is modified to get Eq. (3.11)

$$D = X\,e^{(A_1 - A_2 T_k)}\left(1 - e^{-C * e^{k\,T_k}\,t^n}\right) \tag{3.11}$$

Where, A_1, A_2, C, X, k, n are fitting constants and t is aging time in hours and T_k is aging temperature in Kelvin.

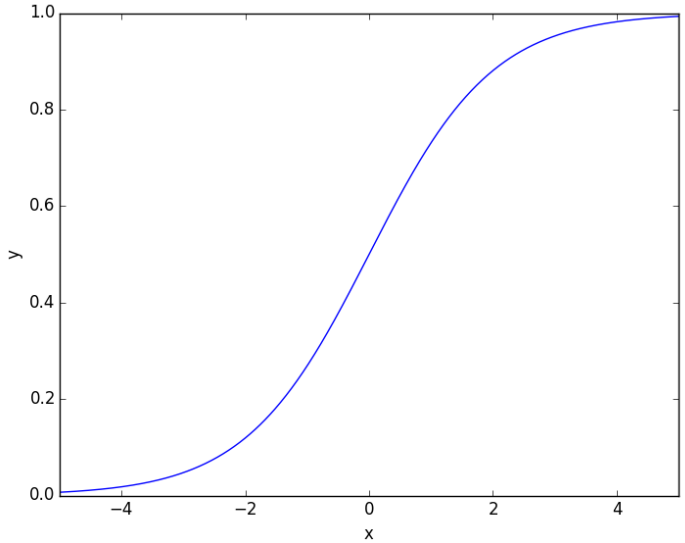

Fig. 3.16: S-shape curve based on Sigmoid equation

Now, the damage variables can be found at any given aging time and temperature using Eq. (3.11). Using these damage variables, the stress-strain curves at any aging time and temperature can be predicted for SBR.

3.5 RESPONSE PREDICTION AND CONFIRMATORY EXPERIMENTS

In order to check the validity of the model for any given aging time and temperature, confirmatory experiments were performed. The aging conditions data (aging time and temperature) was used to calculate the damage coefficient and then the unaged material parameters were modified accordingly. This gives us the stress-strain curve which was then compared to the experimental data as shown in Fig. 3.17.

(A)

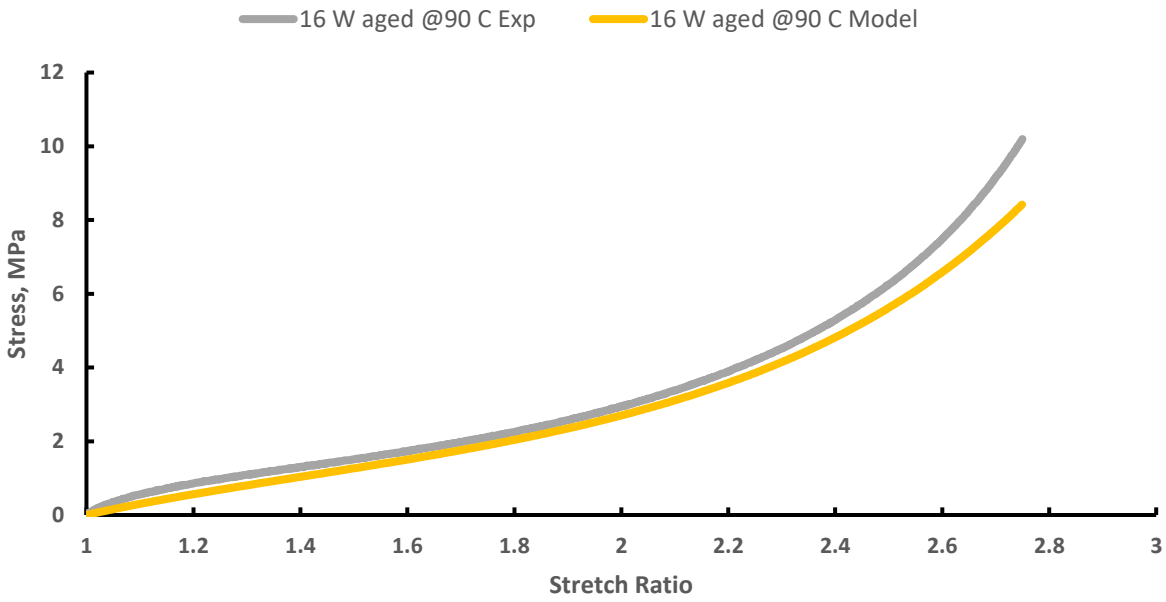
16 W aged @90 C Exp
16 W aged @90 C Model
Stress, MPa
Stretch Ratio
0
2
4
6
8
10
12
1
1.2
1.4
1.6
1.8
2
2.2
2.4
2.6
2.8
3

(B)

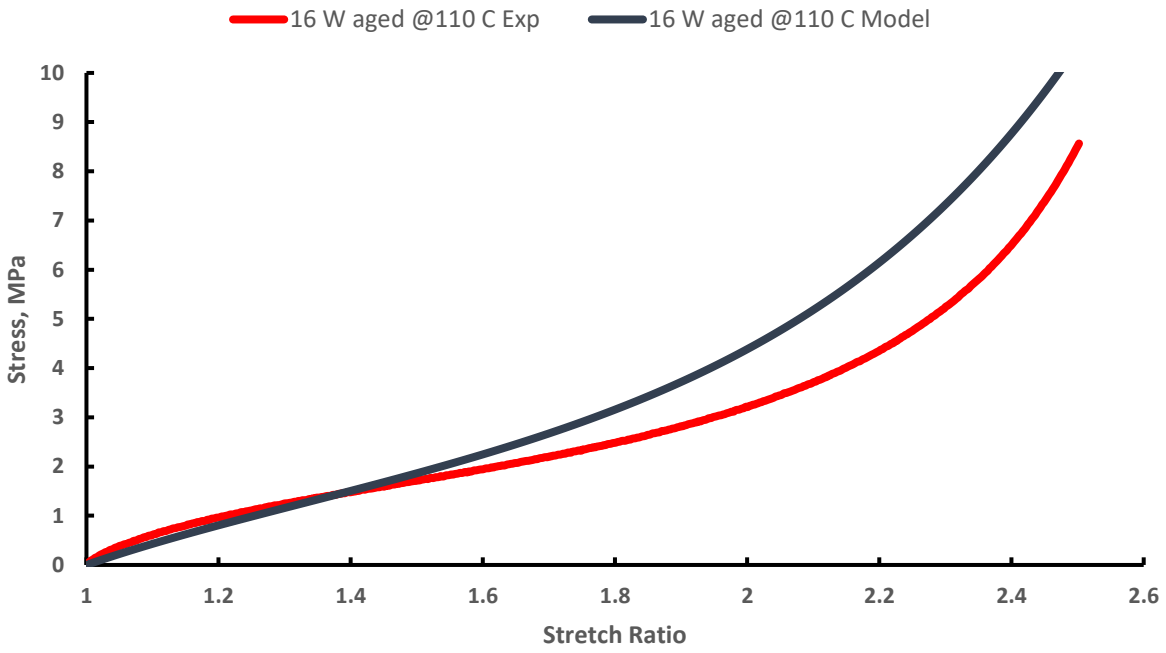
16 W aged @110 C Exp
16 W aged @110 C Model
Stress, MPa
Stretch Ratio
0
1
2
3
4
5
6
7
8
9
10
1
1.2
1.4
1.6
1.8
2
2.2
2.4
2.6

(C)

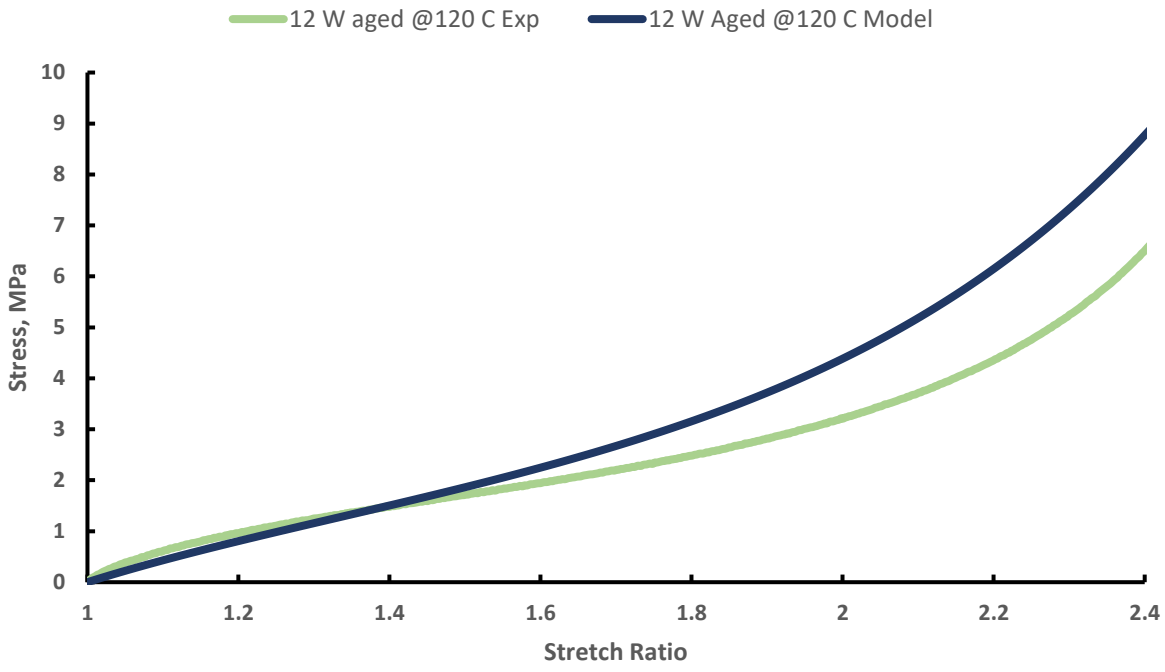

(D)

Fig. 3.17: Predictive Response comparison (A) 18-week aged at 60 ℃ (B) 16-week aged at 90 ℃ (C) 18- week aged at 110 ℃ (D) 12-week aged at 120 ℃

Uniaxial tests were again conducted on aged rubbers with different aging temperatures and higher aging times to understand the robustness of the damage model. The experimental data versus the model for respective aging conditions are shown in Fig. 3.17 (A), (B), (C), (D). The predictions are made, and the experiments are conducted till a stretch ratio of around 2.5 which is around 150% strain. This is a good estimate for the maximum strain the material will encounter in a real-life scenario for various applications.

In all the four cases, the model is able to predict the stress-stretch response quite accurately. However, as the strain increases, the model is observed to sometimes deviate away from the experimental data. However, this is only a concern for predicting the response at very high stretch ratios (> 5).

3.6 ABAQUS USER MATERIAL (UMAT) SUBROUTINE

3.6.1 Theoretical Background

In the previous sections, the Arruda-Boyce model was modified to predict the aged hyperelastic response. Based on this formulation framework, a user material subroutine (UMAT) can be defined for ABAQUS CAE software. This will help to observe the material response for various rubber geometries as well as applications. Commercial simulation software packages such as ABAQUS, ANSYS, SolidWorks, etc. have built-in constitutive equations to model hyperelastic behavior. Some software also have the capability to automatically curve fit the experimental data and give out the necessary fitting constants based on the model. Furthermore, the stability of the model for various deformation modes can then also be determined. However, most software packages are only limited to a handful of standard hyperelastic models such as Neo-Hookean, Mooney-Rivlin, Ogden, etc. Hence, for research purposes, where new material models are developed or existing models are modified, these built-in constitutive models can not be used. For this reason, ABAQUS provides users with the option of developing a user subroutine. In the case of hyperelastic models, we have three types:

1) UHYPER
2) UANISOHYPER
3) UMAT

UHYPER subroutine is used to define a custom hyperelastic model for isotropic materials. This is especially useful to model cases of incompressibility. The SED function needs to be defined as a function of strain invariants. **UANISOHYPER** is a subroutine used for anisotropic hyperelastic materials. Both UHYPER and UANISOHYPER can be used to model nonlinear viscoelastic materials based on the viscoelastic theory framework in ABAQUS. If the Mullins effect is to be considered in the model, the ABAQUS documentation [70] also provides information to include that feature in the subroutines. However, in this study, as the Mullins effect is eliminated while conducting the experiments, it will not be added to the FE model.

Moreover, ABAQUS does not allow combining the Mullins effect with the nonlinear viscoelasticity and both these should be used separately. Finally, the **UMAT** is a general-purpose subroutine that can be used to model any time of material behavior. Users can define their constitutive equations and hence this type of subroutine is used widely for research purposes. UMAT is especially useful over subroutines when modelling compressible solids which require the isochoric and volumetric responses to be decoupled. Thus, in the case of a UMAT subroutine, the user is not bound to a built-in constitutive law in ABAQUS. Another very important feature of UMAT is that state variables can be used to modify the equations which are paramount in this study. After each time increment, the stress and state variables are updated.

The most important and often complicated part of writing a UMAT subroutine is defining the material Jacobian matrix $\partial \triangle \boldsymbol{\sigma} / \partial \triangle \varepsilon$ for the model. Here, $\triangle \boldsymbol{\sigma}$ is a small increment in Cauchy stress and $\triangle \varepsilon$ is a small increment in strain. It is the equivalent of an elasticity tensor or stiffness matrix for elastic materials. It is basically the slope of the stress-strain curve obtained from the constitutive equation and is also called a tangent modulus. It gives us the mapping and relationship between stress and strain. The material Jacobian can be modelled numerically (approximately) or analytically, the latter being harder to do so. Approximate Jacobian matrices will lead to convergence issues. Thus, whenever possible, an analytical material Jacobian is always preferred.

3.6.2 Material Jacobian

Thus, after comparing various hyperelastic subroutines, the UMAT subroutine was chosen for this study. An analytical material Jacobian also was defined for the Arruda-Boyce model which is a first invariant based model. Moreover, the UMAT code developed can be used for any first invariant based hyperelastic model by changing the SED function accordingly.
Every UMAT subroutine has the following basic three requirements:

1) Material Parameters
2) Stress-Strain constitutive equations
3) Jacobian matrix

Material parameters refer to the constants or properties used in the SED function. In this case, for the Arruda-Boyce model, we have two material parameters: the initial shear modulus (μ) and the locking shear (λ_m). The Jacobian matrix can be defined by the Eq. (3.12)

$$C_{ijkl} = \frac{1}{J}\frac{\delta \tau_{ij}}{\delta D_{kl}} \tag{3.12}$$

Where, τ_{ij} is the Kirchoff stress, D_{kl} is the virtual rate of deformation and J is the determinant of the deformation gradient.

The components of the Jacobian matrix can be given by Eq. (3.13)

$$C_{ijkl} = \frac{2}{J}\left(\frac{\partial \bar{U}}{\partial \bar{I}_1}\right) * \left[\frac{1}{2} * \left(\delta_{ik}\bar{B}_{jl} + \delta_{jl}\bar{B}_{ik} + \delta_{il}\bar{B}_{jk} + \delta_{jk}\bar{B}_{il}\right) + \frac{2}{3}\left(\frac{1}{3}\bar{I}_1\delta_{ij}\delta_{kl} - \bar{B}_{ij}\delta_{kl} - \delta_{ij}\bar{B}_{kl}\right)\right]$$
$$+ \frac{2}{J}\left(\frac{\partial^2 \bar{U}}{\partial \bar{I}_1^2}\right) * \left[\bar{B}_{ij}\bar{B}_{kl} - \frac{1}{3}\bar{I}_1\left(\bar{B}_{ij}\delta_{kl} + \delta_{ij}\bar{B}_{kl}\right) + \frac{1}{9}\bar{I}_1^2\delta_{ij}\delta_{kl}\right] + \left(\frac{\partial \bar{U}}{\partial J} + J\frac{\partial^2 \bar{U}}{\partial J^2}\right)\delta_{ij}\delta_{kl} \tag{3.13}$$

Where, C_{ijkl} is the Jacobian tensor, $\bar{U}$ is the SED function, $\bar{I}_1$ is the first isochoric strain invariant of the Cauchy-green tensor, $\bar{B}$. Is the isochoric left C-G tensor and J is the determinant of the deformation gradient. In the Cartesian coordinate system, and for an isotopic martial, the stress can be represented by 6-dimensional vectors using Voigt notation. Thus, the Jacobian can also be defined by a 6x6 matrix as seen below.

$$\text{Jacobian Matrix } (C^{MJ}_{6X6}) = \begin{pmatrix} C_{1,1} & C_{1,2} & C_{1,3} & C_{1,4} & C_{1,5} & C_{1,6} \\ C_{2,1} & C_{2,2} & C_{2,3} & C_{2,4} & C_{2,5} & C_{2,6} \\ C_{3,1} & C_{3,2} & C_{3,3} & C_{3,4} & C_{3,5} & C_{3,6} \\ C_{4,1} & C_{4,2} & C_{4,3} & C_{4,4} & C_{4,5} & C_{4,6} \\ C_{5,1} & C_{5,2} & C_{5,3} & C_{5,4} & C_{5,5} & C_{5,6} \\ C_{6,1} & C_{6,2} & C_{6,3} & C_{6,4} & C_{6,5} & C_{6,6} \end{pmatrix}$$

The Jacobian matrix is symmetrical and hence only the upper triangular matrix elements need to be calculated. Using this formulated Jacobian, the stress can be updated in each simulation increment with an increase in strain.

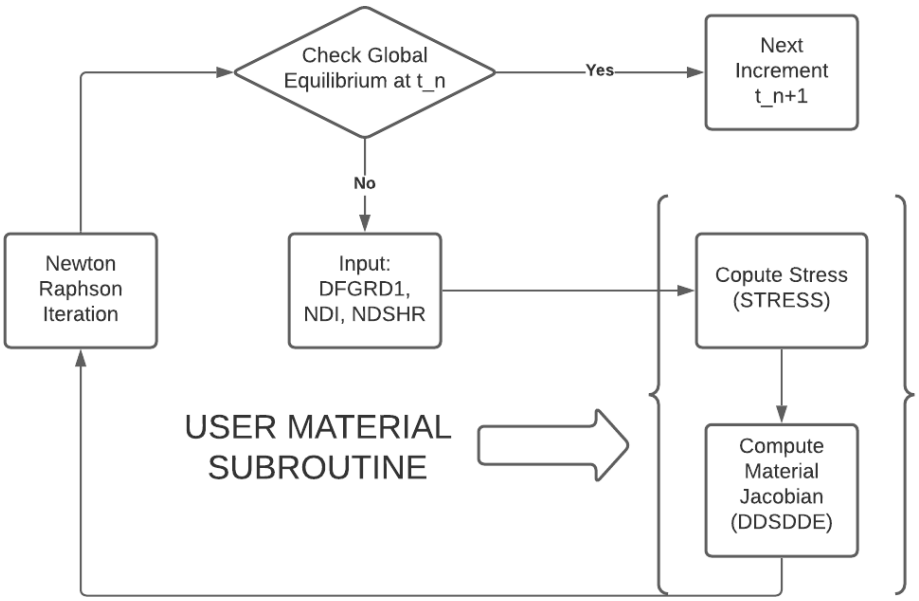

Fig. 3.18: Working of ABAQUS UMAT Subroutine

Here are some general steps used in the writing of the code. The inputs to the code are the deformation gradient (DFGRD) which is a 3x3 matrix, the direct stress components (NDI) and shear stress components (NSHR).

1) Define all the variables and their dimensions and parameters
2) Define the deformation (DFGR) and calculate the distortion tensors (DISTGR) using Jacobian determinant *J* (DET)
3) Calculate the left C-G tensor from the distortion gradient (BBAR)
4) Calculate the Cauchy stress matrix (STRESS)
5) Calculate the Jacobian matrix (DDSDDE)

3.6.3 Abaqus UMAT Simulation

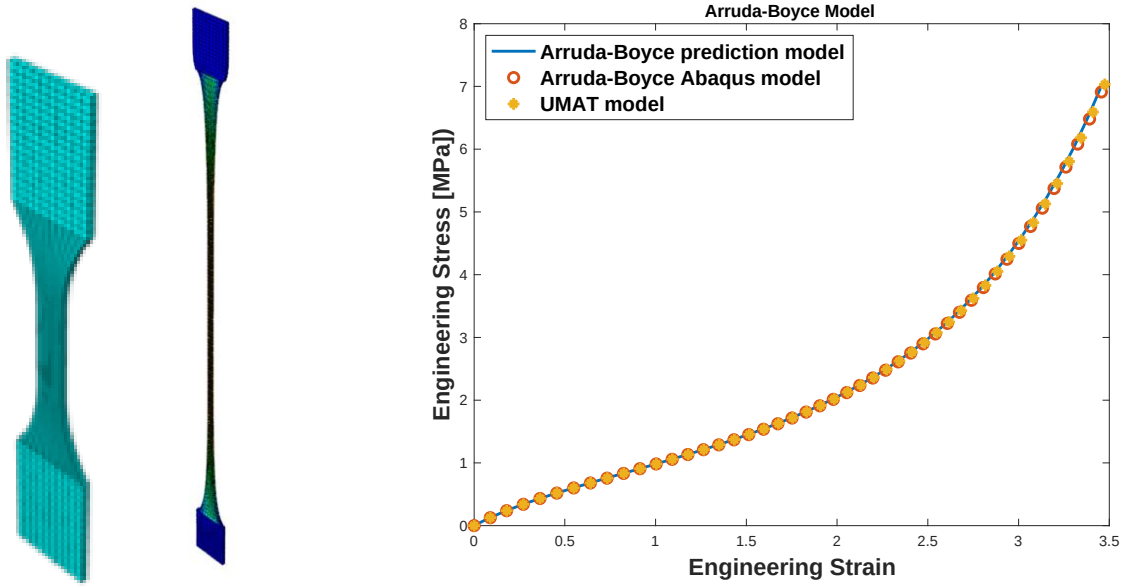

(A) (B)

Fig. 3.19: (A) Meshed Material Geometry Unloaded and under Simulated Uniaxial Tension (B) Comparison of UMAT with built-in ABAQUS model and Prediction Model

Material geometry as shown in Fig. 3.19 (A) is defined in ABAQUS with the same dimensions of the dogbone samples that were tested. Inbuilt Arruda-Boyce hyperelastic model was selected as the constitutive model and unaged material constants were inputted which were derived from experiments. Displacement boundary conditions were applied such that they matched the strain rate during the experiments. A comparison between the UMAT Subroutine response, the built-in Arruda Boyce model response and the mathematical model were all compared in Fig. 3.19 (B). As seen, there is very good agreement between these three models which validates the accuracy of the UMAT subroutine code.

The inputs needed for the UMAT subroutine are -the state variable (in this case the damage variable) and the strain input, as seen in Fig. 3.20. This example shown below is for the 90 C aged case with varying aging time periods. The state variable is modified using the aging evolution function, Fig. 3.20 (A) given by Eq. (3.11). The strain input may appear as an impulse when seen in Fig. 3.20 (B). However, this is due to the mismatch in time scales, wherein the

aging time is very long (in weeks) as compared to the time of testing (in seconds). A magnified view of the strain input is shown in Fig. 3.20 (C) which shows a ramp loading and unloading.

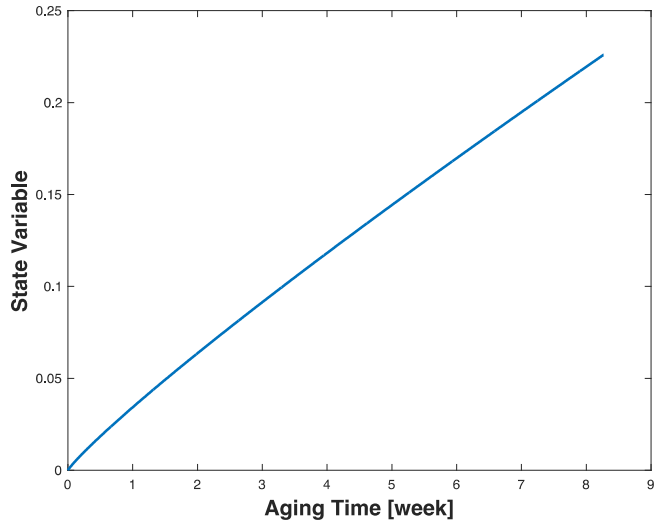

(A)

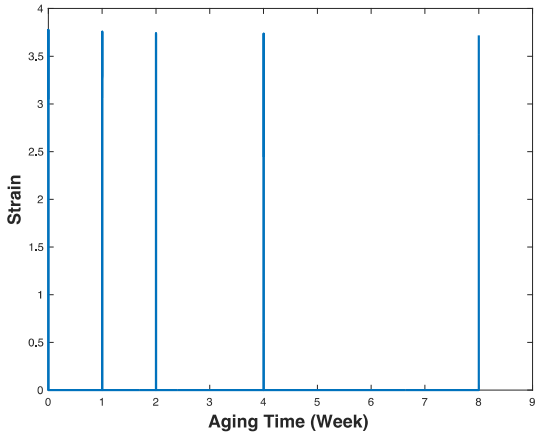

(B)

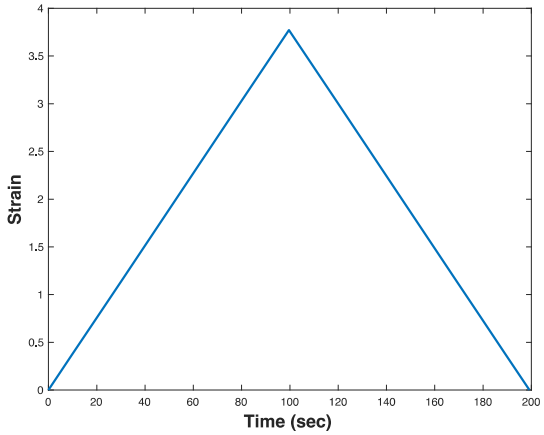

(C)

Fig. 3.20: Inputs for UMAT Simulation (A) State Variable (B) Strain profile for all Aging Scenarios (C) Magnified Strain Profile for each case

After defining the geometry and loading conditions, the meshing scheme and element type also need to be defined. The element type used in the model is C3D8H which is a linear hybrid 3 noded brick. This element type is especially used to model hyperelastic materials. It must be noted that this element can only model incompressible materials. Using the model, suitable input and boundary conditions, meshing scheme and element type we finally can get the required

outputs in the output field of ABAQUS. Fig. 3.21 shows the comparison between the aging evolution function response curves and the UMAT response curves. Both the models show an excellent correlation with one another, further validating the reliability of the UMAT subroutine.

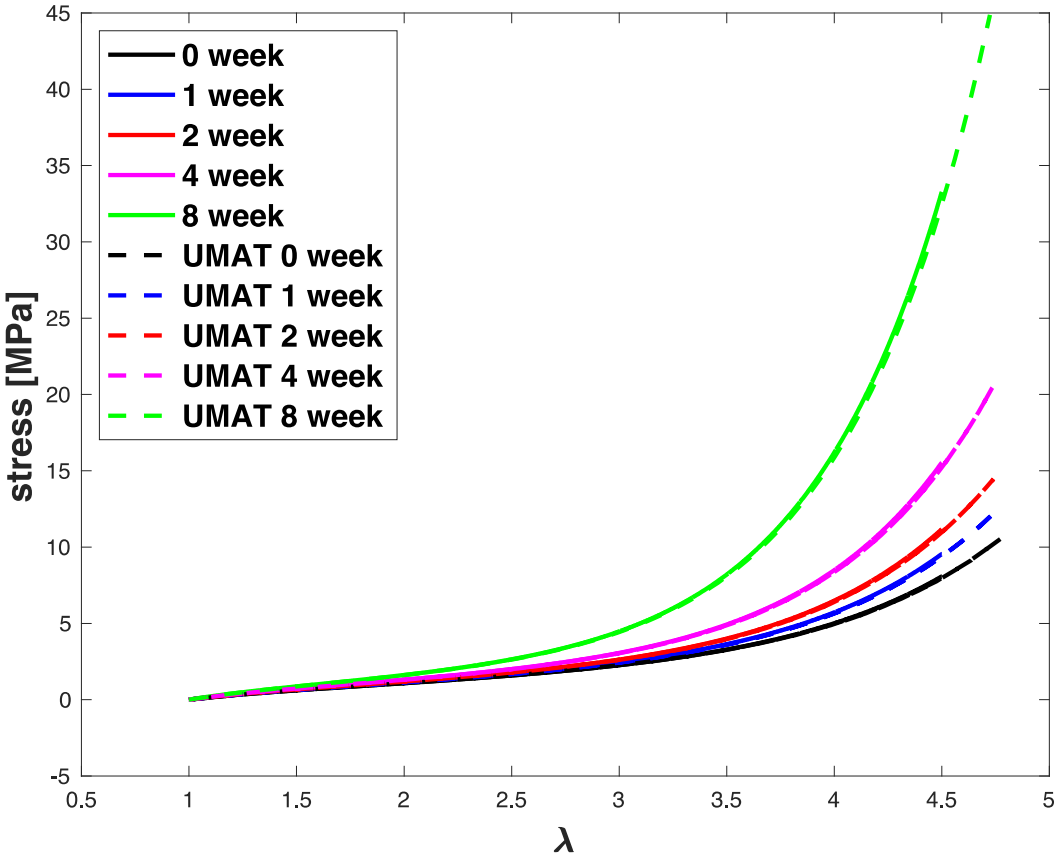

Fig. 3.21: Comparison between Prediction curves and UMAT Subroutine for 90 C aging response

4. STUDYING THE EFFECTS OF AGING ON THE VISCOELASTIC BEHAVIOR OF SBR

The previous chapter modelled the changes taking place in the hyperelastic response of SBR due to aging. This chapter will explore the effects of aging on viscoelastic properties. Dynamic Mechanical Analysis (DMA) experiments are conducted on the aged samples. In this study, only one aging temperature (70 ^{o}C) with varying aging time periods is used. This is because the focus of this study is to observe the mechanical changes and also discuss their effects on other properties such as friction coefficient, wear, etc.

4.1 THEORETICAL BACKGROUND

4.1.1 Viscoelasticity

The term 'viscoelasticity' can be broken down into- 'viscous' and 'elastic'. In simple terms, we can infer that viscoelastic materials have both fluid (viscous) and solid (elastic) properties. These properties become especially apparent during their deformation. Fluids resist shear forces, and their strain varies linearly with time when stress is applied. Also, they have no 'memory' of their configuration and remain deformed when stressed. On the flip side, solid elastic materials return to their original state after the removal of stress (they 'remember' their original configuration). Viscoelastic materials have both these characteristics and also exhibit time-dependent strain. A viscoelastic material also dissipates energy during a loading and unloading cycle. This is due to hysteresis and the amount of energy dissipated is the area of the load-unload loop as seen in Fig. 4.1. Another distinction between elastic and viscoelastic materials is that elasticity is due to the bond stretching along crystallographic planes, whereas, in the case of viscoelastic materials, it is due to the diffusion of atoms in amorphous materials [73].

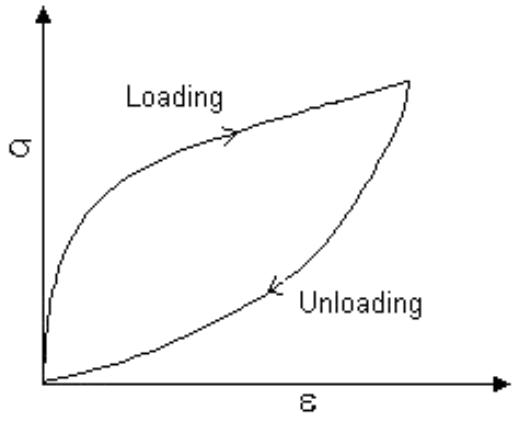

Fig. 4.1: Loading and Unloading curve and Hysteresis in Viscoelastic Materials

The time dependence of viscoelastic material deformation leads us to important loading mechanisms: creep and stress relaxation. In creep, the material is subjected to constant load whereas, in stress relaxation, the material undergoes fixed deformation with variable stress. Both these deformation mechanisms are used to study the viscoelastic properties. Relaxation experiments take less time to run as compared to creep processes. However, nowadays DMA has become increasingly popular to study these viscoelastic properties. DMA is an experimental analysis wherein stress or strain is applied cyclically. DMA experimentation is usually done to obtain modulus information. In a DMA experiment, a sinusoidal force given by Eq. **(4.1)** is applied to the sample and the strain response is then measured.

$$\sigma(t) = \sigma_o \sin(\omega t) \tag{4.1}$$

Where, σ is the maximum stress amplitude, t is the time and ω is the frequency of oscillation. Now, the strain output can be given by Eq.**(4.2)**

$$\epsilon(t) = \epsilon_o \sin(\omega t + \theta) \tag{4.2}$$

Using trigonometric manipulations, Eq. **(4.2)** can be divided into two parts, the in-phase elastic strain ϵ' and the out of phase viscous strain ϵ''.

$$\epsilon' = \epsilon_o \sin(\theta) \tag{4.3}$$

$$\epsilon'' = \epsilon_o \cos(\theta) \tag{4.4}$$

$$\epsilon^* = \epsilon' + \epsilon^{"} \tag{4.5}$$

This gives us two very important moduli for the material: the spring-like storage modulus and the viscous loss or imaginary modulus. The ratio of loss to storage modulus is called tan delta. These moduli are used to then characterize viscoelastic materials. Also, DMA can be used to compute the modulus values for each cycle and hence varying frequencies and temperatures can be used for measuring viscoelastic material behavior. Fig. 4.2 represents the sinusoidal stress input (red curve) given at a frequency of 10 Hz and the resulting strain output (green curve.) We see that the strain lags stress by a certain time dt. This lag is used to model viscous behavior. On the other hand, the slope of the stress-strain curves is related to its elastic behavior.

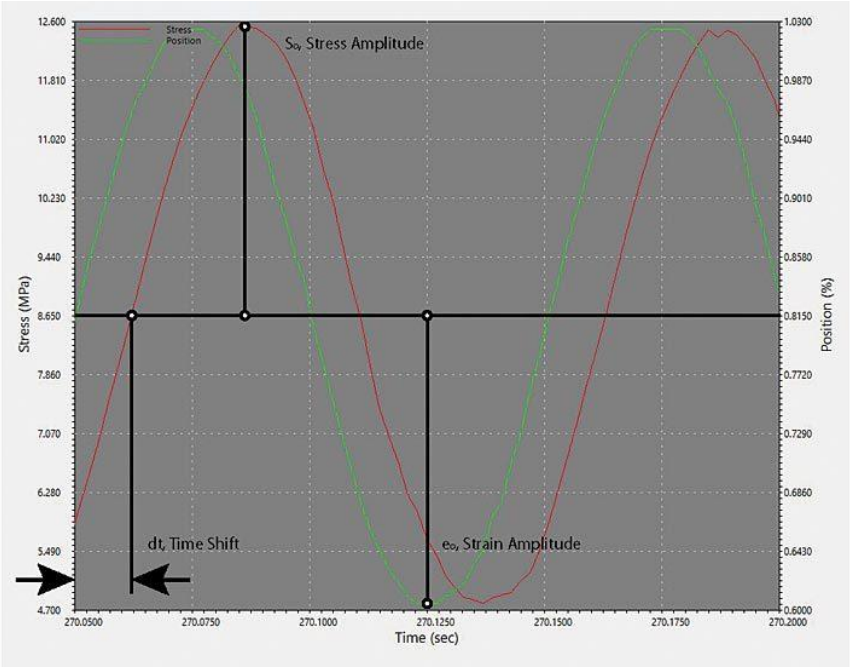

Fig. 4.2: Strain response to Sinusoidal stress input during DMA experiment [74]

4.1.2 Modelling Viscoelastic Behavior

As seen earlier, any viscoelastic material can be defined as a combination of viscous fluid and elastic solid. Thus, for modelling, we can represent a viscoelastic material with dashpots (viscous behavior) shown in Fig. 4.3 (A) and springs Fig. 4.3 (B) (elastic behavior). Their constitutive equations are given by Eq. **(4.6)** and Eq. **(4.7)**

$$\sigma = \eta \frac{d\gamma}{dt} \tag{4.6}$$

$$\sigma = G\,\gamma \tag{4.7}$$

Where, η is viscosity and G is the shear modulus. Now, to represent viscoelasticity, these springs and dashpots can be combined and used in series or parallel to form networks. These models can be used to model viscoelastic behavior. One such model simple model which is used widely is the Maxwell model. In this model, the applied stress is the same for each element and the total strain is the addition of the dashpot and spring deformation. This Maxwell model can be used to represent the rheological behavior in a DMA experiment. Fig. 4.4 shows the Maxwell ladder model which is a network of individual Maxwell models connected in parallel.

Fig. 4.3: (A) Dashpot Model (B) Spring Model

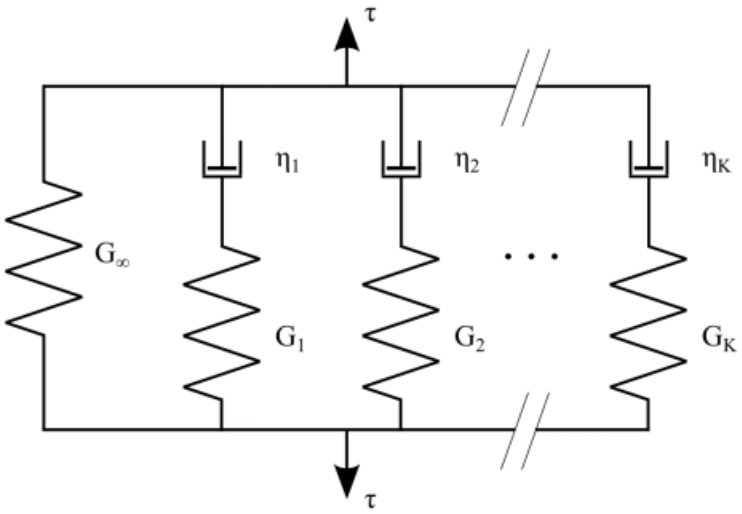

Fig. 4.4: Generalized Maxwell Ladder model

Eq. **(4.8)** Eq. **(4.9)** represent the model of rubber, where G' is storage shear modulus, G'' is loss modulus, ω is the frequency, τ_i is the relaxation time, and g_i is the relaxation modulus. Together, the relaxation time and modulus are termed as 'Prony Series' coefficients. τ_i is the time taken by the polymer to go from its deformed state to its original undeformed state. G_i is the imaginary spring stiffness that makes up the material. These coefficients make up the structure of the Maxwell model with springs and dashpots. For model and thermodynamic stability, these coefficients need to be positive. These Prony parameters have to be found by simultaneously curve-fitting the storage and loss modulus curves to Eq. **(4.8)** and Eq. **(4.9)** respectively.

$$G'(\omega) = G_0\left[1 - \sum_{i=1}^{N} g_i\right] + G_0 \sum_{i=1}^{N} \frac{g_i \tau_i^2 \omega^2}{1 + \tau_i^2 \omega^2} \tag{4.8}$$

$$G''(\omega) = G_0 \sum_{i=1}^{N} \frac{g_i \tau_i \omega}{1 + \tau_i^2 \omega^2} \tag{4.9}$$

4.1.3 TIME-TEMPERATURE SUPERPOSITION PRINCIPLE (TTSP)

TTSP is a widely used approximation in the polymer field. It is used to relate time and temperature in the case of linear viscoelastic materials (LVMs). It is generally observed that the elastic modulus of polymers increases with loading rate but decreases with increasing temperature. Moreover, these moduli curves do not change shape as the temperature is increased, but only shift horizontally. Thus, we can infer that a master curve can be formed by shifting these moduli curves at various temperatures. The master curve can be divided into three distinct regions. The first is the 'glassy region' which corresponds to short time (high frequency) or low temperature wherein rubber behaves more like a solid and has a very high modulus. Next, as the temperature is increased above the glass transition temperature, the modulus drops rapidly indicating the change from glassy state and onset of rubbery state. Lastly, we observe a plateau region termed as the rubbery plateau. If the temperature is increased beyond this point, we again observe a rapid modulus decrease indicating that the rubber has become almost viscous and flows like a fluid.

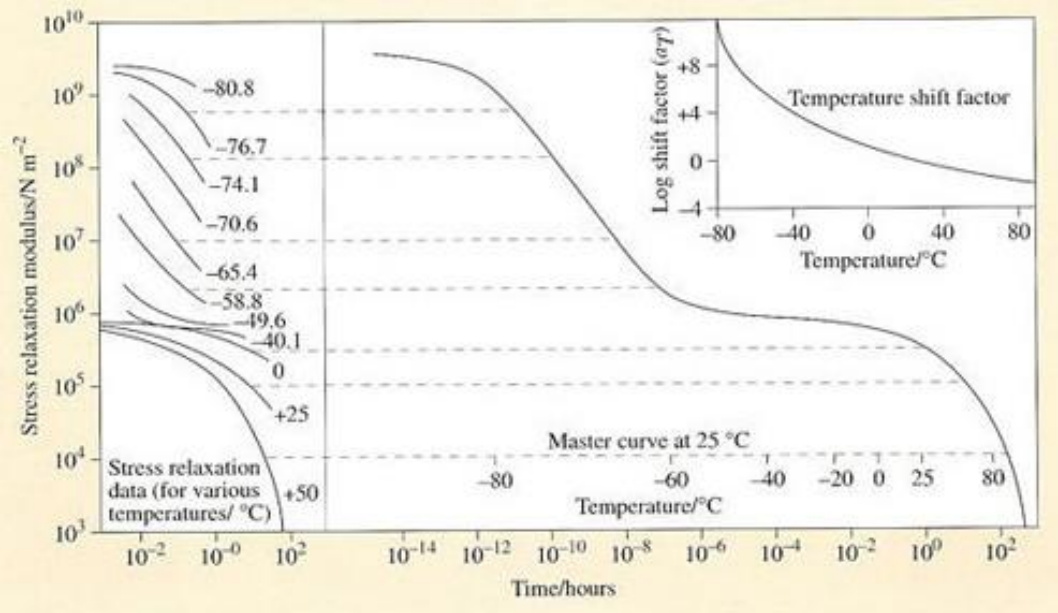

Fig. 4.5: Formation of a master curve from stress relaxation curves obtained at various temperatures and their corresponding shift factor plot [75]

The amount of shift for each curve is noted. Then a plot is formed which shows the change in shift factors w.r.t time, which is called a shift factor plot. Fig. 4.5 depicts the entire TTSP process. The left figure shows the stress relaxation curves obtained from experimentation at various temperatures. The figure in the center shows the master curve formed by shifting of these individual curves at a reference temperature of 25 ^{o}C that spans many decades. Finally, the figure at the top right shows the log shift factor plot w.r.t temperature. The shift factor is computed using a relationship given by Malcolm L. Williams, Robert F. Landel and John D. Ferry (also called the Williams-Landel-Ferry or WLF model) [16]. Another model used widely is the Arrhenius model.

The WLF equation corresponding to the model is shown in Eq. (4.10)

$$\log(a_T) = \frac{-C_1(T - T_{\text{ref}})}{C_2 + (T - T_{\text{ref}})} \tag{4.10}$$

For $T_g < T < T_g + 100$ °C

Where C_1 and C_2 are the WLF constants. C_1 and C_2 have universal values when the reference temperature is selected as the glass transition temperature. The two constants universal values for many high diene rubbers are C_1= 17.4 and C_2= 51.6 [76]. The shift factor, a_T, is defined as the

ratio between the time for a process to reach any given temperature and the time for the same process to reach the reference temperature. So, if the shift temperature is greater than the reference temperature, then this ratio will be > 1.

4.2 EXPERIMENTAL SETUP

4.2.1 Dynamic Mechanical Analysis (DMA)

DMA was used to study the effects of aging on the viscoelastic behavior of SBR samples. The sample thickness used was around 2 mm to ensure plane stress conditions while performing the experiments and for uniform aging. Experiments were performed in constant strain conditions in plane shear mode. The DMA machine used in this study is the Q800 by TA Instruments shown in Fig. 4.6. The size of the samples was 16 mm x 0.75 mm and around 2 mm thick. The experiments were conducted with a frequency sweep from 0.5 to 30 Hz, the constant strain of 0.04%, and a temperature range of -60 to 80^{o}C in increments of 5 degrees. A preload force of 0.001 N was also applied.

(A) **(B)**

Fig. 4.6: (A) Dynamic Mechanical Analysis Machine TA Instruments Q800 (B) DMA Film Tension Clamp

4.2.2 Aging Chamber

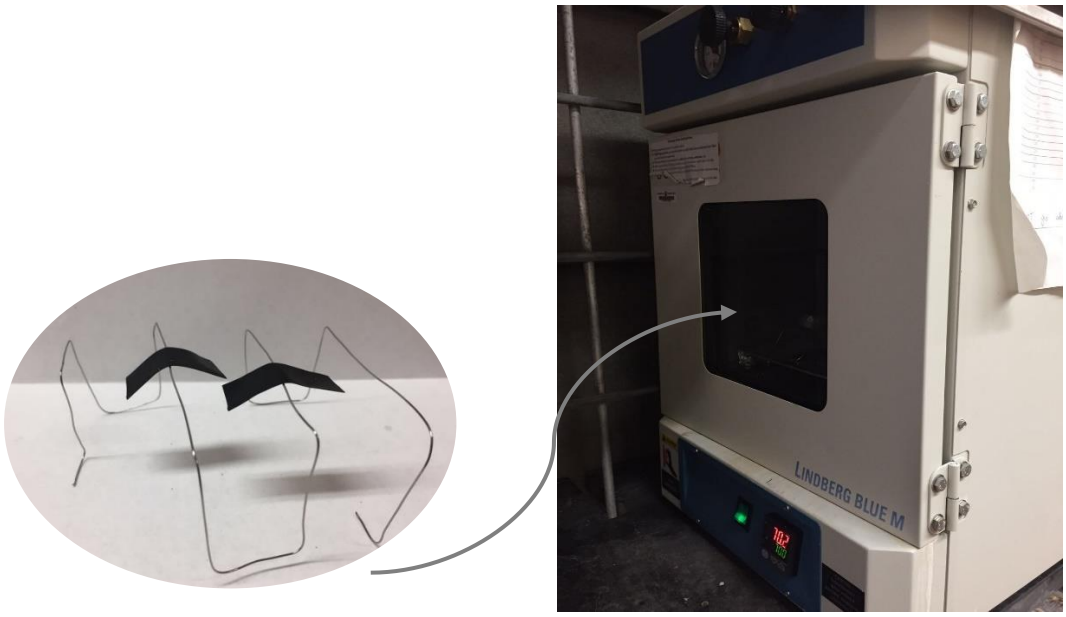

Fig. 4.7: Lindberg/Blue M™ Oven with Samples suspended on Wireframe

The aging process was similar to the one seen in the hyperelastic study. Accelerated aging was performed in the Lindberg/Blue M™ oven shown in Fig. 4.7 which has a capacity of 45L. Samples were suspended on a wire mesh without touching each other or the sides of the aging chamber. This ensured even aging of the samples and no anaerobic oxidation.

4.3 Analysis and Results

The individual moduli curves (storage and loss modulus) obtained from the DMA experiments for various temperatures for a fixed frequency range are shown in Fig. 4.8. The reference temperature was chosen to be 20 °C. The other curves were shifted horizontally w.r.t the reference temperature. The final storage and loss modulus master curves for the unaged condition can be seen in Fig. 4.9 (A). Also, the shift factor plot can be seen in Fig. 4.9 (B). The shift factors are curves fitted to Eq. (4.10) and the WLF constants are determined. The values of constants C_1 and C_2, were investigated to be around 7.3 and 109.8, respectively. This entire process was then repeated for other aging conditions as well. The storage and loss modulus curves for unaged, 2, 4, and 8 weeks aged are shown in Fig.
Fig. 4.10 (A) and

Fig. 4.10 (B) respectively.

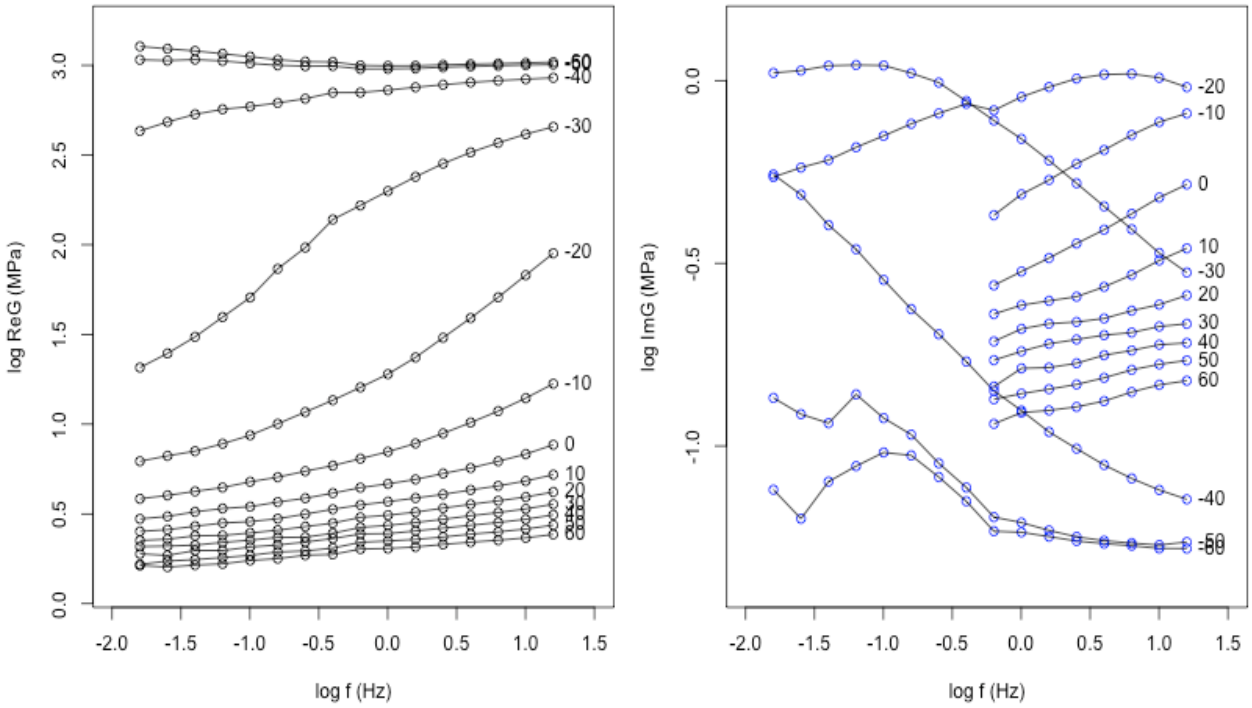

(A) **(B)**

Fig. 4.8: DMA Raw data (A) Storage Modulus curves (B) Loss Modulus curves

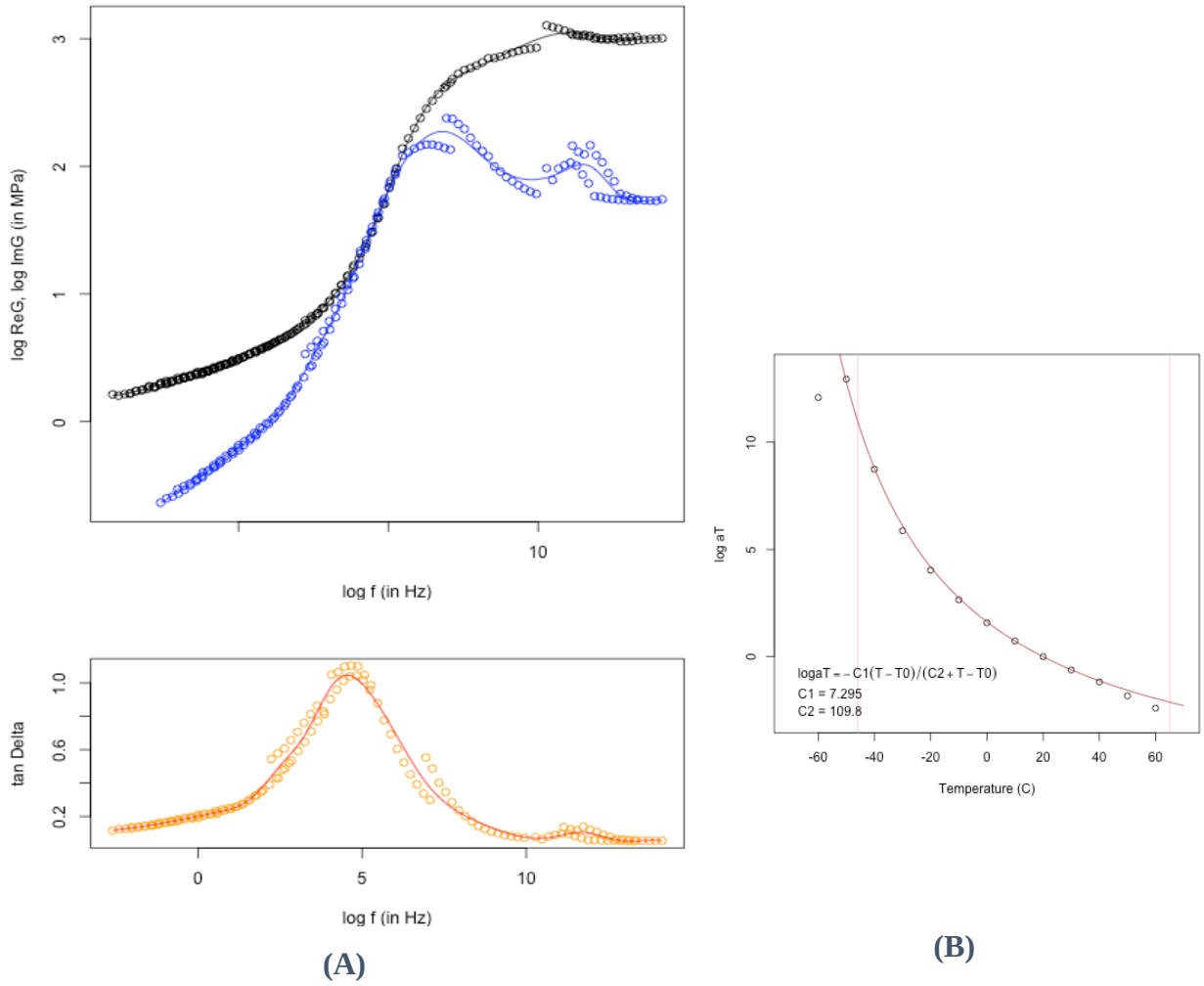

Fig. 4.9: (A) Master Curves for Unaged sample (B) WLF Shift factor plot

An immediate observation in the case of both storage and loss modulus is that of the increase in modulus or stiffness as aging time is increased. This gradual increase in modulus can be attributed to the increase in crosslink density of SBR due to aging. The oxidative reactions increased the chain polarity and crystallinity. The chain scission reactions that occur simultaneously with the crosslinking, increased the energy dissipation ability of rubber which resulted in a higher loss modulus.

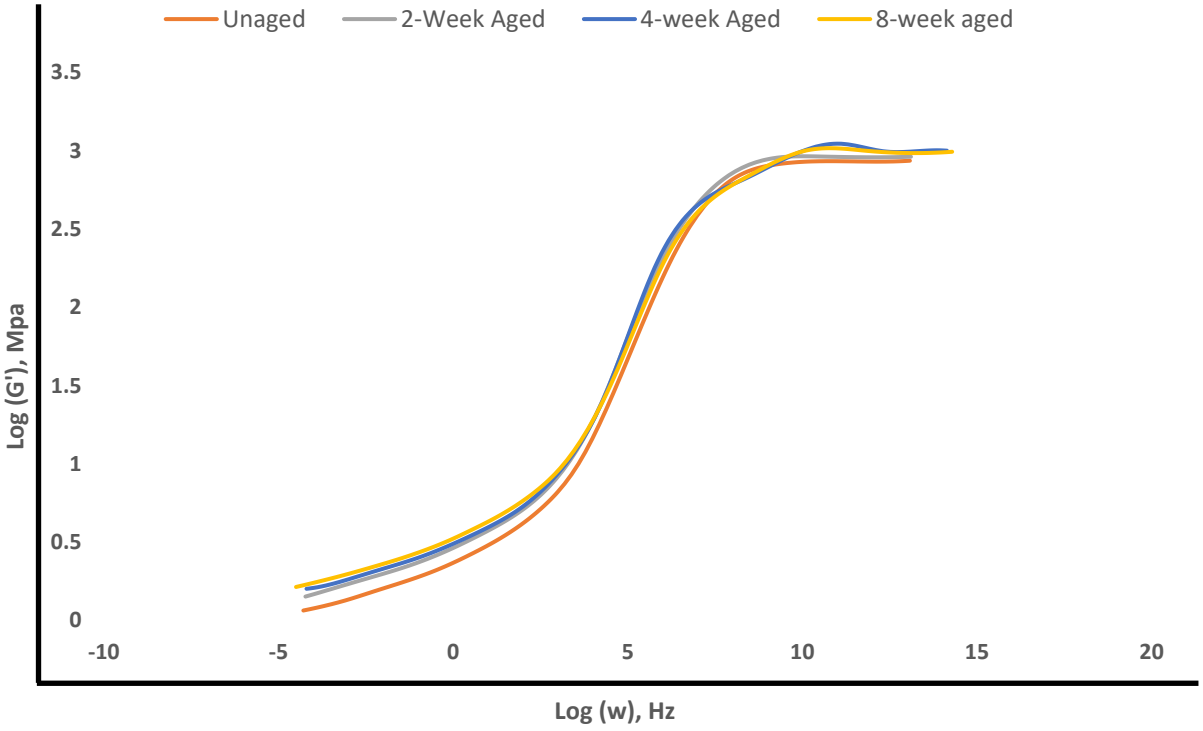
Unaged
2-Week Aged
4-week Aged
8-week aged
3.5
3
2.5
2
1.5
1
0.5
0
-10
-5
0
5
10
15
20
Log (G'), Mpa
Log (w), Hz

(A)

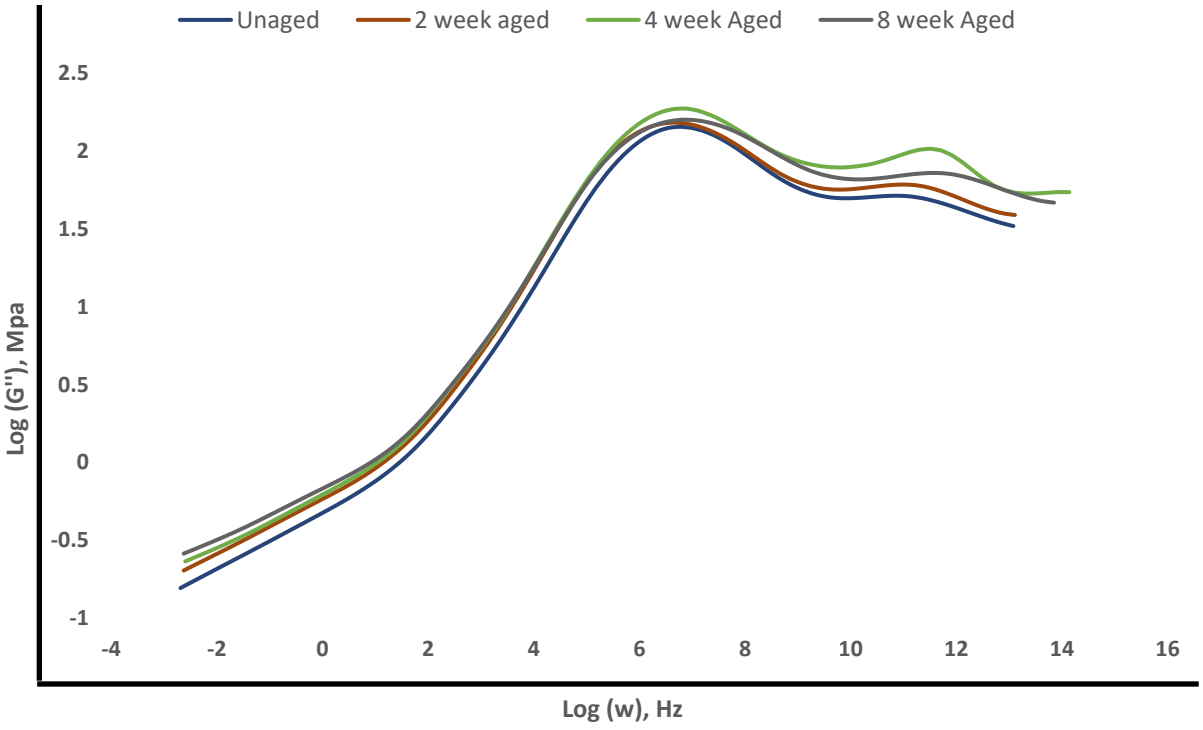
Unaged
2 week aged
4 week Aged
8 week Aged
2.5
2
1.5
1
0.5
0
-0.5
-1
-4
-2
0
2
4
6
8
10
12
14
16
Log (G''), Mpa
Log (w), Hz

(B)

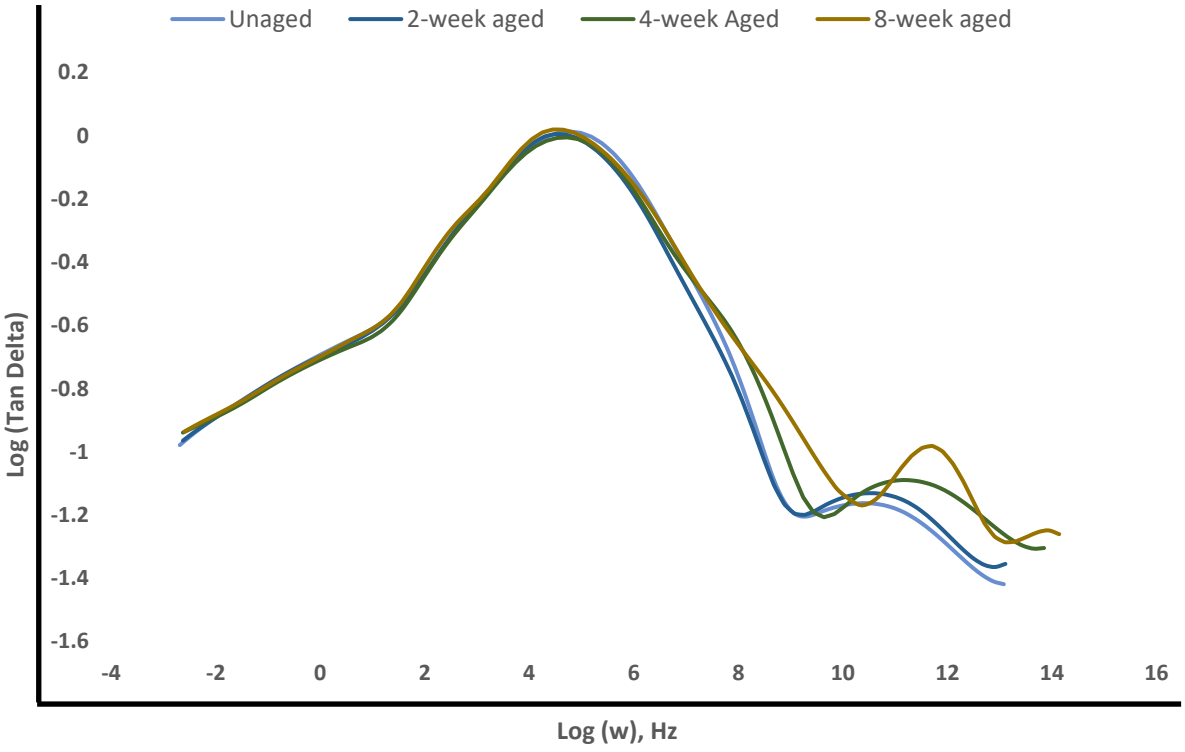

(C)

Fig. 4.10: Master Curves at various Aging conditions (A) Storage Modulus (B) Loss Modulus (C) Tangent Delta

We also observe a small shift to the left in case of the peaks of the tangent delta which indicates an increase in the glass transition temperature. This again is due to the continuous formation of crosslinks. Another observation made was that both storage and loss curves increased nonlinearly with aging time. The different aging temperature curves are cross each other in the transition region but are distinctively spaced apart in the glassy region.

Table 4.1: Equilibrium Modulus comparison for various Aging Conditions

	Unaged	One week aged	Two weeks aged	Eight weeks aged
G_∞ (MPa)	1.159	1.424	1.596	1.639

Table 4.1 and Fig. 4.11 show the increase in the equilibrium modulus as a function of aging time. It is seen that the change in modulus also follows an S-shape curve and eventually plateaus with higher aging time.

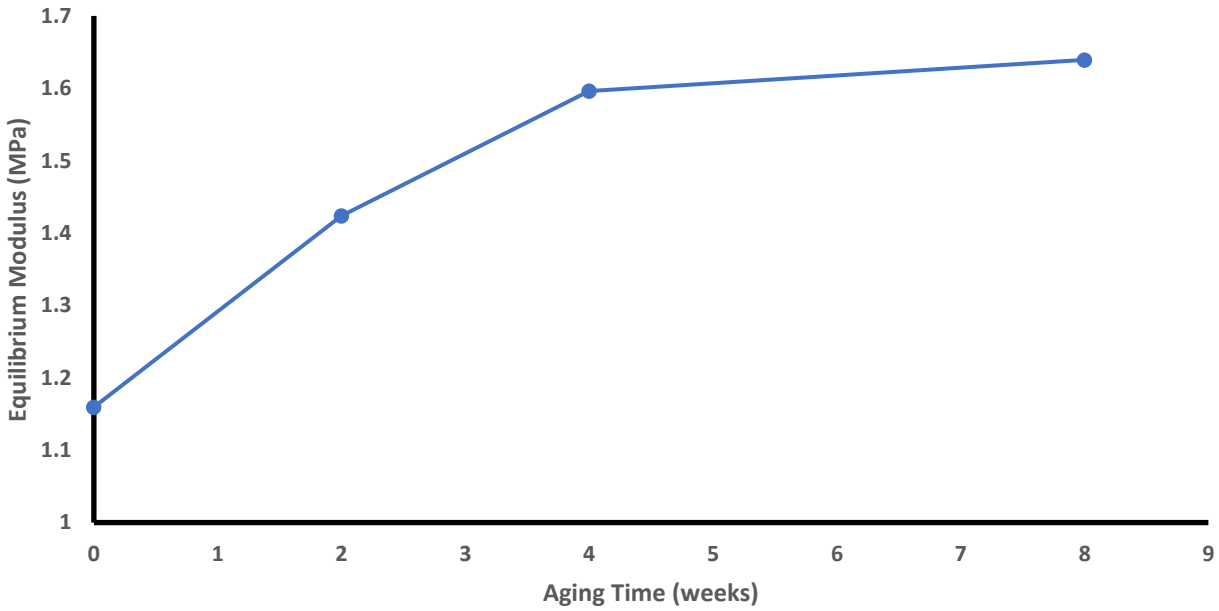

Fig. 4.11: Change of Equilibrium Modulus with aging period

4.4 CROSSLINK DENSITY

The number of crosslinks in a polymer is a very important factor that has a direct influence on the viscoelasticity of the material. This crosslinking can be quantitatively calculated using rheological and DMA experiments. As seen in the previous sections, the DMA master curves have three regions, one of which is the rubbery plateau region. The modulus in the rubbery plateau can be used to quantitatively calculate the SBR crosslink density (CLD). Thus, for various aging conditions, the molecular weight between crosslinks can be calculated by Eq. (4.11)

$$M_C = \frac{RTd}{G'_{\text{rubbery}}} \tag{4.11}$$

Where, M_C is the molecular weight between crosslinks, R is the universal gas constant, T is the temperature in kelvin and d is the density of the polymer. Now the CLD can be calculated by Eq. (4.12)

$$v_e = \frac{M_w}{M_c} \tag{4.12}$$

Where, v_e is the CLD and M_w is the molecular weight of the monomer. However, the relationship can be simplified as given in Eq. (4.13)

$$G'_{rubbery} \cong dRT/M_c = v_e RT \tag{4.13}$$

Thus, the CLD can be calculated from the universal gas constant, absolute temperature, and modulus in the rubbery plateau. Using Eq. (4.13), the CLD change of SBR with increased aging period was calculated and plotted in Fig. 4.12.

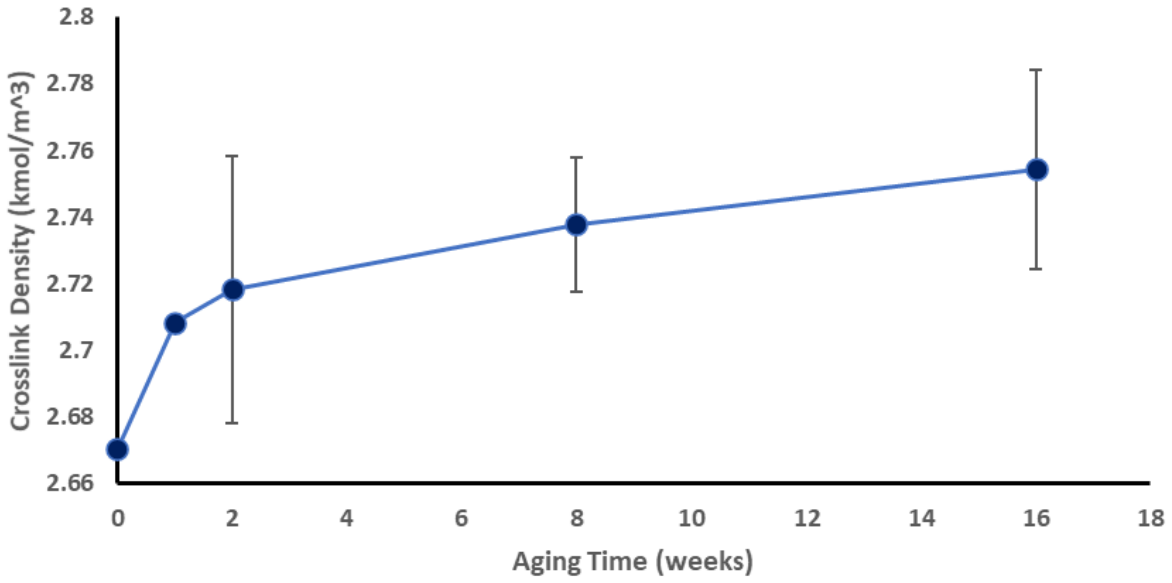

Fig. 4.12: CLD change with Aging Time for 70 °C

The CLD also follows an S-shape trend, similar to the one observed in the equilibrium modulus change due to aging as well. Moreover, this also confirms the fact that the change in the mechanical properties (both hyperelastic as well as viscoelastic) is due to the additional cross-links being formed which are in turn due to the oxidation, oxidative crosslinking and thermal crosslinking reactions occurring due to aging. This trend of change in CLD due to aging is also observed in the literature [40], [41], [54], [77].

5 STUDYING THE EFFECTS OF AGING ON THE TRIBOLOGICAL PROPERTIES OF SBR

As seen in the previous sections, rubber is used widely in many industries for varied applications. In some cases, it may have to undergo thousands of cycles in contact with other materials. This will lead to abrasion of rubber due to friction and the component will eventually wear out. The best example of such an application is vehicle tires. Tires typically undergo around 300,000-400,000 cycles in their useful lifetime. They are easily one of the most abused and the most important parts of a vehicle. Tire wear is influenced by multiple parameters as discussed earlier. The correlation of tire wear with these parameters such as road surface, environmental conditions, material composition, etc. has been studied by many researchers in lubricated conditions. However, the effect of aging, especially thermo-oxidative aging on the tribological properties of rubber in dry conditions has not been studied extensively. This chapter will investigate the correlation between rubber aging and its wear properties.

Tire wear can be defined as the loss of tread material as the tire rolls over the road surface due to tire-road interactive forces. Tire wear is heavily dependent on the vehicle as well as the driver input (braking, throttle, cornering, etc.) as well as surface and environmental conditions. Hence it is very difficult to predict tire wear numerically. As a result, lab and road tests are conducted extensively by changing the parameter under study to observe the change in tribological response of the tread. Aging of tires is quite common in southern states like Arizona and Texas where the increased temperatures accelerate the aging process. In 2008 NHTSA carried out research to study tire aging and better understand the service life and degradation of tires. It also aimed to develop a laboratory-based accelerated aging test to observe the decrease in peel force in belt and skim region of aged tires compared to new tires.

In the field, the treads are exposed to various complex forces and moments, and they are subjected to sliding and impact forces over hard- and sharp-edged materials. Generally, treadwear takes place due to the presence of impurities and imperfections on the surface of the tread. These imperfections may be voids in the tread compound or surface cracks. As the tread rolls and slides through the contact patch, stress concentrations are formed in these areas and

lead to the removal of material thus causing fatigue wear. Moreover, this constant sliding and rolling may increase the temperature of the tread surface, and this coupled with an increased environmental temperature may cause higher degradation. At a lower temperature, oxidation diffusion dominates over oxidation reaction with rubber and at higher temperatures, the rate of oxidation is much higher than diffusion [78]. This causes a layer of the hard and brittle surface to be formed, the depth of which depends on the temperature, oxygen concentration and time of exposure. This also causes the stress and strain at the break of the polymer to reduce significantly as seen from the hyperelastic tests. An increase or decrease in modulus is also seen as the material is aged. In the case of SBR, the material stiffens due to aging. Moreover, the surface of the rubber develops micro-cracks which further accelerates the wear rate due to faster crack growth. Simultaneously, bonds are continuously formed (cross-linking and oxidation bonds) and broken (chain scission). Depending on the exact composition and conditions, one reaction dominates over the other and hence material modulus increases or decreases accordingly.

Kratina et al [78] have researched about the influence of thermal aging on the steady-state and dynamic wear behavior of NR/SBR vulcanizates. A Chip and Cut tester were used to determine the abrasion resistance. Four different NR/SBR blends were studied. They concluded that thermal aging does influence the abrasion process. A linear decrease of rubber resistance with an increase in aging time is found out. Ulf Sandberg (VTI) studied the effects of tire aging on its noise emission and rolling resistance. They found a strong positive correlation between the aging time and the hardness of rubber. This is mainly due to the oxygen in the atmosphere reacting with the tread surface. Moreover, due to this increased hardness, there is also an increase in the noise emitted and thus, unnecessary noise can be eliminated by limiting tire age.

As seen, limited studies exist which investigate the influence of thermal aging on the wear characteristics of SBR compounds. The goals of this research study are :

1) Conduct experiments to determine the wear loss of SBR for different aging temperatures and periods
2) Study influence of aging on the friction coefficient of SBR
3) Calculate the frictional energy (FE) and observe changes due to aging
4) Correlate the viscoelastic properties (tan delta) with wear results for aged samples

5.1 THEORETICAL BACKGROUND

As seen in the previous sections, many elastomer wear models exist. However, Archard's model is used widely in many studies due to its simplicity. It is generally used to model adhesive types of wear. The law states that the volume loss due to wearing (V) is directly proportional to the normal load (F_n) acting on it and the distance it has covered (s) and is inversely proportional to the hardness (H) of the softer material in contact.

$$V = k_{\text{adh}} \frac{F_n\, s}{H} \tag{5.1}$$

Where, k_{adh} is the adhesive wear coefficient. However, this model does not consider the viscoelastic properties of elastomers or the adhesion properties. Also, because the hardness is in the denominator, it is generally assumed that wear will decrease with an increase in hardness. This is, however, not true in all cases due to the presence of the adhesive coefficient that can take values that differ in almost seven orders of magnitude. This limits the capabilities of this model to be used in predictive modelling. Kragelsky [79] stated that wear is positively dependent on hardness. In the case of aging, the oxidation of the surface layer is maximum. As a result, crosslinking and hence hardness is maximum at the surface. However, as we go deeper in the z-axis, the level of oxidation, crosslinking and the hardness decreases as compared to the surface layer. Moreover, aging leads to the formation of surface cracks and defects that further promote wear. This too cannot be modelled Hence, Archard's law cannot be used as is in this study.

The term $F_n.s$ in Archard's law is equivalent to work. Hence, we can say that the volume loss is directly proportional to the work done by friction (W_{fric}). Hence, we can model volume loss as

$$\Delta V = k_{adh} \left(W_{fric}\right)^n \tag{5.2}$$

Where, n is the exponential factor and is kept constant. Now, frictional work can be given by

$$W_{fric} = \mu\, F_n\ s\,, \tag{5.3}$$

$$s = v_s\, t \tag{5.4}$$

Where, μ is the friction coefficient. Now, the friction coefficient can be modeled using the viscoelastic properties as seen in the previous section. The friction coefficient can also be obtained from the tests conducted on the DFT.

5.2 EXPERIMENTAL SETUP

5.2.1 Sample Material and Geometry

The formulation of the compound used in this study has been discussed in Chapter 3 and found in Table 3.1. The geometry and CAD model of the sample is shown in Fig. 5.1.

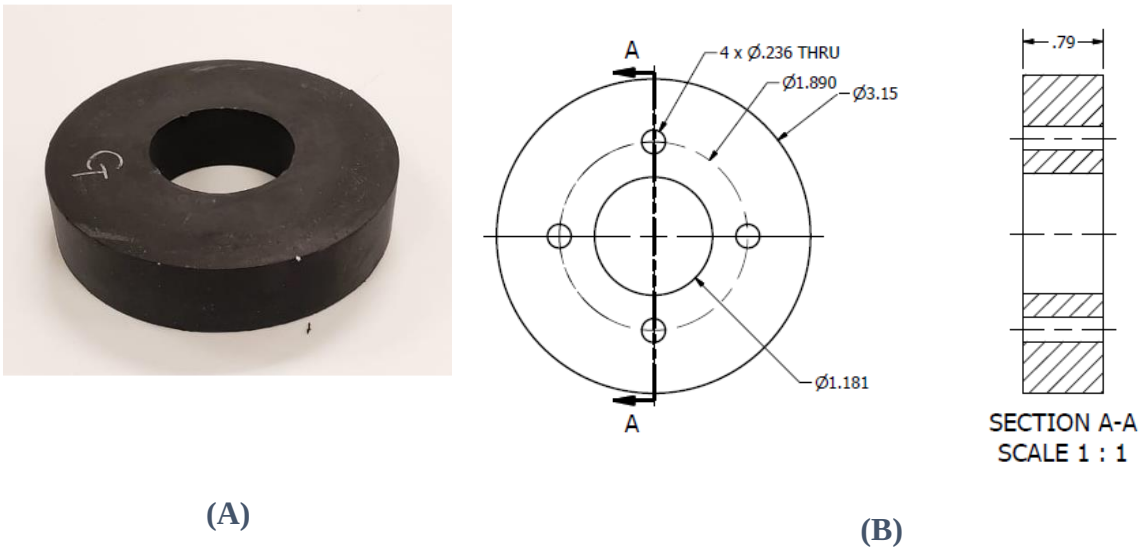

(A) **(B)**

Fig. 5.1: (A) Wear SBR Sample (B) Sample Dimensions

5.2.2 Dynamic Friction Tester and Abrasion Surface

Different types of indoor test rigs that use both sacaled samples as well as full-size tires can be found in the literature. In some cases, outdoor experiments are also carried out when different road surface micro and macro texture need to be studied. For this study, a Dynamic Friction Tester (DFT) was used to carry out the experiments. This test rig was built in-house at the Center for Tire Research (CenTiRe) lab. It is capable of conducting friction and wear experiments on circular elastomer compounds. Following are some of the inputs that can be varied in the DFT:

1) **Normal load/ Contact Pressure & Contact Area**

The frictional force is measured by a FUTEK load cell which measures the resistance of the compound to sliding in the longitudinal direction as shown in Fig. The test setup is also capable of dynamically measuring the normal load. A normal load input is provided which is calculated from the required contact pressure and area. Table 5.1 shows the normal load and the corresponding stationary contact area.

Table 5.1: Contact Area change with Normal Load

Normal Load (lbs.)	Area (mm^2)
10	185.52
20	262.97
30	316.49
40	354.42
50	395.39
60	441.65
70	474.51
80	494.75
90	530.39
100	535.79

2) **Slip velocity (disc and sample velocity)**

Slip velocity can be defined as the relative velocity between the tire and the road. In the case of the DFT, it is the difference in the linear velocity of the sample and the linear velocity point of contact on the disc.

$$v_s = (r\,\omega) - v_{disc} \tag{5.5}$$

Where, $r\ and\ \omega$ are the radius and angular velocity of the sample respectively. In this study, the slip velocity is kept constant at 0.025 m/s and hence accordingly the sample and disc rotational velocities are calculated.

3) Surface profile

The surface on the disc can be changed as per test requirements. Any surface which can adhere to the disk and that can be made into a 12-inch diameter disk with less than 0.75-inch thickness can be used. In this study, P60 grit sandpaper is used for all experiments.

4) Temperature inside test rig

The test rig is enclosed in an environmental chamber. As a result, the inside temperature of the test rig can be controlled. The temperature range for the test rig is from -20 °C to 50 degrees Celsius. This is especially helpful to observe wear at sub-zero and elevated temperatures.

5) % Oxygen in the test rig

Similar to the temperature, the oxygen percent can also be varied inside the test chamber. This is done by initially sucking out as much air as possible inside the chamber using a compressor. Then, nitrogen, which is an inert gas is pumped inside the chamber to reduce the oxygen levels. An oxygen level indicator is used to measure the oxygen concentration and we have achieved a low of 3-5% oxygen in the chamber. Again, this is very beneficial while studying the effects of oxygen and oxygen-based reaction that occur during the treadwear process.

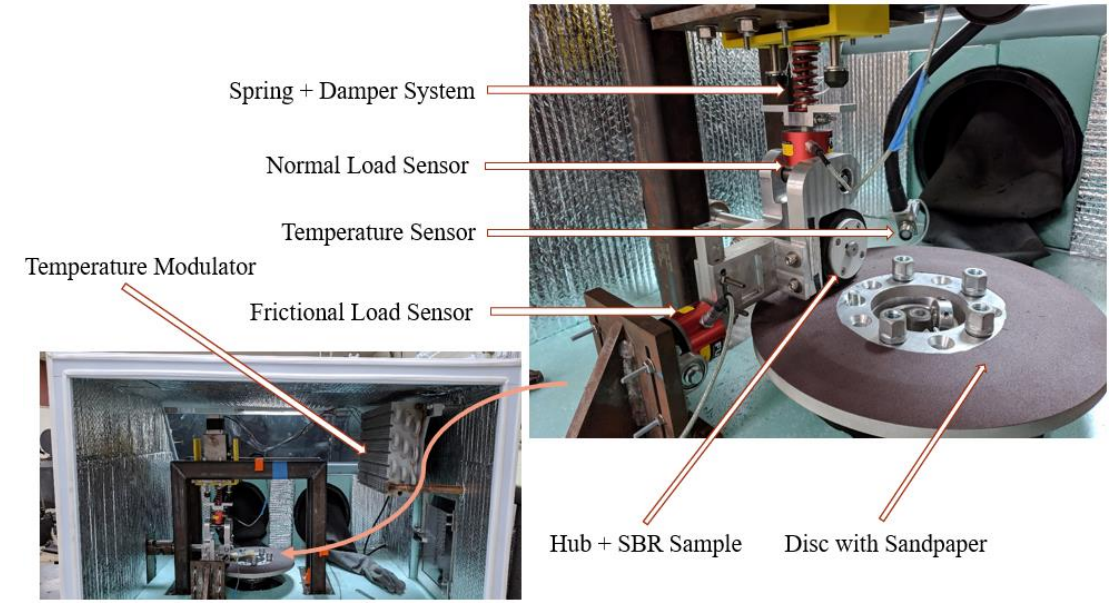

(A)

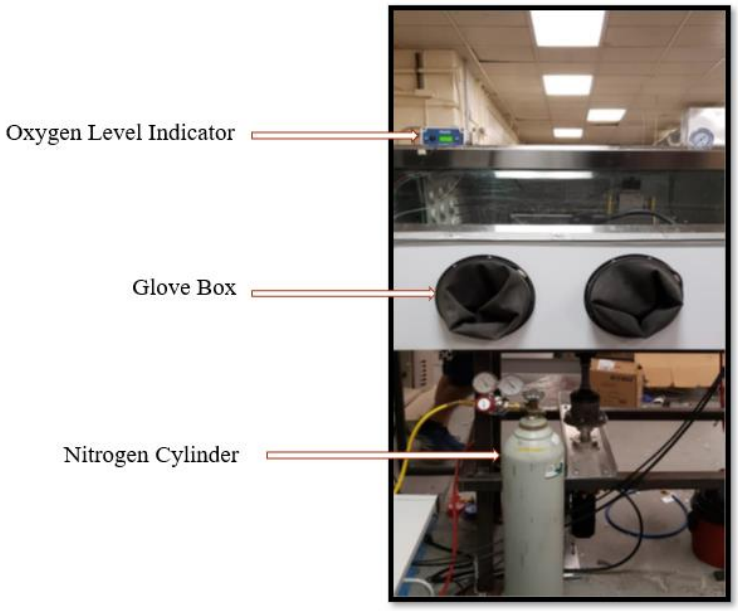

(B)

Fig. 5.2: Dynamic Friction Tester (A) Front (B) Back

For this study, the normal load slip velocity is kept constant at 10 lbs and 0.025 m/s respectively. Tests are conducted at room temperature without changing oxygen levels. Tests are run for

samples at various aging periods (uanged, 1, 2, 4 and 8 weeks aged) and temperatures (70 °C, 90 °C, 110 °C).

5.2.3 Measuring Scale

A Tree HRB Milligram Analytical and Precision Balance is used to measure the weight of the sample before and after each wear test. Fig. 5.3 shows the measuring scale with the SBR sample inside it. As seen, the weight of the sample alone (without the hub) is around 81.609 g. This number can vary slightly from sample to sample.

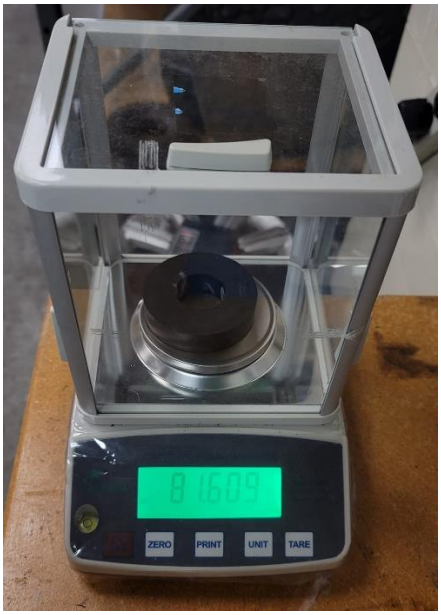

Fig. 5.3: Tree HRB Milligram Analytical and Precision Balance with SBR wear sample mounted

5.2.4 Experimental Procedure

The following test procedure was followed exactly during every wear test.

1) Take out the stored rubber samples from the cold storage/refrigerator around 3 hours before the start of the experimentation. This ensures that the material is brought back to ambient temperature and there is no change in the chemical or mechanical properties.
2) Open and configure LabVIEW to record data.
3) Clean the hub assembly using rubbing alcohol before mounting the samples on the hub. Clean off any debris on the disc as well.

4) Run the sample at 0.1 m/s sliding velocity at 50 lbs. normal load for 30 seconds. This ensures removal of the ay layer on the surface that inhibits wear (in case of aged samples this step is to be done before aging.)
5) Weigh the assembly on the precision balance and note down the initial weight in grams. Take three readings and average them out.
6) Insert the sample-hub assembly on the shaft. Tighten the collar and key the shaft.
7) Based on the test conditions, enter the values of the RPM of sample and disc in the Kollmorgen workbench
8) Start data acquisition in LabVIEW and set the load value
9) During the test, keep dusting the disc to remove debris (sample wear.)
10) Remove the hub-sample assembly and lightly rub off the excess dangling debris from the surface of the sample.
11) Measure the weight of the assembly again three times.
12) Repeat steps 5 to 11 until all test conditions are completed.

5.3 CHANGE IN FRICTION COEFFICIENT DUE TO AGING (VISCOELASTICITY MODEL)

5.3.1 Theoretical Estimation

Many researchers have tried to estimate the friction coefficient of rubber in the past. Some of the most notable studies have been performed by Persson. However, Persson's multiscale theory for rubber friction based on viscoelastic losses is very mathematically intensive and needs many experiments to find the equation parameters. However, this theoretical model was simplified and condensed into a much simpler model by Persson in 1998 and Popov in 2010 [80]. They have reduced the model from a multiscale model to a single scale with a large cutoff wavevector. Rubber friction can be divided into mainly two mechanisms: hysteresis and adhesion. The adhesion component of friction reduces considerably with an increase in surface roughness. Thus, we can conclude that the hysteretic component is dependent on the long-wavelength surface roughness whereas the adhesion will follow the short-wavelength surface roughness of the substrate.

Grosch experimentally showed that a single master curve can be obtained that showcases the velocity and temperature dependence of friction coefficient This was done using the WLF transform which is explained in detail in previous sections. He also proved experimentally that for rubber, two friction maxima exist: one due to adhesion component at slow speeds and the second due to viscoelastic losses at higher speeds. Heinrich [81] suggested that rubber follows a short-wavelength surface roughness profile especially at slow speeds and low roughness profiles and induces some adhesive friction components. He proposed his model given by Eq. (5.6).

$$\mu = C\,\frac{Im\,E(\omega_o)}{|E\,(\omega_o)|} \tag{5.6}$$

Where, $E(\omega_o)$ is the complex modulus of rubber from viscoelastic tests and $\omega_o \sim \frac{v}{l}$ is the frequency of deformation at velocity v and asperity diameter l. The constant C was assumed to be "unity" for very rough surfaces. In the case of the P60 sandpaper, the average diameter of asperity is around 250 μm. Thus, the frequency is around 100 Hz. Now, replacing ω_o=100 in Eq. (5.6), we get the following values of friction coefficient as shown in Table 5.2.

Table 5.2: Friction Coefficient: Heinrich Model

Aging Time	Friction Coefficient (μ)
Unaged	0.341
2-week	0.344
4-week	0.360
8-week	0.349

Popov [80] also arrived at a similar equation as Eq. (5.6). Instead of a constant, he used the RMS slope of the surface. In literature, the RMS value for a rough surface is ~ 1.3.

$$\mu = h'_{rms}(q_1)\frac{\text{Im}\;E(\omega_0)}{|E(\omega_0)|} \tag{5.7}$$

Where, q_1 is the large cut-off vector which depends on the surface profile.

M. Ciavarella [1] proposed a slightly modified version of Popov's equation given by Eq. (5.8).

$$\mu \simeq h'_{rms} \frac{\text{Im } E(q_1 v)}{|E(q_1 v)|} \tag{5.8}$$

Furthermore, the PSD of 120 grit sandpaper was performed and analyzed by Sunish Vadakkeveetil in his doctoral dissertation [9]. The small wave vector cutoff (q_0) was found to be $10^{3.3}$ and the large wave vector (q_1) was found to be 10^6. Thus, for a 60-grit sandpaper, with average particle diameter almost double as that of P120 sandpaper, we assume $q_1 = 10^4$. The sliding velocity between the disc and sample was 0.025 m/s. This gives us the frequency of deformation $q_1 v = 250\, Hz$. Now, the values of complex modulus and loss modulus can be substituted from the DMA data into Eq. (5.8) to get the theoretical estimation of friction coefficient. This is done for different aging conditions as well as seen in Table 5.3.

Table 5.3: Friction Coefficient: M. Ciavarella Model

Aging Time	Friction Coefficient (μ)
Unaged	0.526
2-week	0.530
4-week	0.542
8-week	0.532

There is a difference in the friction coefficient values between the two models. The Ciavarella model predicts the friction coefficient to be higher than the Heinrich model. This is mostly due to the rms constant that is multiplied with the loss to complex modulus ratio and the fact that the frequency used in the latter is lower. In general, for both the models, the friction coefficient increases with aging time and then decreases as seen in Table 5.3. This is because, the stickiness of rubber decreases, and the hardness increases simultaneously as it is aged. As both these models are completely based on the viscoelastic losses (hysteresis friction) and other friction components are not considered (Section 2.1.1). Further experimental investigation is conducted in the subsequent sections of this work to understand the actual friction values.

5.3.2 Experimental Results

The DFT setup has the capability to dynamically output the normal load as well as the frictional force for the SBR sample under study. Thus, using this data, the friction coefficient of the SBR sample for various aging conditions can be found. The friction coefficient can be found by simply dividing the frictional force by the normal force acting on the sample. One such example for an unaged sample is shown below. As seen in Fig. 5.4, for an unaged SBR sample, the static friction coefficient is ~ 1.1 and the average dynamic friction coefficient is 0.41.

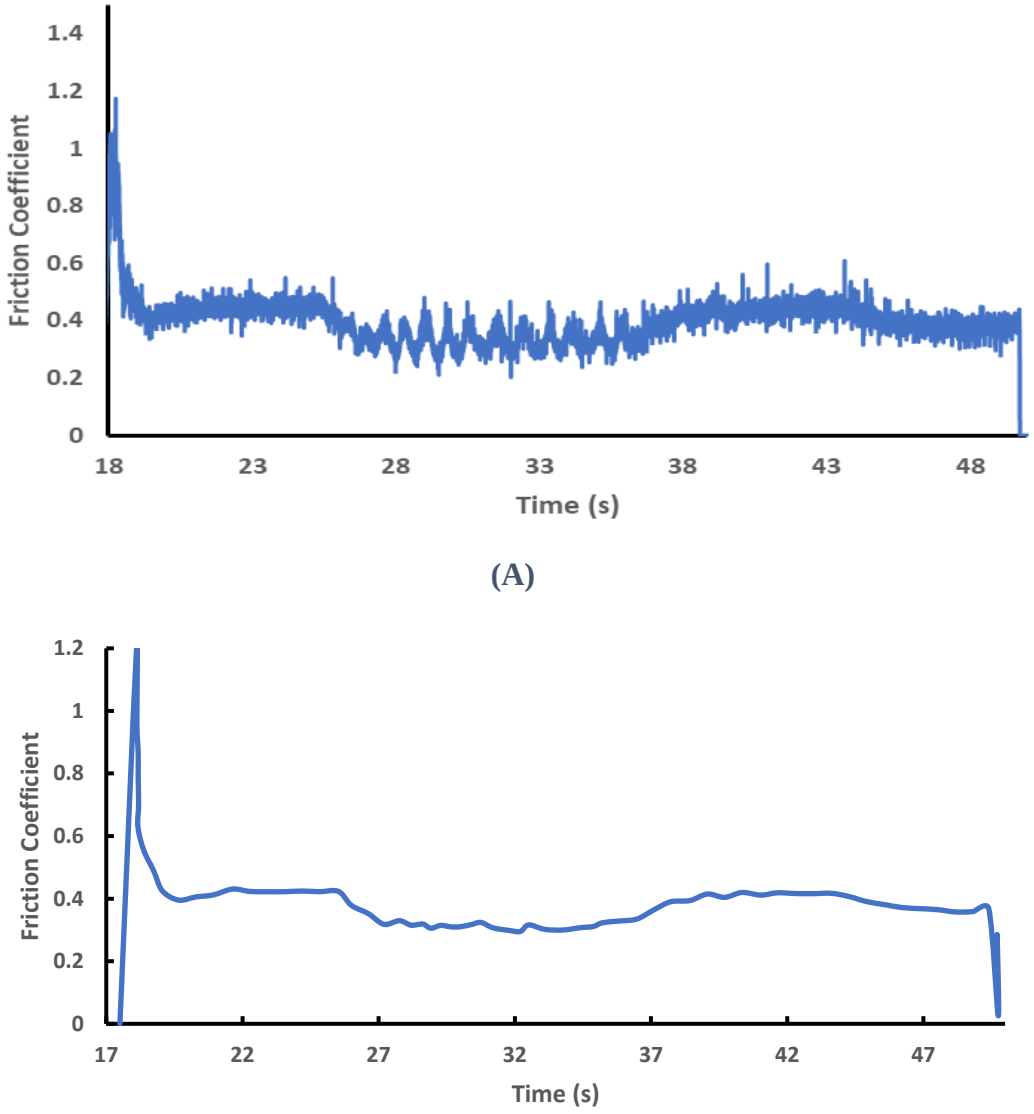

Fig. 5.4: Friction Coefficient curve for unaged sample (A) Unfiltered (B) After Filtering

As seen in Fig. 5.5, for 70 C aged sample, the static friction coefficient remains almost the same at around 1. However, the dynamic friction is around 0.61 for the four-week aged sample and around 0.72 for the 8-week aged sample for the first 10 seconds and then the friction coefficient reduces to 0.43 again. The thickness of the SBR wear samples is very high. This means that only the surface of the samples is aged. As seen in Fig. 5.5, the dynamic friction coefficient is initially high which corresponds to the surface of the samples which is fully aged. However, as the aged layer is worn off, the friction coefficient again goes back to the unaged friction coefficient which is around 0.42. Not much difference is observed in the 1-week aged sample and the dynamic friction coefficient average is around 0.43.

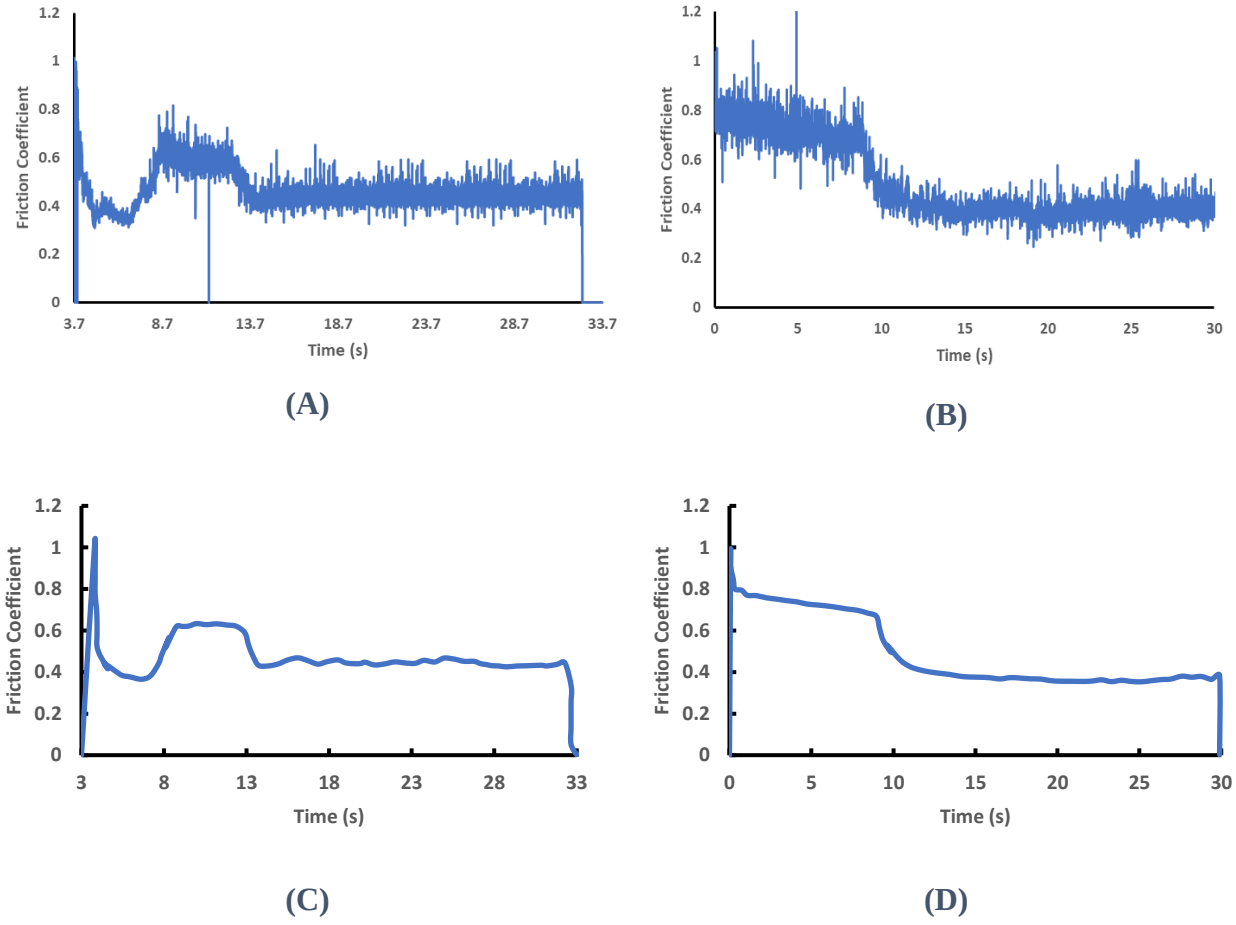

Fig. 5.5: Friction Coefficient curve for (A) 4-week aged sample (B) 8-week aged sample (C) 4-week aged sample Filtered (D) 8-week aged sample Filtered

The experimental friction coefficients vary as compared to the ones predicted by the analytical models. The experimental results and the Ciavarella model have similar values of friction coefficient for the unaged condition. However, as the aging time increases, the experimental

friction coefficient is higher than the one predicted from the models. This may be because the model predicts only the friction coefficient component due to viscoelastic losses. The adhesive, viscous and cohesive friction losses are not considered in this study. Moreover, the model does not consider the effects of surface cracks formed because of aging which changes the micro texture of the sample considerably.

5.4 WEAR TEST RESULTS AND ANALYSIS

Wear tests were conducted on the DFT at a fixed load of 10 lbs. and sliding velocity of 0.025 m/s. For each test, three samples are used, and their weights are averaged out to get mass loss. Tests are conducted on samples after free-rolling (FR) of samples to remove the wax layer on the surface and without its removal. This is to also study how much effect the wax has on aging and eventually wear. The results for the wear tests are shown in Table. 5.4.

Table 5.4: Mass and Volume loss of SBR during wear tests at various Aging Time and Temperatures

70 °C			
Aging Time	**Mass loss (g)**	**Volume loss (cm^3)**	**Friction Coefficient**
Unaged	0.070	0.074	0.41
1-week	0.081	0.086	0.43
2-week	0.096	0.102	0.49
4-week	0.143	0.151	0.61
8-week	0.166	0.176	0.72
90 °C			
Aging Time	**Mass loss (g)**	**Volume loss (cm^3)**	**Friction Coefficient**
Unaged	0.07	0.074	0.41
1-week	0.088	0.093	0.42
2-week	0.098	0.104	0.55
4-week	0.150	0.159	0.63
8-week	0.169	0.179	0.69
110 °C			
Aging Time	**Mass loss (g)**	**Volume loss (cm^3)**	**Friction Coefficient**
Unaged	0.072	0.076	0.41
1-week	0.094	0.100	0.45
2-week	0.11	0.117	0.57
4-week	0.149	0.158	0.66
8-week	0.197	0.209	0.76

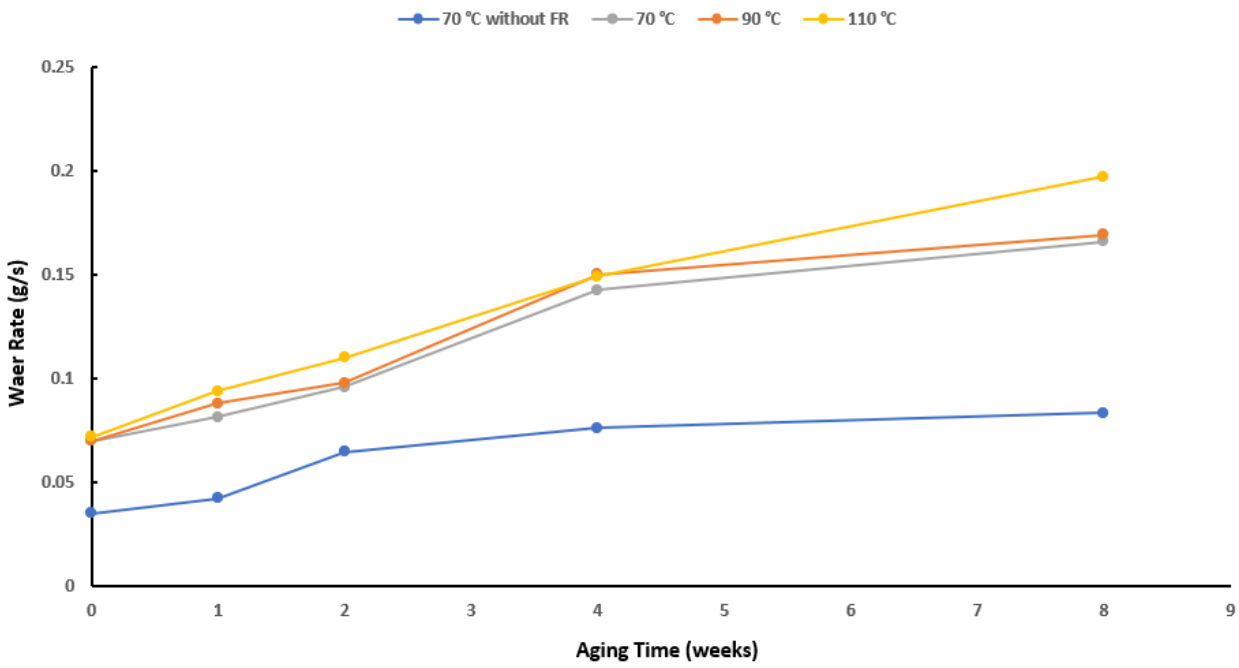

Fig. 5.6: Change in Wear rate with Aging Time and Temperature

Thus, we see that the wear rate observed after free rolling and aging of samples is much higher (almost double) than without performing free rolling prior to aging. This indicates that the wax layer plays a major role in reducing the effect of aging. However, it should also be considered that free-rolling generates abrasion and thus more surface cracks. These cracks serve as a site for reactions and oxygen permeation during oven aging which is hindered to a great extent by the wax layer. Furthermore, these cracks and surface defects help in further crack propagation and the formation of rolls of SBR. All this explains the increased wear rate.

With an increase in aging time, we see a steady increase in wear rate. This is due to the increased brittleness of the surface rubber as well as the cracks formed on the surface due to aging. With aging temperature, we do not observe a huge increase in wear rate. This may be due to the high thickness of the sample which hinders sub-surface aging.

Now that we have the friction coefficients for all aging times and temperatures, we can find out the Frictional Energy (FE) or work done by friction (w_{fric}). Eq. (5.2) can be modified by taking logarithm on both sides, giving us Eq. (5.9).

$$\log \Delta V = \log k_{ahesive} + n \log(W_{fric}) \quad \textbf{(5.9)}$$

Comparing Eq. (5.9) with y = mx + c, we get a linear plot of $\log \Delta V$ vs $\log(W_{fric})$ with $\log k_{ahesive}$ as the intercept and n as the slope.

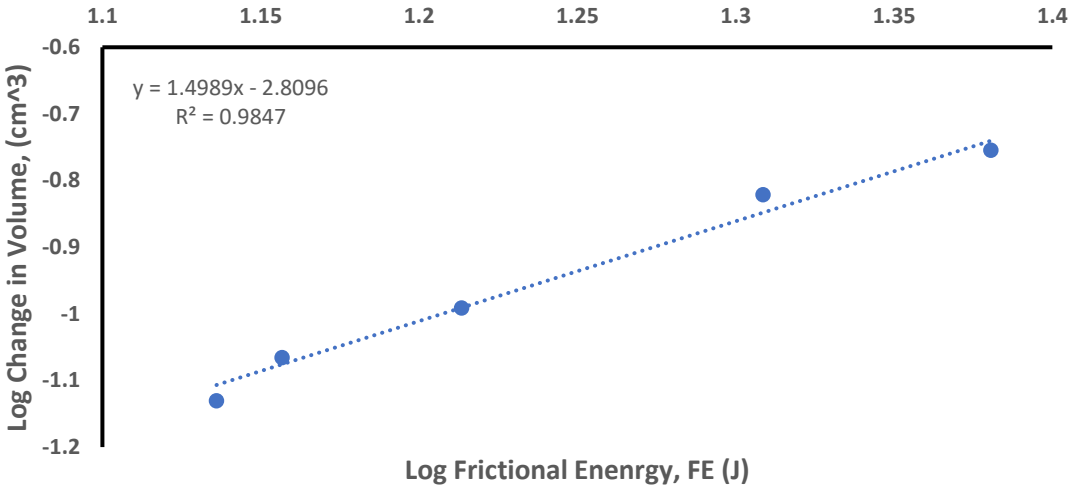

(A)

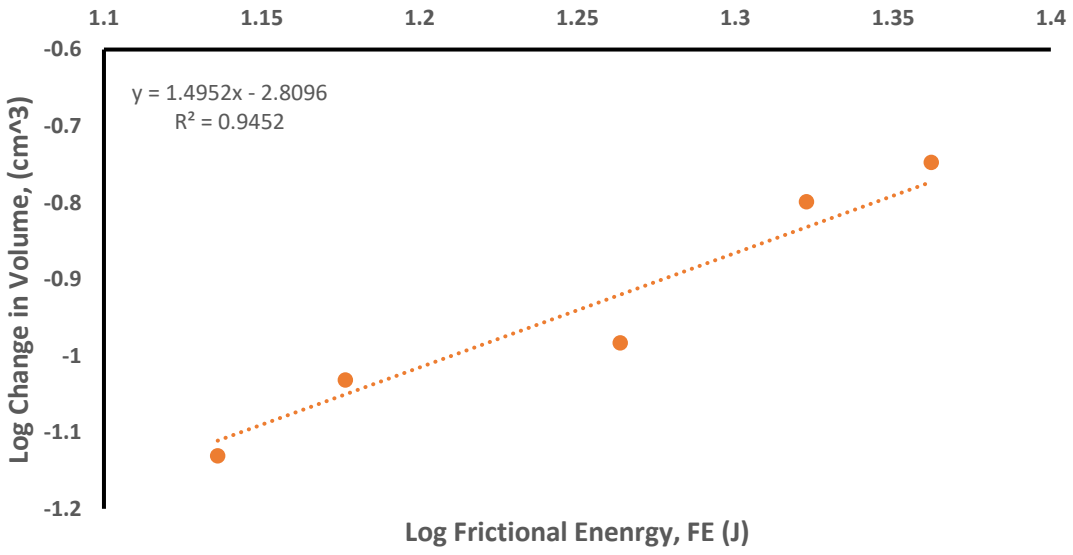

(B)

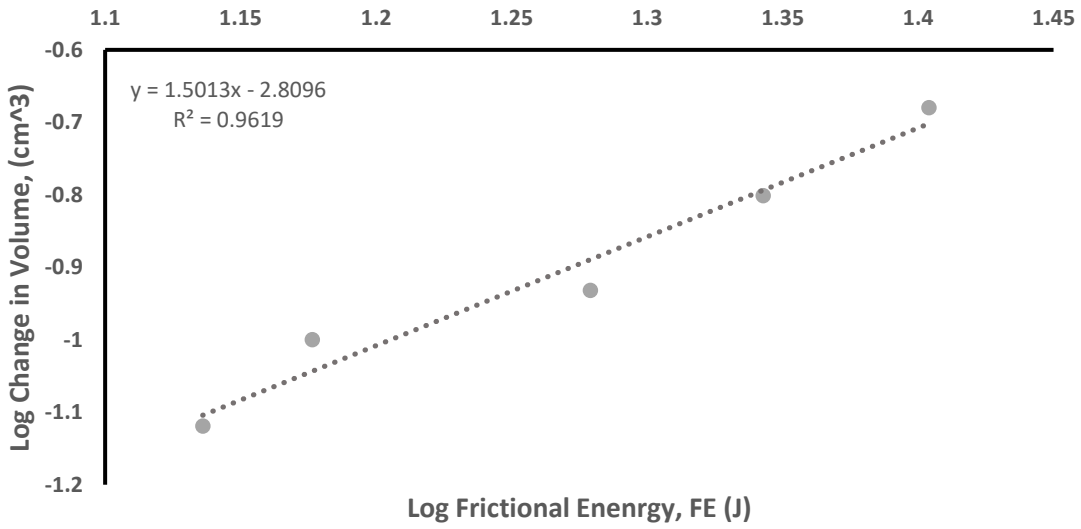

(C)

Fig. 5.7: Log Volume Change vs Log Frictional energy for (A) 70 °C (B) 90 °C (C) 110 °C Aging temperatures

From Fig. 5.7 we see an excellent linear correlation between log volume change and log frictional energy. This means that Archard's law can be used to model volume loss as a function of frictional energy.

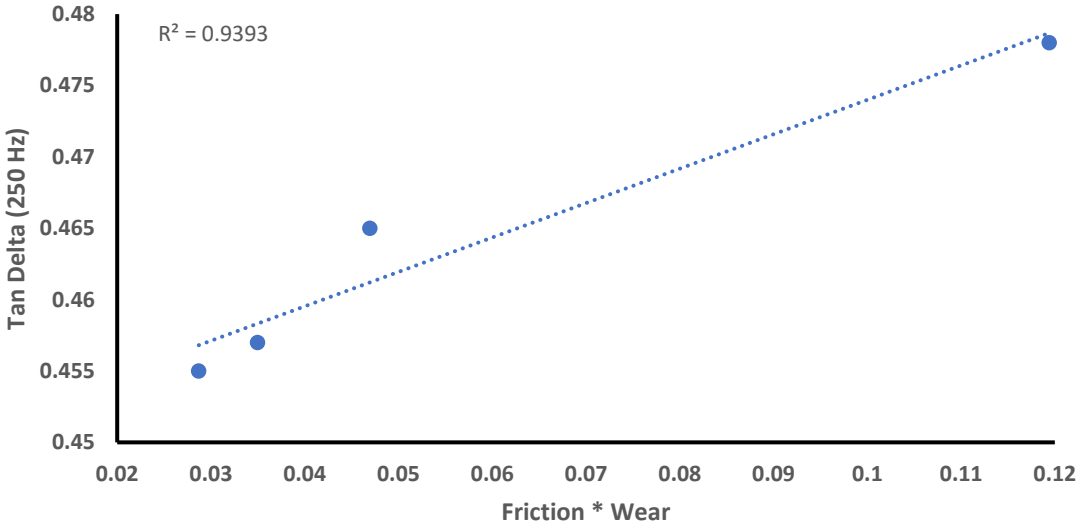

(A)

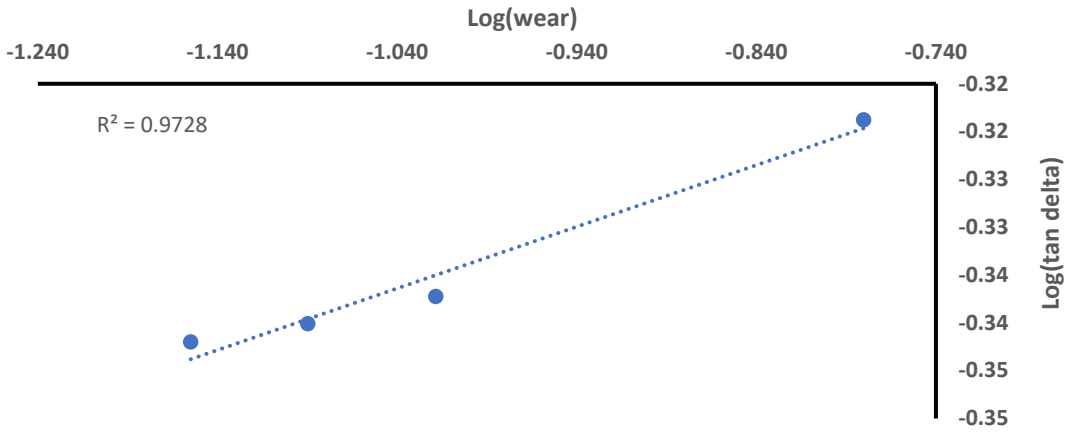

(B)

Fig. 5.8: (A) Tan Delta vs Wear* Friction plot (B) Log (tan delta) vs Log (wear) plot

Now, the 'log(wear) vs long tan delta' and the 'tan delta vs friction*wear' for 70 °C aged SBR are plotted in Fig. 5.8 (A) and (B). The graphs clearly show a linear correlation between wear and tangent delta. This further proves the dependence of friction and wear characteristics on the viscoelastic properties of rubber.

6 SBR LIFETIME PREDICTION BASED ON HYPERELASTIC PROPERTIES

Elastomer properties and lifetime prediction are paramount in ensuring the reliability and safety of components. This has become increasingly important in today's time due to environmental concerns as well as the use of elastomers in mission-critical applications. This section will discuss various models that can be used to predict the lifetime of SBR at various temperatures. The main damage considered in this study is the thermo-oxidative aging that occurs in SBR during use. Other factors such as ozone, humidity, working conditions, etc. also play an important role in rubber degradation. However, studying all these factors at once and preparing a model is very difficult because of the complex chemical reactions and interactions taking place in SBR. Hence, in this study, we have focused on one of the most common and detrimental types of aging that occurs in rubber which is due to the combined effects of oxygen and temperature. As seen earlier, when SBR is aged, it becomes brittle and rigid due to the crosslinks formed, loses its damping capabilities, forms cracks and surface voids, etc. This significantly affects the rubber lifetime as well. Different models used in this chapter are shown in Fig. 6.1.

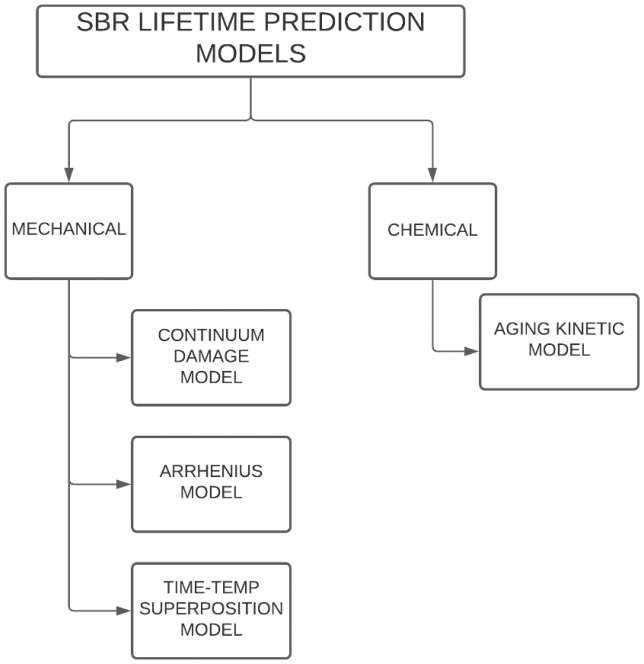

Fig. 6.1: SBR Lifetime Prediction Models

6.1. CONTINUUM DAMAGE MECHANICS (CDM) MODEL

The CDM model has been discussed in Section 3.4.2 wherein, the model was used to predict the damage state variable (D) of SBR at any given aging time and temperature. The damage variable D is defined between 0 to 1. Zero being unaged condition and one being fully aged condition. For this study, 90% damage is considered to be the limit of SBR and hence in turn, its lifetime. This translates to D = 0.9 as the limit. The extrapolated curves till 90% damage of SBR are shown in Fig. 6.2. Table 6.1 shows the lifetime prediction for various temperatures.

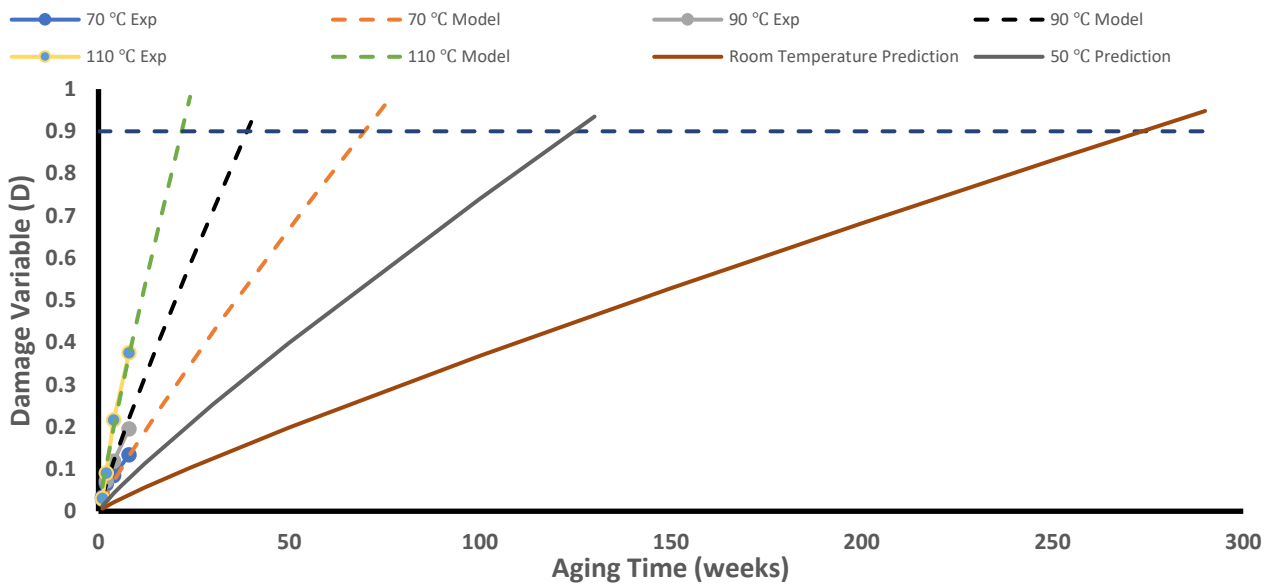

Fig. 6.2: Damage Variable Evolution and Lifetime prediction of SBR at various Aging Temperatures

As seen in both Fig. 6.2 and Table 6.1 the lifetime for SBR does not change linearly with temperature. This means that higher temperature speeds up the aging kinetics. Hence, at temperatures around 5 °C, the kinetics are very slow and aging proceeds at a very slow pace. Hence, tires and elastomers are often stored at sub-zero temperatures and in an inert environment to reduce the aging effects significantly and hence increase the life of the product.

Table 6.1: SBR Lifetime Prediction at various aging temperatures (CDM Model)

Aging Temperature (°C)	SBR Lifetime (90% Damage)
5	~ 9.5-10 years
25	~ 5.5 years
50	~ 2.5 years
70	~ 1.5 years
90	~ 40 weeks
110	~ 20 weeks

6.2 ARRHENIUS EQUATION-BASED MODEL

As seen in the previous section, using the CDM model, we can estimate the damage in the material at a macroscopic scale due to aging. However, this is not very intuitive as we do not have a very strong idea about the exact values of the mechanical properties. Strain/elongation at break is one such property that can be used to determine the lifetime of SBR. The Arrhenius equation-based model will be able to predict the strain at break depending on aging conditions and ultimately its lifetime.

The Arrhenius equation Eq. (6.1), has been used widely to predict lifetimes of materials where temperature effects are involved

$$K = A\, e^{\frac{-E_a}{R\,T_k}} \tag{6.1}$$

Where K is the property under study, A is the pre-exponential factor, E_a is the activation energy, R is the universal gas constant (8.3144 J/K) and T_k is the absolute temperature. It has been observed in the literature [82] that CLD increases with increasing time and temperature. However, the slope decreases as the material ages till it reaches a plateau. This behavior is also

verified in Section 4.4 by calculating the change in CLD with aging time from DMA data. Moreover, if we plot the results of strain at break for aged samples normalized by the strain at break for unaged samples for various aging times, we see a similar trend. Hence, it is safe to assume that both these parameters (strain at break and CLD) change in a similar form with time and temperature. Thus, they can be modelled using a modified form of an Arrhenius equation.

Such use of Arrhenius equation and CLD change to model various parameters such as Ultimate Tensile Strength (UTS), strain at break, and secant modulus of NR compounds has already been studied and implemented by Korba [56] in his doctoral dissertation. His approach is used for predicting the strain at break for SBR compounds in this study.

Now, replacing the property K in Eq. (6.1) by normalized strain at break (λ_j/λ_o), and mirroring the equation (strain at break decreases with increase in aging time and temperature) we get Eq. (6.2).

$$\ln\left(\frac{\lambda_j}{\lambda_o}\right) = \left(\frac{-1}{A}\right) e^{\frac{-E_a}{R\,T_k}} \tag{6.2}$$

Now, the pre-exponential factor A was modified to include the aging time and temperature effects given by Eq. (6.3).

$$A = (1/t)e^{(X_1 - X_2 \cdot T_k)} \tag{6.3}$$

Where X_1, X_2 are fitting constants and t is the aging time in hours.

$$\ln\left(\frac{\lambda_j}{\lambda_0}\right) = (-t.\, e^{X_2\, T_k - X_1})\; e^{\frac{-E_a}{R\,T_k}} \tag{6.4}$$

The values of fitting constants X_1, X_2 and the activation energy (E_a) were determined by curve fitting the normalized strain at break data to Eq. (6.4).

Fig. 6.3 shows the normalized strain at break data as a function of aging time and temperature along with the fitted curves for the respective conditions. Now, similar to the CDM model, the Arrhenius equation-based can also be used to predict SBR lifetime. This is done by extrapolating the model curves seen in Fig. 6.3. The limit set for normalized strain at break is 0.1. This means that the material has degraded to 10% of its original strength. This is shown in Fig. 6.4 and predictions are made for 50 ℃ and 25 ℃. Again, we observe a non-linear change in the strain at break with a function of aging time and temperature.

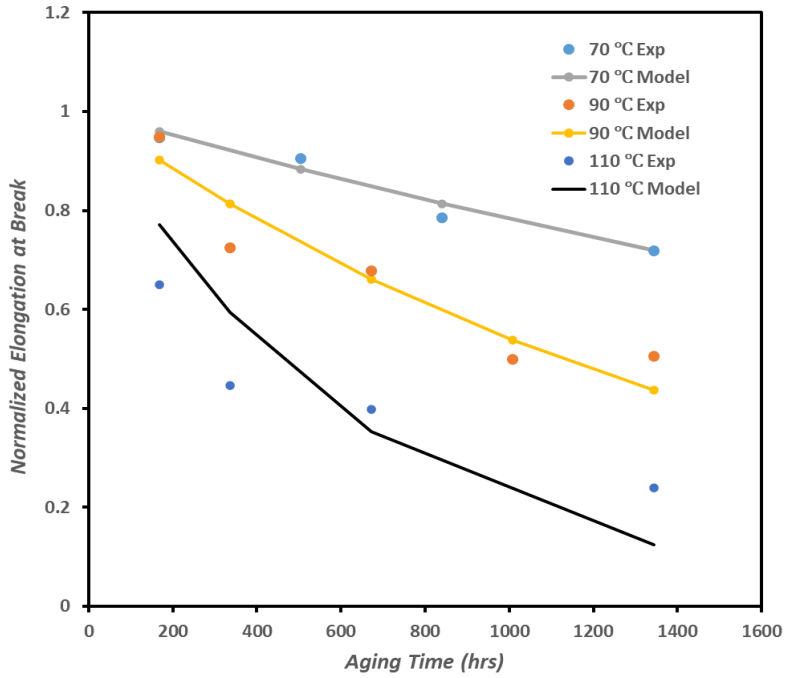

Fig. 6.3: Normalized Strain at Break- Experimental Data and Arrhenius Model estimate

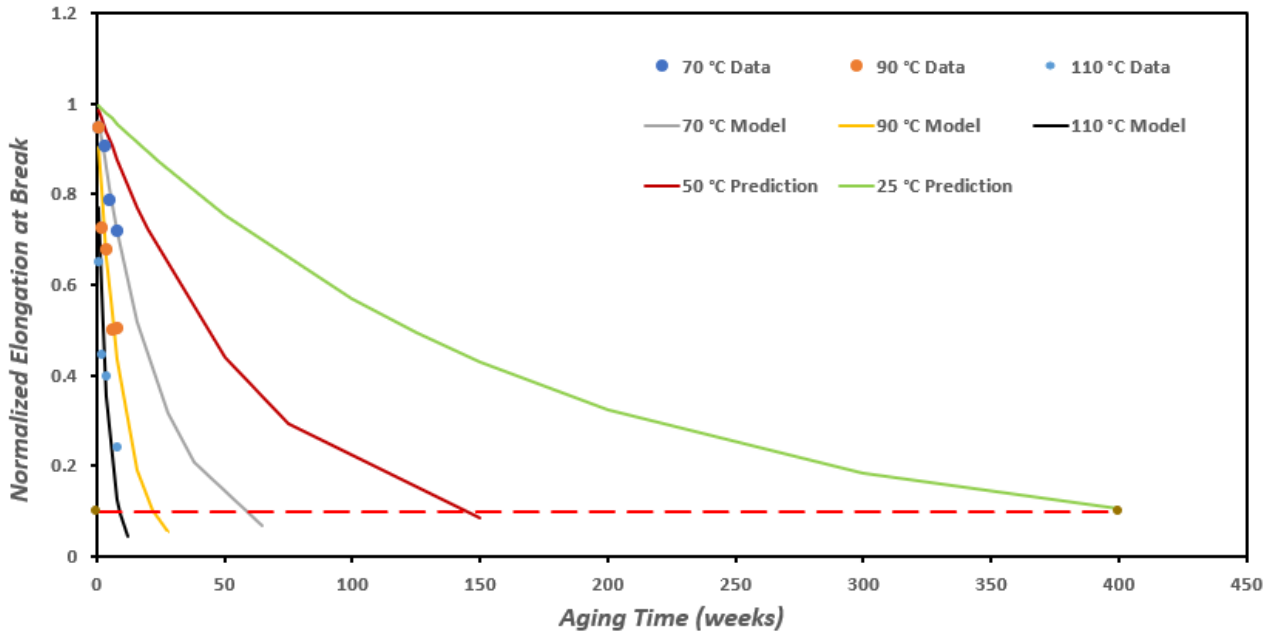

Fig. 6.4: SBR Lifetime Prediction: Arrhenius based Model

Table 6.2: SBR Lifetime Prediction at various aging temperatures (Arrhenius Equation Model)

Aging Temperature (°C)	SBR Lifetime (10% Normalized Strain at Break)
25	~ 8 years
50	~ 3 years
70	~ 1.25 years
90	~ 25 weeks
110	~ 12 weeks

6.3 AGING TIME-TEMPERATURE SUPERPOSITION PRINCIPLE MODEL

The TTS principle was discussed briefly in Section 4.1.3. TTSP is a widely used concept in polymer physics. It is generally used to characterize viscoelastic behavior at a different time or frequency ranges as seen in Section 4. The principle states that time and temperature are correlated and can be used interchangeably. It means that instead of measuring a property change at a lower temperature and waiting for long periods, the material can be subjected to a higher temperature and get the same amount of change in a shorter time. However, it must be ensured that the underlying mechanisms that induce the changes in properties should not change. A simple way to ensure this is to observe the shape of the curves at various aging temperatures for a fixed interval of aging periods as shown in Fig. 6.5. The decrease in the strain at break is consistent with the change in temperatures. Hence, the TTSP can be used in this study to predict the lifetime of SBR. In this study, three temperatures and four aging periods are used. However, for better prediction and a higher range of values, the material needs to be aged at more time intervals and temperatures.

A reference curve was selected, which in this case corresponded to 70 ℃ aging temperature. The other two curves were shifted horizontally to the right till a smooth curve was obtained. The shift factor (a_T) is recorded for the 90 ℃ and 110 ℃ aging curves. This will give a prediction of normalized strain at break for 70 ℃ aging temperature.

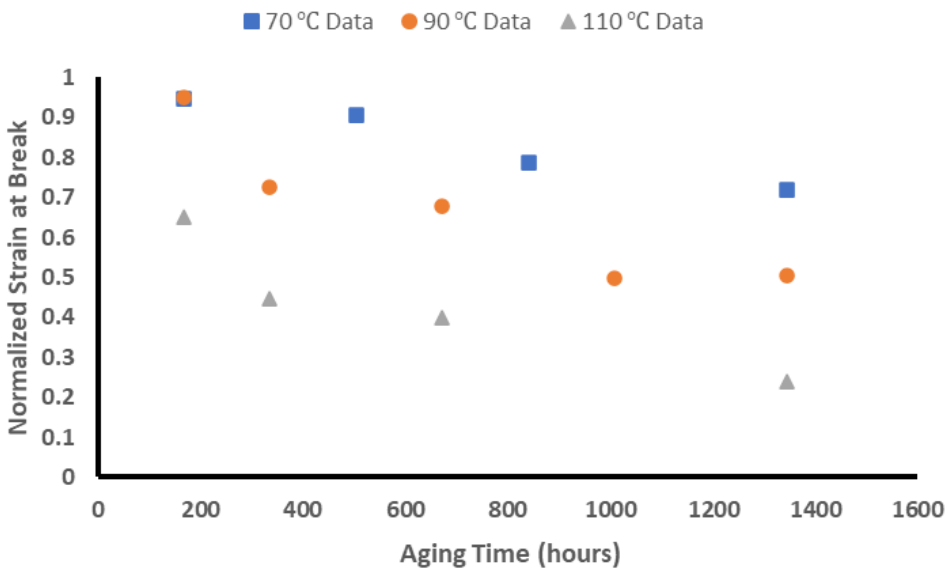

Fig. 6.5: Normalized Strain at Break- Experimental Data

The finalized master curve can be seen in Fig. 6.6. The shift factors are plotted against the aging time and a shift factor plot is obtained as seen in Fig. As we can see, the shift factor plot is almost linear. However, this needs to be confirmed further by doing more experiments. Fig. 6.6, predicts that it will take approximately 60-65 weeks (~1.2 years) for the material to have a normalized strain at break of 0.25 which corresponds to 75% degradation in strength.

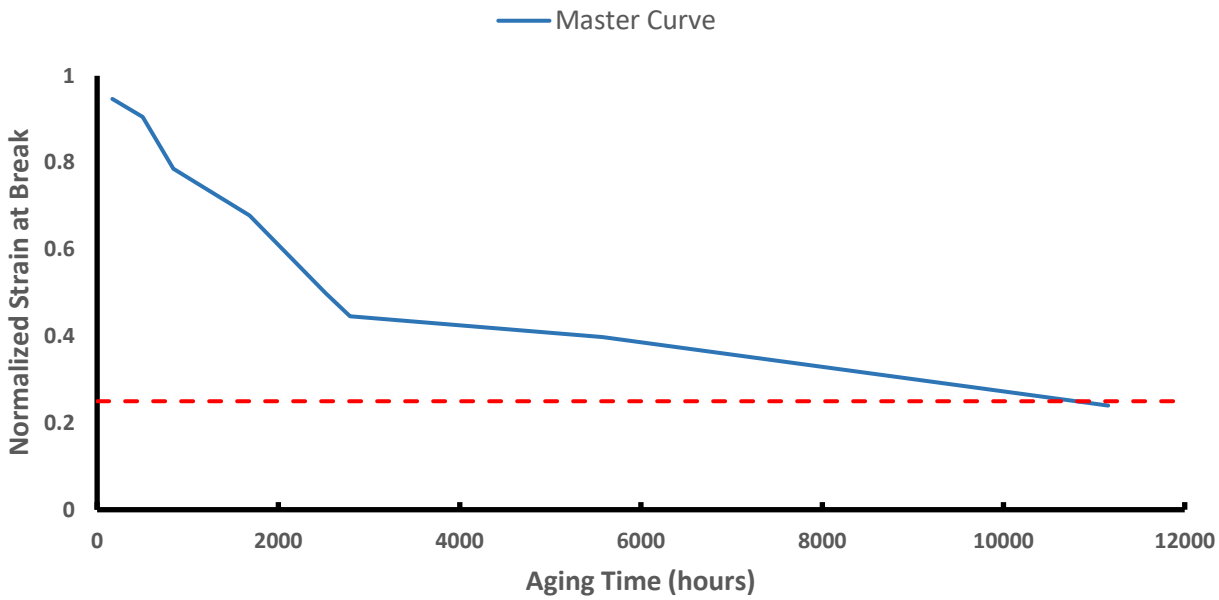

Fig. 6.6: Master Curve for Normalized Strain at Break vs Aging Time at 70 ℃ reference temperature

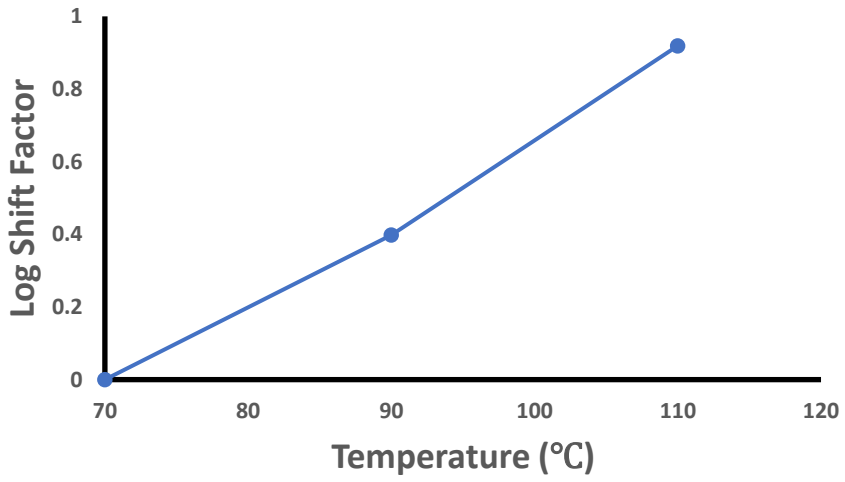

Fig. 6.7: Aging Shift Factor Plot

6.4 FT-IR BASED AGING KINETIC MODEL

The FTIR spectra of SBR aged samples at 90 C was discussed in Section 3.3.2. Similarly, the FTIR is conducted for other aging temperatures as well and their spectra are shown in Fig. 6.8. In

order to study the aging kinetics, the peak around 2800 cm^{-1} which corresponds to C-H stretching is utilized owing to its strong intensity and resolution. It has to be understood that the aging reactions are quite complex, and their products are diverse. Hence, it is very difficult and almost impossible to study these reactions (corresponding to different peaks in FTIR spectra) one by one. Hence, to simplify this process, three typical reactions that generally take place during aging are studied. They are:

1) Oxidation
2) Oxidative Crosslinking
3) Thermal Crosslinking

First, polymer oxidation is a common reaction between oxidative species and polymers, emerging oxygen-containing groups. Similarly, oxidative crosslinking is the reaction between two polymer chains and oxidative species, forming an ether crosslink. Both reactions consume C-H groups, and therefore, reduce the C-H stretching signal on the FTIR. Lastly, the isoprene moiety in the SBR rubber can be thermally initiated and induce thermal crosslinking with a neighboring isoprene group, yielding the C-C crosslink, which is difficult to detect by FTIR due to its symmetric nature. Based on these reactions, the kinetic equation can be given as Eq. (6.5) and Eq. (6.6).

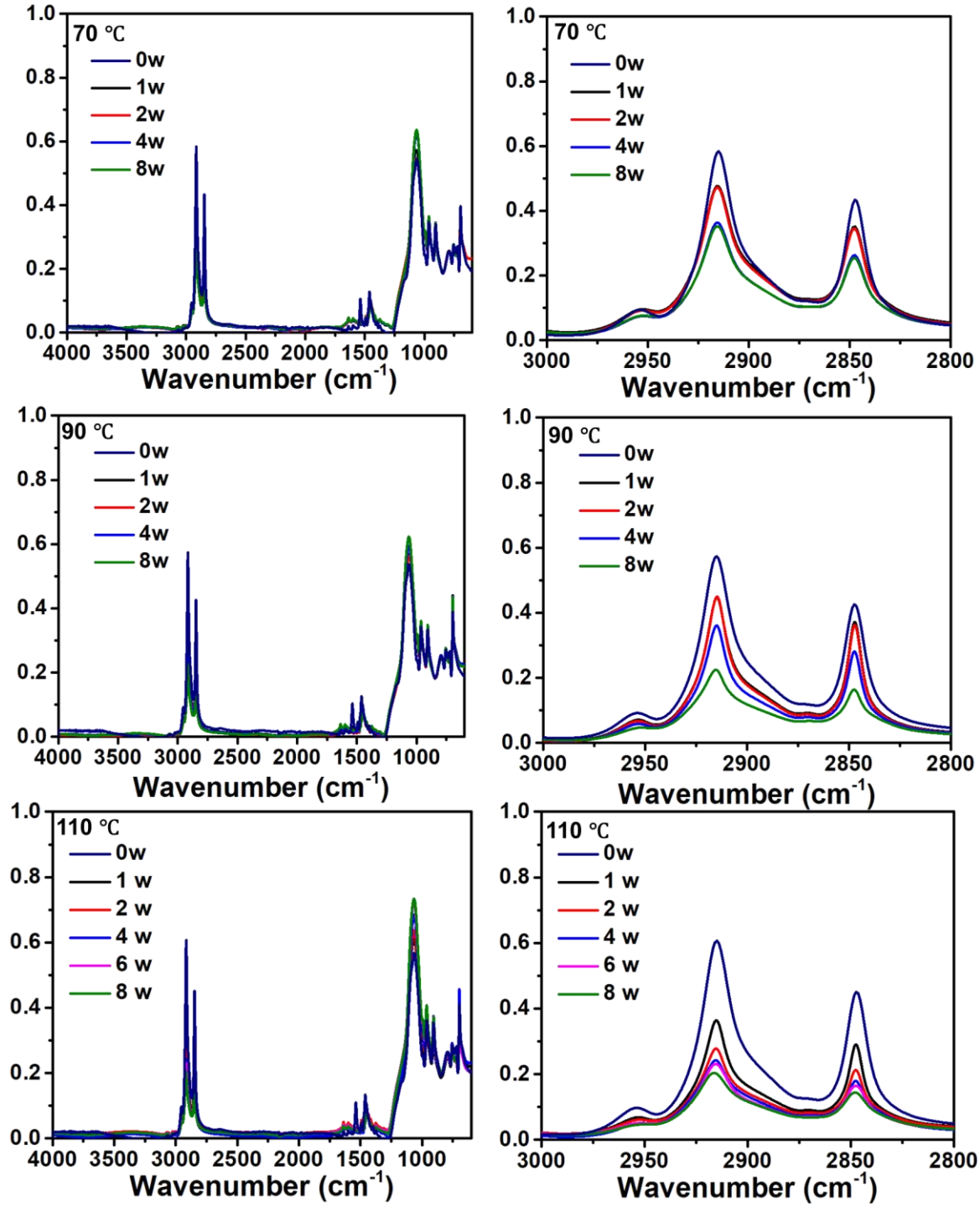

Fig. 6.8: Left: FTIR Spectra of SBR at various Aging Temperatures; Right: Zoomed in spectra (3000 to 2800 cm^{-1})

$$\frac{d[C-H]}{dt} = k_1[O][C-H] + k_2[O][C-H]^2 - X([C=C]) \quad \textbf{(6.5)}$$

$$\frac{2}{tan\left(\frac{k_1 + 2k_2[C-H]}{\sqrt{-4Xk_2 - {k_1}^2}}\right)\sqrt{-4Xk_2 - {k_1}^2}} = t \quad \textbf{(6.6)}$$

Where, k_1, k_2 and X are the kinetic constants of oxidation, oxidative crosslinking, and thermal crosslinking reactions respectively. X and [O] are assumed to be constant. The assumption of a constant X results in a constant thermal crosslinking rate at all reaction periods. Such assumption will lead to a considerable discrepancy with the reality when the thermal crosslinking reaction is a dominant aging reaction. However, according to the FTIR, reactions that consume the C-H group have outweighed the reaction yielding C-H group. Therefore, the assumption of a constant X([C=C] is to some extent reasonable.

Table 6.3: Kinetic Constants for various Aging Temperatures

Aging Temperature (°C)	k_1	k_2	X	R2
70	0	0.217	-0.088	0.917
90	0	0.294	-0.119	0.98
110	0	0.408	-0.165	0.945
50	0	0.148	-0.060	-
30	0	0.097	-0.039	-

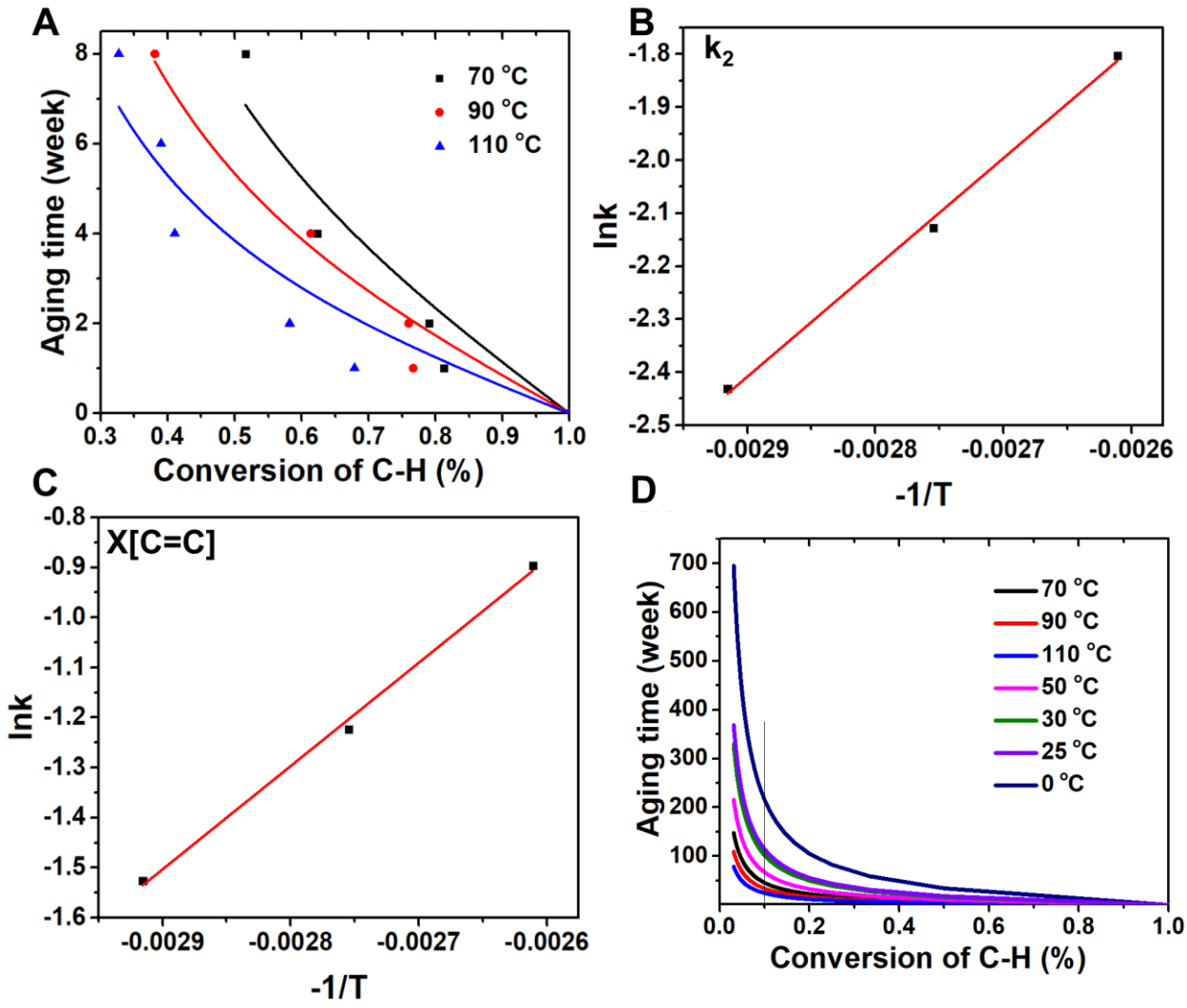

Fig. 6.9: (A) Kinetic equation curve fit (B) k_2 prediction (C) X[C=C]; prediction (D) Extrapolation of C-H Conversion

The FTIR data is then curve fitted to Eq.(6.6) as seen in Fig. 6.9 (A). We observe a reasonable curve fit even after the bold assumption regarding the thermal crosslinking being constant. The kinetic constants are compiled in. An interesting observation made is that k_1 for all aging conditions is almost 0. This indicates an absence of oxidation reactions. This is further confirmed by the absence of carbonyl and hydroxyl groups in the FTIR spectra. On the other hand, the rates of oxidative and thermal crosslinking increased with aging time and temperature. This in turn leads to an increase in CLD and higher modulus. The kinetic constants can now be extrapolated to other aging times and temperatures as well. Table 6.3 and Fig. 6.9 (B)-(C) show the extrapolated constants for 50 C and 30 C. Now, using these kinetic constants, the C-H

conversion at the various aging time and temperatures is shown in Fig. 6.9 (D). If we set 10% conversion of the C-H group as the end of service life of SBR, the lifetime for various temperatures is shown in Table 6.4.

Table 6.5: SBR Lifetime Prediction at various Aging Temperatures (Aging Kinetic Model)

Aging Temperature (°C)	SBR Lifetime (10% C-H bond conversion)
25	~ 2.5 years
50	~ 1.5 years
70	~ 1 year
90	~ 0.7 year
110	~ 0.5 year

6.5 Comparing Models

So far, we have studied four different types of approaches to predict SBR lifetime. However, the models give some variation in terms of their results. It is interesting to note that the CDM model predicts 90% damage of SBR at room temperature at around 270 weeks which roughly translates to around 5.5 years. NHTSA also recommends against using unused tires stored at room temperature after 5-6 years of storage over concerns due to aging. The CDM model estimate closely aligns with this as well.

Both the Arrhenius and TTSP models are based on the same principle of maximum strain at break. The Arrhenius model is able to predict the lifetime of SBR for any given aging temperature. However, in the case of the aging TTSP model, the prediction capability largely depends on the experimental data and the aging temperature at which the data is collected. In this study, after shifting the curves w.r.t to the 70 C aging curve, we observe that the maximum

damage observed is around 75% which occurs at around 1.2 years. Comparing the 75% degradation with the Arrhenius and CDM model, we observe that they predict 0.7 and 1.4 years respectively.

We observe that the prediction from TTSP aligns more closely with the CDM model. However, more data points need to be tested to confirm the inflection point occurring at 110°C.

The aging kinetic model predicts the lifetime of SBR at room temperature as around three years. However, this is significantly lower (almost half) of the lifetime predicted by the CDM model and the Arrhenius model. This may be because of the assumption that the thermal crosslinking rate is uniform which simplifies the model. This further proves that the higher the temperature, the faster is the aging. Moreover, FTIR measures surface oxidation which is much higher than sub-surface oxidation. Thus, the kinetic aging model will always predict lifetime which is much lesser than that of the other mechanical models.

7 CONCLUSIONS AND FUTURE WORK

Thus, in the present work, the effects of thermo-oxidative aging are studied in detail. An in-depth literature review about various types of aging and their related research studies as well as rubber friction and wear studies are performed. This gives a general overview of the mechanisms of rubber friction and wear and how it is different from other materials. The influence of thermo-oxidative aging on the hyperelastic, viscoelastic, friction, wear, and chemical properties of SBR is studied using an integrated testing and modelling framework.

A novel and simple yet powerful CDM approach was applied to model the changes in the hyperelastic response of SBR as it is aged at various aging time periods and temperatures. The change in the response was captured by modifying the hyperelastic material parameters of the Arruda-Boyce model. A damage state variable was introduced to capture the material degradation over time due to aging. A modified form of the Avrami equation was used to predict the change in the damage variable. This model was then translated into an ABAQUS UMAT subroutine.

On similar lines, the effects of aging on the viscoelastic response were also studied. DMA tests were used to characterize the viscoelastic response by subjecting the SBR sample to various frequency and temperature sweeps. TTSP was then used to generate a master curve for storage and loss modulus. As observed, the storage and loss modulus increase with an increase in aging time. However, these changes are very small, and the samples also need to be tested at higher aging temperatures. These viscoelastic property changes also directly influence the friction and wear properties of SBR. CLD was estimated from the DMA data to show that the changes in SBR are indeed due to thermo-oxidative aging.

The effect of aging on the wear properties of SBR was also studied. The DFT was used to perform wear testing on aged SBR samples to collect data for mass and volume loss. It was observed that the aging time and temperature had a direct correlation with an increase in mass loss. This is due to the degradation of SBR due to aging as seen both in the hyperelastic and viscoelastic models. It is also due to the formation of surface cracks and defects as the material is aged. Using the viscoelastic model, the friction coefficient was estimated using the simplified form of Persson's equation. This was compared with the experimental friction coefficient obtained from the DFT data. The friction coefficient for the unaged SBR showed an excellent correlation between the model and the test data. However, as the sample was aged, the model outputted significantly lower friction coefficient values than the actual test results. This may be because of the simplifications and assumptions and also due to the surface crack formation and the adhesive friction component which is not considered in this model.

Finally, the lifetime of SBR for various aging temperatures is studied and predicted using various novel models— the CDM model, Arrhenius equation-based model, Aging TTSP models and Aging Kinetic model. All these models give a slightly different lifetime prediction when compared together, which is expected because each of them is based on different mechanical and chemical properties of SBR as they change due to aging.

7.1 FUTURE WORK

- Conduct different deformation mode experiments for hyperelastic response and compare with existing model results
- Test UMAT subroutine for different loading and geometries of rubber and compare to experimental data
- Conduct viscoelastic testing for higher aging temperatures
- Include the effects of adhesive friction components and surface cracks in the friction model
- Use Raman Spectroscopy to improve aging kinetic model prediction
- Perform Scanning Electron Microscopy (SEM) to study surface cracks formed due to aging and Schallamach patterns
- Develop a wear model to predict change in friction coefficient and wear due to aging
- Couple the hyperelastic and viscoelastic CDM models with the wear model

REFERENCES

[1] M. Ciavarella, “A Simplified Version of Persson’s Multiscale Theory for Rubber Friction Due to Viscoelastic Losses,” *J. Tribol.*, vol. 140, no. 1, 2018, doi: 10.1115/1.4036917.

[2] European Commission, “Critical raw materials,” *Internal Market, Industry, Entrepreneurship and SMEs*, 2020. .

[3] S. Polukoshko, A. Martinovs, and E. Zaicevs, “Experimental studing of mechanical-and-physical properties of rubber during ageing,” in *Vide. Tehnologija. Resursi - Environment, Technology, Resources*, 2019, vol. 3, pp. 214–218, doi: 10.17770/etr2019vol3.4200.

[4] S. Polukoshko, A. Martinovs, and E. Zaicevs, “Influence of rubber ageing on damping capacity of rubber vibration absorber,” in *Vibroengineering Procedia*, 2018, vol. 19, pp. 103–109, doi: 10.21595/vp.2018.20219.

[5] A. G. Korba, A. Kumar, and M. E. Barkey, “A model for hyper-elastic material behavior under thermal aging with an application to natural rubber,” in *ASME 2018 13th International Manufacturing Science and Engineering Conference, MSEC 2018*, 2018, vol. 2, doi: 10.1115/MSEC2018-6539.

[6] B. N. J. Persson, “Theory of rubber friction and contact mechanics,” *J. Chem. Phys.*, vol. 115, no. 8, 2001, doi: 10.1063/1.1388626.

[7] T. D. Gillespie, *Fundamentals of Vehicle Dynamics*. 1992.

[8] J. W. J. Hall, K. L. J. Smith, L. Titus-Glover, J. C. Wambold, T. J. Yager, and Z. Rado, “Guide for Pavement Friction,” 2009.

[9] Sunish Vadakkeveetil, “ Multi-Length Scale Modeling of Rubber Tribology For Tire Application,” Virginia Tech, Blacksburg, 2019.

[10] D. F. Moore, *The friction and lubrication of elastomers, by Desmond F. Moore*, [1st ed.]. Pergamon Press Oxford, New York, 1972.

[11] K. A. Grosch, “Correlation between road wear of tires and computer road wear simulation

using laboratory abrasion data," *Rubber Chem. Technol.*, vol. 77, no. 5, 2004, doi: 10.5254/1.3547852.

[12] S. D. Gehman, C. S. Wilkinson, and R. D. Daniels, "Smearing of Vulcanized Rubber," *Rubber Chem. Technol.*, vol. 28, no. 2, 1955, doi: 10.5254/1.3542812.

[13] A. Schallamach, "Abrasion, fatigue, and smearing of rubber," *J. Appl. Polym. Sci.*, vol. 12, no. 2, 1968, doi: 10.1002/app.1968.070120204.

[14] A. Tsujimoto *et al.*, "Wear of resin composites: Current insights into underlying mechanisms, evaluation methods and influential factors," *Japanese Dental Science Review*, vol. 54, no. 2. 2018, doi: 10.1016/j.jdsr.2017.11.002.

[15] G. Wu, "The mechanisms of rubber abrasion," Queen Mary, University of London, London, 2017.

[16] M. L. Williams, R. F. Landel, and J. D. Ferry, "The Temperature Dependence of Relaxation Mechanisms in Amorphous Polymers and Other Glass-forming Liquids," *J. Am. Chem. Soc.*, vol. 77, no. 14, 1955, doi: 10.1021/ja01619a008.

[17] V. H. Nguyen, D. Zheng, F. Schmerwitz, and P. Wriggers, "An advanced abrasion model for tire wear," *Wear*, vol. 396–397, 2018, doi: 10.1016/j.wear.2017.11.009.

[18] Y. Fukahori and H. Yamazaki, "Mechanism of rubber abrasion. Part I: Abrasion pattern formation in natural rubber vulcanizate," *Wear*, vol. 171, no. 1–2, 1994, doi: 10.1016/0043-1648(94)90362-X.

[19] K. A. Grosch, "The Relation between the Friction and Viscoelastic Properties of Rubber," *Rubber Chem. Technol.*, vol. 37, no. 2, 1964, doi: 10.5254/1.3540331.

[20] Nhtsa, "NHTSA Tire Aging Test Development Project - Tire Innerliner Analysis," *Security*, no. March, 2010.

[21] National Highway Traffic Safety Administration, "Firestone Tire Recall," Oct. 04, 2001. .

[22] A. Genovese, G. A. D'Angelo, A. Sakhnevych, and F. Farroni, "Review on friction and wear test rigs: An overview on the state of the art in tyre tread friction evaluation," *Lubricants*, vol. 8, no. 9. 2020, doi: 10.3390/LUBRICANTS8090091.

[23] L. N. T. 37201 (US) Bridgestone Americas Tire Operations and Bridgestone Corporation Tokyo 104–8340 (JP), “ENGINEERED SURFACES FOR LABORATORY TREAD WEAR TESTING OF TIRES,” EP 2 668 486 B1, 2013.

[24] C. Su, “Integrated Experimental Methods and Machine Learning for Tire Wear Prediction,” Virginia Tech, Blacksburg, 2019.

[25] M. Barquins and A. D. Roberts, “Rubber friction variation with rate and temperature: Some new observations,” *J. Phys. D. Appl. Phys.*, vol. 19, no. 4, 1986, doi: 10.1088/0022-3727/19/4/010.

[26] Y. FUKAHORI, “Carbon Black Reinforcement of Rubbers: No.8 (Final): The Origin of Weakness and Reinforcement of Elastomers,” *Nippon GOMU KYOKAISHI*, vol. 78, no. 1, 2005, doi: 10.2324/gomu.78.19.

[27] H. Watabe, M. Komura, K. Nakajima, and T. Nishi, “Atomic force microscopy of mechanical property of natural rubber,” *Japanese J. Appl. Physics, Part 1 Regul. Pap. Short Notes Rev. Pap.*, vol. 44, no. 7 B, 2005, doi: 10.1143/JJAP.44.5393.

[28] M. Barquins and R. Courtel, “Rubber friction and the rheology of viscoelastic contact,” *Wear*, vol. 32, no. 2, 1975, doi: 10.1016/0043-1648(75)90263-X.

[29] A. Schallamach, “Friction and abrasion of rubber,” *Wear*, vol. 1, no. 5, 1958, doi: 10.1016/0043-1648(58)90113-3.

[30] Y. Wu, J. Dong, C. Sun, J. Li, and J. Chen, “A novel methodology for evaluating wear behavior of rubber composites under combination of sliding and rolling conditions,” *Polym. Eng. Sci.*, vol. 60, no. 9, 2020, doi: 10.1002/pen.25456.

[31] R. Ramakrishnan, J. A. Donovan, and A. I. Medalia, “The Effect of Abrading Surfaces on the Wear of Rubber Tread Compounds,” *Rubber Chem. Technol.*, vol. 68, no. 4, 1995, doi: 10.5254/1.3538762.

[32] M. Gunaratne, N. Bandara, J. Medzorian, M. Chawla, and P. Ulrich, “Correlation of Tire Wear and Friction to Texture of Concrete Pavements,” *J. Mater. Civ. Eng.*, vol. 12, no. 1, 2000, doi: 10.1061/(asce)0899-1561(2000)12:1(46).

[33] M. Gonzalez, A. De Oliveira Lima, and S. L. Tighe, “Nanoconcrete for rigid pavements: Abrasion response and impact on friction,” *Transportation Research Record*, vol. 2441. 2014, doi: 10.3141/2441-05.

[34] T. Vieira, R. P. Ferreira, A. K. Kuchiishi, L. L. B. Bernucci, and A. Sinatora, “Evaluation of friction mechanisms and wear rates on rubber tire materials by low-cost laboratory tests,” *Wear*, vol. 328–329, 2015, doi: 10.1016/j.wear.2015.04.001.

[35] M. Resnikowskij, “.,” *Kautschuk und Gummi, Nr. 9*, pp. 33–37, 1960.

[36] I. Kragelskij, “.,” *Wear, Vol. 8, No.4*, pp. 303–329, 1965.

[37] H. Hertz, “.,” *J. fur die reine und Angew. Math. Issue 92*, pp. 156–171, 1882.

[38] Y. Miyashita and H. Kato, “Cross-linking reaction of LDPE and the behavior of decomposition products from cross-linking agents,” 1988, doi: 10.1109/iseim.1988.763488.

[39] J. Zhi, Q. Wang, M. Zhang, Z. Zhou, A. Liu, and Y. Jia, “Coupled analysis on hyper-viscoelastic mechanical behavior and macromolecular network alteration of rubber during thermo-oxidative aging process,” *Polymer (Guildf).*, vol. 171, pp. 15–24, 2019, doi: 10.1016/j.polymer.2019.03.029.

[40] B. Moon, J. Lee, S. Park, and C.-S. Seok, “Study on the aging behavior of natural rubber/butadiene rubber (NR/BR) blends using a parallel spring model,” *Polymers (Basel).*, vol. 10, no. 6, 2018, doi: 10.3390/polym10060658.

[41] J. Zhao, R. Yang, R. Iervolino, and S. Barbera, “Investigation of crosslinking in the thermooxidative aging of nitrile-butadiene rubber,” *J. Appl. Polym. Sci.*, vol. 132, no. 3, 2015, doi: 10.1002/app.41319.

[42] Searcy Law, “How aging tires can cause unexpected blowouts,” Jan. 27, 2014. .

[43] N. H. T. S. A. S. A. O. of D. I. U.S. Department of Transportation, “EA00-023: Firestone Wilderness AT Tires,” Oct. 2001.

[44] Q. Liu, W. Shi, K. Li, Z. Chen, and H. Liu, “Performance Degradation Prediction and Reliability Evaluation of Rubber Aging in Natural Environment under Alternating Cyclic

Thermal Load," *IEEE Access*, vol. 7, pp. 63027–63035, 2019, doi: 10.1109/ACCESS.2019.2917008.

[45] C. Bendjaouahdou and S. Bensaad, "Aging studies of a polypropylene and natural rubber blend," *Int. J. Ind. Chem.*, vol. 9, no. 4, pp. 345–352, 2018, doi: 10.1007/s40090-018-0163-2.

[46] S. Kashi *et al.*, "Mechanical, Thermal, and Morphological Behavior of Silicone Rubber during Accelerated Aging," *Polym. - Plast. Technol. Eng.*, vol. 57, no. 16, pp. 1687–1696, 2018, doi: 10.1080/03602559.2017.1419487.

[47] H. He, W. Hu, and S. Gao, "Prediction of rubber aging life by intelligent neural network," in *MATEC Web of Conferences*, 2018, vol. 175, doi: 10.1051/matecconf/201817503070.

[48] H. He, K. Liu, X. Fu, and K. Ye, "Development of rubber aging life prediction software," *Lect. Notes Comput. Sci. (including Subser. Lect. Notes Artif. Intell. Lect. Notes Bioinformatics)*, vol. 10464 LNAI, pp. 831–842, 2017, doi: 10.1007/978-3-319-65298-6_74.

[49] J. Liu, X. Li, L. Xu, and P. Zhang, "Investigation of aging behavior and mechanism of nitrile-butadiene rubber (NBR) in the accelerated thermal aging environment," *Polym. Test.*, vol. 54, pp. 59–66, 2016, doi: 10.1016/j.polymertesting.2016.06.010.

[50] Y. Li, P. Zhu, J. Wen, Q. Zhang, and L. Yin, "Influence of carbon black on aging properties of natural rubber," in *IOP Conference Series: Earth and Environmental Science*, 2021, vol. 692, no. 3, doi: 10.1088/1755-1315/692/3/032051.

[51] R. Bouaziz *et al.*, "Elastic properties of polychloroprene rubbers in tension and compression during ageing," *Polymers (Basel).*, vol. 12, no. 10, pp. 1–14, 2020, doi: 10.3390/polym12102354.

[52] C. L. Dong, C. Q. Yuan, X. Q. Bai, X. P. Yan, and Z. Peng, "Tribological properties of aged nitrile butadiene rubber under dry sliding conditions," *Wear*, vol. 322–323, 2015, doi: 10.1016/j.wear.2014.11.010.

[53] R. Han, Y. Wu, X. Quan, and K. Niu, "Effects of crosslinking densities on mechanical properties of nitrile rubber composites in thermal oxidative aging environment," *J. Appl.*

Polym. Sci., vol. 137, no. 36, 2020, doi: 10.1002/app.49076.

[54] N. Rezig, T. Bellahcene, M. Aberkane, and M. Nait Abdelaziz, "Thermo-oxidative ageing of a SBR rubber: effects on mechanical and chemical properties," *J. Polym. Res.*, vol. 27, no. 11, 2020, doi: 10.1007/s10965-020-02330-y.

[55] K. Xiang, G. Huang, J. Zheng, X. Wang, and J. Huang, "Investigation on the thermal oxidative aging mechanism and lifetime prediction of butyl rubber," *Macromol. Res.*, vol. 21, no. 1, pp. 10–16, 2013, doi: 10.1007/s13233-012-0174-3.

[56] A. G. Korba, A. Kumar, and M. Barkey, "A hyper-elastic thermal aging constitutive model for rubber-like materials," *J. Elastomers Plast.*, vol. 52, no. 8, pp. 677–700, 2020, doi: 10.1177/0095244319883405.

[57] D. F. Tandy, R. Pascarella, K. Tandy, and J. Neal, "Effect of aging on tire force and moment characteristics," *SAE Tech. Pap.*, 2010, doi: 10.4271/2010-01-0772.

[58] M. G. Pottinger and K. D. Marshall, "The effect of tire aging on force and moment properties of radial tires," *SAE Tech. Pap.*, 1981, doi: 10.4271/810066.

[59] O. M. Baldwin and D. R. Bauer, "Rubber oxidation and tire aging - A review," *Rubber Chem. Technol.*, vol. 81, no. 2, pp. 338–358, 2008, doi: 10.5254/1.3548213.

[60] J. M. Baldwin, D. R. Bauer, and P. D. Hurley, "Field aging of tires, part II," *Rubber Chem. Technol.*, vol. 78, no. 5, pp. 754–766, 2005, doi: 10.5254/1.3547911.

[61] J. M. Baldwin, D. R. Bauer, and K. R. Ellwood, "Rubber aging in tires. Part 1: Field results," *Polym. Degrad. Stab.*, vol. 92, no. 1, pp. 103–109, 2007, doi: 10.1016/j.polymdegradstab.2006.08.030.

[62] D. R. Bauer, J. M. Baldwin, and K. R. Ellwood, "Correlation of laboratory tire endurance and rubber aging," *Rubber Chem. Technol.*, vol. 80, no. 4, pp. 726–737, 2007, doi: 10.5254/1.3548190.

[63] D. R. Bauer, J. M. Baldwin, and K. R. Ellwood, "Rubber aging in tires. Part 2: Accelerated oven aging tests," *Polym. Degrad. Stab.*, vol. 92, no. 1, pp. 110–117, 2007, doi: 10.1016/j.polymdegradstab.2006.08.014.

[64] J. M. Baldwin, D. R. Bauer, and K. R. Ellwood, “Accelerated aging of tires, part III,” *Rubber Chem. Technol.*, vol. 78, no. 5, pp. 767–776, 2005, doi: 10.5254/1.3547912.

[65] B. Trobentar, S. Glodež, and B. Zafošnik, “Gear tooth deflection of spur polymer gears,” in *International Gear Conference 2014: 26th–28th August 2014, Lyon*, 2014.

[66] A. F. Bower, *Applied mechanics of solids*. 2009.

[67] L. Mullins, “Softening of Rubber by Deformation,” *Rubber Chem. Technol.*, vol. 42, no. 1, 1969, doi: 10.5254/1.3539210.

[68] I. I. Muhamad *et al.*, “Accelerated testing methodology for long-term life prediction of cellulose-based polymeric composite materials,” in *Durability and Life Prediction in Biocomposites, Fibre-Reinforced Composites and Hybrid Composites*, 2018.

[69] ASTM, “Standard Test Method for Rubber — Deterioration by Heating in Air (Test Tube Enclosure) 1,” *Annu. B. ASTM Stand.*, vol. i, 2012.

[70] Dassault Systèmes Simulia, A. . Fallis, and D. Techniques, “ABAQUS documentation,” *Abaqus 6.12*, vol. 53, no. 9, 2013.

[71] D. Kondo, H. Welemane, and F. Cormery, “Basic concepts and models in continuum damage mechanics,” *Rev. Eur. génie Civ.*, vol. 11, no. 7–8, 2007, doi: 10.3166/regc.11.927-943.

[72] R. W. Sullivan, “Development of a viscoelastic continuum damage model for cyclic loading,” *Mech. Time-Dependent Mater.*, vol. 12, no. 4, 2008, doi: 10.1007/s11043-008-9069-2.

[73] G. C. Papanicolaou and S. P. Zaoutsos, “Viscoelastic constitutive modeling of creep and stress relaxation in polymers and polymer matrix composites,” in *Creep and Fatigue in Polymer Matrix Composites*, 2019.

[74] Richard Gedney, “An Introduction to Viscoelasticity Dynamic Mechanical Analysis,” *Quality Magazine*, Feb. 01, 2019. .

[75] OpenLearn, “Introduction to polymers- Time-Temperature superposition,” *Open.edu*, Oct. 08, 2012. .

[76] J. D. Ferry, *Viscoelastic properties of polymers*. 1980.

[77] T. Kaneko, S. Ito, T. Minakawa, N. Hirai, and Y. Ohki, "Degradation mechanisms of silicone rubber under different aging conditions," *Polym. Degrad. Stab.*, vol. 168, 2019, doi: 10.1016/j.polymdegradstab.2019.108936.

[78] O. Kratina, R. Stoček, and E. Euchler, "The influence of thermal ageing of natural rubber/Styrene butadiene rubber Vulcanizates on Steady state and Dynamic Wear behaviour," *KGK Kautschuk Gummi Kunststoffe*, vol. 69, no. 4, 2016.

[79] I. Kragelski, M. Dobychin, and V. Kombalov, "The calculation framework of the friction and wear." Mashynostroenie, 1977.

[80] V. L. Popov, *Contact mechanics and friction: Physical principles and applications, second edition*. 2017.

[81] G. Heinrich, "Hysteresis friction of sliding rubbers on rough and fractal surfaces," *Rubber Chem. Technol.*, vol. 70, no. 1, 1997, doi: 10.5254/1.3538415.

[82] S. S. Choi, "Influence of rubber composition on change of crosslink density of rubber vulcanizates with EV cure system by thermal aging," *J. Appl. Polym. Sci.*, vol. 75, no. 11, 2000, doi: 10.1002/(SICI)1097-4628(20000314)75:11<1378::AID-APP9>3.0.CO;2-I.